

Studies of reactor anti-neutrinos with ISMIRAN

By

Dhruv Mulmule

PHYS01201504023

Nuclear Physics Division,
Bhabha Atomic Research Centre (BARC),
Mumbai - 400085

*A thesis submitted
to the Board of Studies in
Physical Sciences*

*In partial fulfillment of requirements
For the Degree of*

DOCTOR OF PHILOSOPHY

of

HOMI BHABHA NATIONAL INSTITUTE

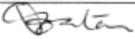
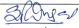
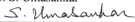


September, 2020

Homi Bhabha National Institute

Recommendations of the Viva Voce Committee

As members of the Viva Voce Committee, we certify that we have read the dissertation prepared by **Dhruv Mulmule** entitled "**Studies of reactor anti-neutrinos with ISMRAN**" and recommend that it may be accepted as fulfilling the thesis requirement for the award of Degree of Doctor of Philosophy.

Chairman - Prof. Vivek M. Datar		Date: 29-01-2021
Guide / Convener - Prof. L. M. Pant		Date: 28/01/2021
Examiner - Prof. S. R. Dugad		Date: 28/01/2021
Member 1 - Dr. B. Satyanarayana		Date: 28/01/2021
Member 2 - Dr. V. Jha		Date: 28.01.2021
Member 3 - Prof. S. Umasankar		Date: 28.01.2021

Final approval and acceptance of this thesis is contingent upon the candidate's submission of the final copies of the thesis to HBNI.

I hereby certify that I have read this thesis prepared under my direction and recommend that it may be accepted as fulfilling the thesis requirement.

Date : 28 Jan 2021
Place : Mumbai


Prof. L. M. Pant (Guide)

STATEMENT BY THE AUTHOR

This dissertation has been submitted in partial fulfillment of requirements for an advanced degree at Homi Bhabha National Institute (HBNI) and is deposited in the library to be made available to borrowers under rules of the HBNI.

Brief quotations from this dissertation are allowable without special permission, provided that accurate acknowledgement of source is made. Requests for permission for extended quotation from or reproduction of this manuscript in whole or in part may be granted by the Competent Authority of HBNI when in his or her judgment the proposed use of the material is in the interests of scholarship. In all other instances, however, permission must be obtained from the author.

September 2020, Mumbai

A handwritten signature in black ink, appearing to read 'Dhruv', written over a horizontal line.

Dhruv Mulmule

DECLARATION

I hereby declare that the investigation presented in the thesis has been carried out by me. The work is original and has not been submitted earlier as a whole or in part for a degree/diploma at this or any other Institution/University.

September 2020, Mumbai

A handwritten signature in black ink, appearing to read 'Dhruv', is written over a horizontal line. The signature is slanted upwards to the right.

Dhruv Mulmule

List of Publications arising from the thesis

Publications in Refereed Journal

Published

1. A plastic scintillator array for reactor based anti-neutrino studies, D. Mulmule, S. P. Behera, P. K. Netrakanti, D. K. Mishra, V. K. S. Kashyap, V. Jha, L. M. Pant, B. K. Nayak, A. Saxena, *Nuclear Instruments and Methods in Physics Research Section A: Accelerators, Spectrometers, Detectors and Associated Equipment*, (2018), 911, pp. 104 – 114, doi : 10.1016/j.nima.2018.10.026 .
2. Machine learning technique to improve anti-neutrino detection efficiency for the ISMRAN experiment, D. Mulmule, P. K. Netrakanti, L. M. Pant

and B. K. Nayak, *Journal of Instrumentation*, (2020), 15, pp. P04021, doi : 10.1088/1748-0221/15/04/p04021 .

Symposium and Conference proceedings

1. **D. Mulmule**, P.K. Netrakanti, S.P. Behera, D.K. Mishra, V. Jha, V. Rao, S. Bhatt, L.M. Pant, B.K. Nayak, *Background reduction studies with shielding for mini-ISMARAN*. Proceedings of DAE international symposium on nuclear physics V. 63, G26 (2018), URL: <http://www.symnpn.org/proceedings/63/G26.pdf> .
2. S. P. Behera, **D. Mulmule**, D. K. Mishra, P. K. Netrakanti, V. Jha, L. M. Pant, B. K. Nayak, *Sum energy technique for anti-neutrino event reconstruction in ISMRAN*. Proceedings of DAE international symposium on nuclear physics V. 63, G27 (2018), URL: <http://www.symnpn.org/proceedings/63/G27.pdf> .
3. **D. Mulmule**, P.K. Netrakanti, S.P. Behera, D.K. Mishra, V. Jha, L.M. Pant, B.K. Nayak, *Exploring anti-neutrino event selection and background reduction techniques for ISMRAN*. Applied Antineutrino Physics 2018 Workshop, LLNL, USA, (2018). URL: <https://arxiv.org/pdf/1911.06834> .
4. **D. Mulmule**, P.K. Netrakanti, S.P. Behera, D.K. Mishra, V. Jha, L.M. Pant, B.K. Nayak, *Anti-neutrino like events from mini-ISMARAN at Dhruva reactor*. Proceedings of DAE symposium on nuclear physics V. 64, (2019) Lucknow University, Lucknow, URL: <http://symnpn.org/proceedings/64/G8.pdf> .

5. **D. Mulmule**, P.K. Netrakanti, L.M. Pant, B.K. Nayak, *Improvements in prompt and delay event selection in ISMRAN using artificial neural networks*. Proceedings of DAE symposium on nuclear physics V. 64, (2019) Lucknow University, Lucknow, URL: <http://sympnp.org/proceedings/64/G9.pdf> .

6. **D. Mulmule**, P.K. Netrakanti, V. Jha, S.P. Behera, D.K. Mishra, L.M. Pant, B.K. Nayak, A. Saxena, *Measurement of non-reactor background and effect of borated polyethylene shielding for ISMRAN*. Proceedings of DAE symposium on nuclear physics V. 62, (2017) Thapar University, Patiala, URL: <http://sympnp.org/proceedings/62/G13.pdf> .



Dhruv Mulmule

DEDICATED TO

My Sister

who gave me the strength and support to pursue my PhD

And

My Parents

whose blessings have always been with me

ACKNOWLEDGEMENTS

I would like to thank my doctoral advisor Prof. L. M. Pant for his constant guidance and support throughout my thesis work. It was his meticulous planning and supervision that allowed me to complete my thesis work in time and get things in good shape by the end. I thank Prof. V. M. Datar for making me part of the INO programme. As the chairman of my doctoral committee, I'm thankful to him for his guidance and inspiring discussions. I would also like to thank the other members of my doctoral committee: Prof. S. Umasankar, Dr. B. Satyanarayana and Dr. V. Jha for guiding the progress of my work. My thanks also to all the great teachers who taught me during my course work at TIFR - Professors V. M. Datar, S. Umasankar, G. Majumdar, V. Nanal, S. Banerjee, K. Mazumdar, S. Raychaudhuri, K. Sridhar, R. Vijayraghavan and Ms. Mandakini Patil.

I'm extremely grateful to my other colleagues in the ISMRAN team – Dr. V. Jha, Dr. P.K. Netrakanti, Dr. D. K. Mishra and Dr. S.P. Behera for their immense generosity and patience in training me during my PhD tenure. Discussing physics with Dr. Jha helped improve my understanding. Dr. P.K. Netrakanti made sure that the milestones of my thesis work were reached in time. Working closely with him was an eye-opener in many ways and gave me a broader perspective on being part of a collaborative work. Dr. Dipak Mishra always provided useful inputs and the right advice. Dr. S.P. Behera, being more of a contemporary to me, was very understanding of my situation and always helpful. I also thank the open source community, especially, the Linux, StackExchange, L^AT_EX, GEANT and ROOT communities for their numerous computing and scientific tools and

discussion forums.

Last but not the least, I'm thankful to my junior colleague - Roni dey, my batch-mates - Jaydeep Dutta and Aparajita Mazumdar, Seniors - Varchaswi Kashyap, Neha Panchal, Apoorva Bhatt, Suryanarayana Mondal, S. Pethuraj, Scientific officers - Mr. Mandar Saraf, Yuvaraaj, Pathaleshwar, Mr. Shinde and Support staff - at INO Mr. Asgolkar, Mr. Chavan who have all helped me through various situations I encountered either during the course-work or later in PhD. We also enjoyed fun get-togethers and meets which helped bring down my stress level whenever I got overwhelmed by the work.

Contents

Summary	23
List of Figures	25
List of Tables	37
List of Abbreviations	42
1 Neutrino	43
1.1 Early developments	43
1.2 Standard model of particles	44
1.2.1 Neutrino in Standard Model	45
1.3 Sources of neutrinos	46
1.3.1 Natural sources	47
1.3.2 Man-made sources	51

1.4	The Neutrino voyage : From discovery to applications	53
1.4.1	The Discovery of neutrino - ‘Project Poltergeist’	54
1.4.2	Discovering the μ and τ flavour neutrinos: AGS and DONUT experiments	56
1.5	Neutrino oscillations : Anomalies and experimental results . . .	57
1.5.1	Solar Neutrino problem	58
1.5.2	Confirmation of Solar neutrino oscillation	59
1.5.3	Atmospheric Neutrino Anomaly	61
1.6	Theoretical background of neutrino oscillation	63
1.6.1	Two flavour mixing of neutrinos	65
1.6.2	Matter oscillations of neutrinos	66
1.6.3	Hierarchy in the neutrino mass eigenstates	66
1.7	Are neutrinos majorana or Dirac particles ?	67
1.8	Anomalies pointing to more neutrinos	68
1.8.1	Short baseline oscillations : LSND Anomaly	69
1.9	Reactor Anti-neutrino Anomaly	70
1.9.1	Search for sterile neutrinos	71
1.9.2	Spectral distortion at 5 MeV : The ‘Bump’	74
1.10	Neutrinos as messenger particles	76
1.10.1	Multi-messenger astronomy : IceCube experiment	76
1.11	Reactor monitoring	79
1.11.1	Worldwide efforts	80
1.12	Indian Scintillator Matrix for Reactor AntiNeutrinos (ISMARAN)	84
1.13	Summary	86

<i>CONTENTS</i>	19
2 Indian Scintillator Matrix for Reactor AntiNeutrinos	89
2.1 Reactor safeguards and anti-neutrino monitors	89
2.2 The Dhruva reactor	90
2.3 $\bar{\nu}_e$ event detection and rates in ISMRAN	93
2.4 ISMRAN PS bar	96
2.5 ISMRAN detector	99
2.6 Pulse processing electronics and DAQ	102
2.6.1 Acquisition software - digiTES	110
2.7 Prototype detector – mini-ISMРАН	112
2.8 ISMRAN PS characterization studies	115
2.8.1 Gain matching	116
2.9 Calibration	124
2.10 Summary	133
3 Detector Simulations	135
3.1 Simulation setup for ISMRAN	135
3.2 ISMRAN simulation results:	140
3.2.1 Results from IBD event simulations	147
3.3 Detection efficiency for pure IBD events in ISMRAN	157
3.3.1 Photon evaporation Vs Final state model	160
3.4 Event embedding procedure	162
3.5 Cosmic muon and neutron backgrounds	169
3.6 Summary	174
4 Machine learning framework for ISMRAN	175
4.1 Choice of analysis technique	175

4.2	Multivariate analysis and Machine learning	176
4.3	Artificial Neural Networks and Multi-Layer Perceptron	177
4.3.1	TMVA analysis package and its MLP	181
4.4	Event definitions in ISMRAN	182
4.5	Multivariate classifier for ISMRAN	183
4.6	Results from reco prompt vs background classification with MLP	188
4.7	Evaluation of the MLP classifier performance for reco prompt selection	195
4.8	Summary	199
5	miniISMRAN data-taking and analysis	201
5.1	Measurements with miniISMRAN	201
5.2	Non-reactor and reactor background measurements with mini- ISMRAN	202
5.2.1	Non-reactor background measurement	205
5.2.2	Reactor background measurement	206
5.3	Event building in reactor data	213
5.3.1	Prompt and delayed events in ISMRAN	214
5.4	Mixed event analysis	224
5.5	Filtered IBD candidate events after cuts	229
5.6	Summary	231
	Conclusions and Outlook	232
6	Conclusions	233
6.1	Studies of $\bar{\nu}_e$ using ISMRAN	234

<i>CONTENTS</i>	21
6.2 Simulations in ISMRAN geometry	234
6.3 Using MLP for improved detection efficiency	235
6.4 Analysis results from the prototype - miniISMRAN	236
7 Outlook	237
7.1 Full scale ISMRAN detector	237
7.2 Extracting neutrino spectrum	238
7.3 Detection technology	238
7.4 New physics	239
7.5 Potential reactor sites	240
Bibliography	243

List of Figures

1.1	The standard model of particle physics. (Image source [4])	44
1.2	Neutrino spectra from various natural and man-made sources [13].	47
1.3	Left: The detector used at the Savannah River plant. Right: Visualization of a prompt and delayed event in this detector [22].	55
1.4	A schematic of Sudbury Neutrino Observatory 2039 m below the surface in a nickel mine near Sudbury, Ontario [31]	60
1.5	A cutaway schematic of Super kamiokande detector. The inner and outer detector and the dome with the front end electronics and calibration equipment are visible [35].	62
1.6	Feynman diagram of double beta decay for Left: Dirac neutrinos and Right: Majorana neutrino cases [41].	67
1.7	The invisible decay width of Z boson and fit performed for different neutrino numbers [43].	68

1.8	The basic element of SoLiD detector – ‘PVT cube’ with its components shown on top. An IBD event inside the detector is visualized in middle and time delay signature of prompt and delayed event shown at the bottom [53]	73
1.9	NEOS and Daya Bay experimental results compared with ‘H-M-V’ model [54].	75
1.10	The schematic of IceCube Neutrino Observatory [18]	78
1.11	Left: The main LS tank of NUCIFER and Right: Final shielded setup of NUCIFER detector [59]	82
1.12	Schematic of ISMRAN setup	85
2.1	Left: Dhruva reactor building at BARC from outside. Right: Inside the Dhruva reactor hall.	91
2.2	Left: Cross-sectional view of Dhruva reactor core [66]. Right: ISMRAN footprint location and orientation w.r.t core center in reactor hall.	92
2.3	Top: ISMRAN PS bar in lab. Bottom: Drawing of the PS bar showing different parts and dimensions.	97
2.4	Emission spectrum or wavelengths of scintillation photons for EJ200 scintillator [68].	98
2.5	Proposed ISMRAN detector setup comprising of shielding trolley and 100 PS bars. The major components of the setup are listed in their respective colors at top.	100

2.6	Cross-sectional view of modified ISMRAN assembly design with provision of in-situ calibration. The shielding plugs and slots are visible.	102
2.7	V1730 digitizer based system of 12 boards, synchronized and daisy-chained for data taking operation.	103
2.8	Typical pulse acquisition for waveform digitizers showing trigger and gating information [71].	104
2.9	Timestamp derivation from cross-over in digitizer pulse processing algorithm [70]	105
2.10	The timestamp difference ΔT_{TS} between master and slave digitizers for the muon events Left: Before synchronization and Right: After synchronization.	109
2.11	Architecture of the digiTES code showing various blocks of operation.	111
2.12	mini-ISMRAN 4×4 matrix in laboratory environment.	113
2.13	mini-ISMRAN 4×4 matrix with progressively increasing shielding in reactor environment.	114
2.14	ADC spectrum of the Near (black) and Far (red) end PMTs of an ISMRAN PS bar at standard operating voltage of -1800V.	117
2.15	Compton edge channel numbers for 1.274 MeV ^{22}Na γ -ray plotted for Near and Far PMT ADC spectra at different bias voltages. The resulting graph is fitted with a polynomial function for gain matching purposes.	119

- 2.16 Compton edge ADC value for 1.274 MeV γ -ray of ^{22}Na source extracted from the ADC spectrum of Near and Far PMT of PS bars SF882 to SF890 at different bias voltages. The resulting graph is fitted with a polynomial function for gain matching purposes. 120
- 2.17 ADC spectrum of natural activity recorded in 18 of the PS bars. **Left:**Before gain matching. **Right:**After gain matching. 121
- 2.18 ADC spectrum of the end PMTs of a single PS bar as the source data is recorded for intervals of 10 cm, from one end to other. 122
- 2.19 ADC values of ^{137}Cs compton edge plotted for the near and far PMT at 10 cm intervals. The G.M. is plotted in solid line seen along the center. 122
- 2.20 Energy calibrated distributions for ISMRAN PS bar. Panel (a) shows ^{137}Cs (black), ^{22}Na (blue) and ^{60}Co (red) γ -ray source response. Panel(b) shows the recorded and calibrated Am-Be response. Panel (c) shows the natural background and cosmic muon activity. 125
- 2.21 ΔT_{LR} distribution for ^{137}Cs source placed at center of the PS bar. . . 127
- 2.22 ΔT_{LR} distribution for ^{137}Cs source placed at different positions along the length of the PS bar. 128
- 2.23 ΔT_{LR} vs source position graph fitted with polynomial function. . . . 129
- 2.24 ΔT distribution for cosmic muons passing vertically through the center of two PS bars. 131

- 2.25 The sum energy distribution within 40 ns time window, (a) $N_{\text{bars}} = 4$, (b) $N_{\text{bars}} = 5$ and (c) $N_{\text{bars}} = 6$, for the ^{60}Co (solid histogram) and natural background (filled histogram) events. The insets in panel (a) and (b) shows the zoomed x-axis of the sum energy distribution for the ^{60}Co source and natural background. 132
- 3.1 Cross-sectional view of ISMRAN detector in simulation. 136
- 3.2 Relative $\bar{\nu}_e$ flux due to different isotopes convoluted with IBD cross-section to give measured spectrum in detector [76]. 138
- 3.3 **Left:** Evolution of isotopic fission fractions with fuel burn-up [77] and **Right:** The IBD spectrum due to the dominant core fuel isotopes highlighting the disparity in their spectrum [78]. 140
- 3.4 γ -ray acceptance of Pb and Pb+BP shield for ISMRAN. 141
- 3.5 Fast neutron acceptance of different thickness of Pb+BP shield. 143
- 3.6 The incident (blue) and penetrating (red) cosmic neutron flux for the ISMRAN shielding. 144
- 3.7 Comparison of energy distribution between data (solid) and simulation (dashed) from a ^{137}Cs source spectrum in a 100cm \times 10cm \times 10cm PS bar. The simulation results are smeared for the energy resolution of the plastic scintillator bar. 147
- 3.8 **Left:** Linear energy response curve for ISMRAN PS bar showing γ -ray source data points, **Right:** Energy resolution curve for ISMRAN PS bar obtained from the same source data points. 148
- 3.9 IBD event simulated inside ISMRAN geometry depicted using separate color coding for each particle. 149

3.10	Sum energy (left) and N_{bars} (right) distributions for prompt positron event in ISMRAN for nominal and 0.2 MeV threshold.	152
3.11	IBD neutron capture event position profile highlighting the two major capture location due to elements: Gd on left panel and due to H on right panel	154
3.12	ΔT between prompt and delay event from simulation in ISMRAN geometry for the two dominant capture elements Gd and H.	154
3.13	Sum energy (left) and N_{bars} (right) distributions for delayed neutron event in ISMRAN geometry with and without shielding.	155
3.14	Comparison of sum energy (left) and N_{bars} (right) distributions for delayed neutron event in ISMRAN and mini-ISMРАН geometries.	157
3.15	Sum energy (left) and N_{bars} (right) distributions for delayed neutron event in ISMRAN geometry for choice of final state and photon evaporation models of Gd de-excitation.	161
3.16	Timestamp differences of PS bars for whole dataset compared between simulation and miniISMРАН data.	163
3.17	Time difference for different PS bars of an event compared between simulation and miniISMРАН data for prompt(left) and delayed(right) events.	164
3.18	Difference of Z values of bars in an event compared between simulation and miniISMРАН data for prompt (left) and delayed (right) events.	165
3.19	E_1/E_{max} ratio of prompt(left) and delayed (right) events compared between simulation and miniISMРАН data.	166

<i>List of Figures</i>	31
3.20 E_{\max}/E_{tot} ratio of prompt(left) and delayed (right) events compared between simulation and miniISMARAN data.	166
3.21 Difference in Z position of prompt delay pairs in simulation and miniISMARAN data.	167
3.22 Typical energy spectrum recorded for CRY generated cosmic muon event in ISMRAN PS bar.	171
3.23 The sum energy (left) and N_{bars} (right) for the cosmogenic muon event in ISMRAN.	172
3.24 Typical energy spectrum recorded for CRY generated cosmic neutron event in ISMRAN PS bar.	173
3.25 The sum energy (left) and N_{bars} (right) for the cosmogenic neutron events in ISMRAN.. . . .	173
4.1 Simulated Sum Energy (panel (a)) and N_{bars} distributions (panel (b)) for prompt and delayed events in ISMRAN showing overlap at the threshold level cuts.	176
4.2 Simplest feed-forward neural network [88].	178
4.3 Flow of supervised learning mechanism using weights ‘W’ and biases ‘b’ in Machine learning. [93].	179
4.4 The two hidden layer MLP architecture for ISMRAN showing the neurons and their connections (synapses) color coded, with blue end representing weaker connection strength and red end depicting stronger connections.	185

- 4.5 Panel (a) and (b) shows the comparison of performance for maximum likelihood and MLP classifiers on simulated IBD reco prompt and false prompt events in ISMRAN detector, respectively. Panel (c) shows the comparison of ROC curve for the MLP and maximum likelihood classifiers. 187
- 4.6 Panel (a) shows the reco prompt and false prompt event separation for D_k variable for IBD events in ISMRAN. Panel (b) shows the response after application of MLP classifier including the D_k variable along with N_{bars} and sum energy variable. Panel (c) shows the improvement in the ROC curve of MLP classifier with inclusion of D_k variable for reco prompt efficiency and false prompt rejection. 190
- 4.7 Panel (a) and (b) shows the MLP classifier response for reco prompt events from positron and false prompt events from neutron capture on Gd and H, respectively. Panel (c) shows the comparison of ROC curve for the reco prompt efficiency and false prompt rejection from neutron capture events on Gd and H. 192
- 4.8 Panel (a) MLP classifier response for reco prompt events from positron and reactor γ -ray backgrounds. Panel (b) ROC curve for the reco prompt efficiency and reactor γ -ray background rejection. . . . 193
- 4.9 Panel (a) MLP classifier response for reco prompt events from positron and proton recoil events from fast neutrons. Panel (b) ROC curve for the reco prompt efficiency and fast neutron rejection. . . . 194
- 4.10 Reco prompt efficiency, purity and product of efficiency and purity for MLP as a function of different selection cut values on the MLP output. 196

4.11	Panel(a) : Prompt sum energy distribution for true input, reco prompt events classified with MLP and from a cut based analysis. Panel(b) shows the false prompt events which are misidentified as reco prompt events using MLP classifier and cut based analysis.	198
5.1	Non-reactor background spectrum recorded in 16 PS bars of the unshielded miniISMARAN setup in laboratory.	206
5.2	Energy spectrum recorded in ISMRAN PS bar under reactor ON condition for no-shielding and full shielding configurations.	207
5.3	Energy distributions recorded in ISMRAN PS bar under full shielding reactor ON and OFF conditions.	208
5.4	Energy distributions recorded in a CeBr ₃ γ -ray detector under reactor ON and OFF conditions.	209
5.5	PSD vs Energy plot for events recorded with 5" liquid scintillator inside full ISMRAN shielding.	210
5.6	PSD plot for events recorded with 5" liquid scintillator inside full ISMRAN shielding for specific energy cut.	211
5.7	Deviations from the expected MPV for muon events in all the mini-ISMARAN PS bars at the reactor site.	212
5.8	Inter bar ΔT distribution for events in the miniISMARAN matrix.	213
5.9	ΔT_{PD} between prompt and delay events with cosmic muon contamination in reactor OFF and ON conditions.	215
5.10	Raw prompt and delay event rates during reactor ON and OFF periods in the month of December 2018 from miniISMARAN data.	215

5.11	Raw prompt and delay event rates during the complete shutdown in the month of March 2018 from miniISMARAN data.	216
5.12	ΔT_{PD} between raw events in different combinations after cosmic muon contamination removal in reactor OFF and ON conditions. . .	217
5.13	Difference of timestamps 2nd highest to highest energy deposit for prompt events with $N_{bars}=2$ or 3.	218
5.14	Difference between the timestamps of highest and the next highest energy PS bar for a 4 bar delay event.	218
5.15	Difference of timestamps of 3rd highest and highest energy deposit for prompt events with $N_{bars}=3$	219
5.16	Difference between the Z positions of highest and the next highest energy PS bar for a prompt event.	220
5.17	Difference between the Z positions of highest and the next highest energy PS bar for a prompt event.	221
5.18	Difference between the Z positions of highest and the next highest energy PS bar for a 4 bar delay event.	221
5.19	E_1/E_{max} ratio for prompt events with $N_{bars}=2$ or 3.	222
5.20	E_2/E_{max} ratio for prompt events with $N_{bars}=3$	222
5.21	Ratio of all the lower energies $E_1, E_2\dots$ to highest energy deposit (E_{max}) shown progressively in clockwise fashion, under reactor OFF conditions for ISMRAN delay events $N_{bars}=4,5$ and 6.	223
5.22	Ratio of all the lower energies to highest energy deposit shown progressively in clockwise fashion, under reactor ON conditions for ISMRAN delay events $N_{bars}=4,5$ and 6.	224

5.23 Comparison plot between data (symbols) and simulation (shaded region) for mini-ISMIRAN delay events. 225

5.24 Prompt delay pairs ΔT_{PD} distribution from mini-ISMIRAN data in ROFF and RON overlaid with mixed event datasets 226

5.25 ΔT_{PD} for reactor ON and OFF conditions fitted with double exponential. 229

7.1 The scaled up 9×9 PS matrix recording cosmic background in laboratory. 238

List of Tables

2.1	Specifications of the Dhruva reactor [67].	93
2.2	Energy released and cross-section for neutron capture in ISMRAN geometry	95
2.3	Properties of EJ200 scintillator [68]	98
2.4	Properties of ETL 9305KB PMT [69]	99
3.1	Detector parameters in simulation	137
3.2	Element-wise capture fractions for IBD neutron in ISMRAN, sorted in descending order.	153
3.3	Detection efficiencies of $\bar{\nu}_e$ events in ISMRAN with different prompt and delayed event selections.	159
3.4	Selection cuts and corresponding event efficiencies from embedded data set.	168

4.1	Efficiency, purity and false rejection performance for reco prompt events.	197
5.1	Background rates measured in mini-ISMARAN for various shielding configurations in reactor ON condition.	207
5.2	Systematic errors at different selection levels implemented for cut based analysis	228
5.3	Filtered $\bar{\nu}_e$ -like candidate events using cuts in mini-ISMARAN reactor data.	230

Chapter 6

Conclusions

Neutrinos make important tools for probing nuclear activity remotely, especially, for monitoring nuclear reactor cores. They can also act as messenger particles for probing otherwise inaccessible physical phenomena like supernovae, AGNs and GRBs. Additionally, some unsolved problems still exist in the neutrino physics sector such as existence of sterile counterparts of known neutrinos, the mass hierarchy of the neutrino mass eigenstates, whether neutrinos are Dirac or majorana fermions etc. To host such detection setups, nuclear reactors provide an ideal environment due to their high $\bar{\nu}_e$ s flux and controlled operation.

The ISMRAN experiment at Dhruva reactor facility of BARC, India, is a one of the efforts in this area. It is proposed for monitoring the natural uranium core of Dhruva using non-hazardous plastic scintillator volume of moderate scale.

The experiment has made substantial progress, with completion of a number of different activities for its development.

6.1 Studies of $\bar{\nu}_e$ using ISMRAN

Characterization of PS

The plastic scintillators used to form the ISMRAN matrix have been characterized for their energy and timing response. Detailed studies using known radioactive sources and natural background have been carried out for spectral matching of the PMTs and also globally amongst the different PS bars. The calibration derived for each PS shows a linear energy response over a broad scale ranging up to 20 MeV (cosmic muon). The presence of double ended PMT readout is useful to leverage the timing information from both and infer the timing and Z position. Parametrization for the timing to Z position conversion have been calculated. A data-taking exercise using known correlated γ -ray source ^{60}Co shows faithful reconstruction of its events and also points to use of sum energy and bar multiplicity or N_{bars} as event variables to select IBD events in the ISMRAN segmented volume.

6.2 Simulations in ISMRAN geometry

The plastic scintillator volume comprising of individual PS bars is replicated in monte-carlo simulations and IBD events are generated and transported using the GEANT4 simulation package. The reference spectrum and various parametrization and cross-section calculations are taken from known LEU phenomenology

analyses as part of references [80, 79, 48, 81]. These are used as the inputs to generate the IBD event and then standard kinematics derives the daughter product energies. The resulting event signatures are separately evaluated for prompt positron and delayed neutron for their sum energy and N_{bars} signature. The event detection efficiencies are evaluated from the simulated events using these variables.

Due to the requirement of in situ calibration, the matrix may have to be reduced to 9×10 and the remaining width can be divided into the gaps between bar columns. Although, the reduced volume will roughly reduce the $\bar{\nu}_e$ detection rates by 10% the events interacting are found to be detected with only 1% drop in efficiency even in the modified geometry with gaps.

6.3 Using MLP for improved detection efficiency

Machine learning has been gaining increased popularity among HEP community for filtering signal events from background dominated samples, especially in collider experiments. Although the neutrino detection process is not as dynamic and lacks direct trigger information as in colliders, the task of looking for specific tracking or energy signatures which are mimicked by other backgrounds is the same. ISMRAN aims to adopt the power of machine learning to filter signal events as the DAQ system uses only minimum thresholds for online triggering and records much of the raw data for possibly complex and involved analysis needed for $\bar{\nu}_e$ detection.

Using a standard feed-forward ANN in the form of a multi-layer perceptron (MLP) having two hidden layers and the capability for Bayesian error correction

(MLPBNN), a highly efficient prompt event classification is shown to be possible for the full ISMRAN volume. As part of this process, a new and effective variable – D_k is devised, which is a weighted combination of both the base variables sum energy and N_{bars} . This framework yields about 91% efficient classification data with close to 73% pure output sample. This is a positive sign for the ISMRAN setup as it suffer from huge efficiency losses when only cut based analysis is considered.

6.4 Analysis results from the prototype - miniISMRAN

The prototype detector – miniISMRAN, which is a 16 PS bar matrix, is a precursor to the ISMRAN detector. This prototype serves as a test bed for the full detector operation as it allows for formalizing and streamlining of the various procedures to be adopted for setting up of ISMRAN. Operation of this prototype in the reactor environment for long duration with minimal personnel supervision has established the suitability of a near-field detector like ISMRAN for long-term unmanned operation inside the reactor hall. An elaborate background measurement campaign has been carried out both in laboratory and reactor environments with miniISMRAN matrix. A detailed analysis framework has been developed to extract the IBD candidate events and their rates in the miniISMRAN data are also calculated.

Summary

Monitoring of nuclear reactor cores via the measurement of their emitted $\bar{\nu}_e$ flux, offers a convenient and non-intrusive solution for tracking changes in their power and fuel composition. A preferred monitoring detector is expected to be an above ground, moderate scale (few tonnes) and non hazardous setup easily operated by non-scientific personnel. Additionally, such a detector positioned at short baselines from different reactor core types can also search for the hypothesized $\sim 1\text{eV}^2$ scale oscillations of these $\bar{\nu}_e$ s into sterile states.

The Indian Scintillator Matrix for Reactor AntiNeutrinos (ISMARAN) – a 1 m^3 and ~ 1 ton scale plastic scintillator (PS) detector is proposed with this dual objective in view and currently under development at the Bhabha Atomic Research Centre (BARC) India. It is a segmented volume of 100 PS detectors in a 10×10 matrix and uses high sampling rate waveform digitizers for its DAQ. The γ -rays and neutrons in the reactor environment will be shielded using a 10 cm thick Pb and 10 cm thick borated polyethylene (BP) shield. A proof-of-

principle measurement is planned at the Dhruva research reactor facility at ~ 13 m from its natural uranium core. To streamline the characterization procedure and to quantify the natural and reactor backgrounds, a prototype detector – miniISMARAN having 16 PS detectors in a 4×4 matrix was operated both in laboratory and reactor environment.

The objective of monitoring the reactor involves precise understanding of the detector response and inverse beta decay (IBD) interaction signature. Characterization studies are therefore performed as part of this thesis work to derive the energy scale, resolution of PS and also the timing response. Simulations done in ISMRAN geometry to study – shielding effectiveness, IBD event signature, cosmic backgrounds and detection efficiencies, are also presented. Using neural networks to classify simulated signal and background data, it is shown that significant improvement in detection efficiency is achievable for ISMRAN geometry. Background measurements from miniISMARAN matrix and efficient γ -ray and neutron detectors in reactor environment are presented, followed by a thorough analysis of 4 months of miniISMARAN data taken in reactor using various levels of selections. The identified $\bar{\nu}_e$ -like events from this analysis show reasonable agreement with the prediction but with large uncertainties. The remaining PS bars needed to setup the full scale ISMRAN have been characterized in laboratory and currently measuring cosmogenic backgrounds before their planned move to reactor in the first quarter of next year.

Chapter 1

Neutrino

1.1 Early developments

Neutrino is perhaps the most intriguing member of the standard model of particle physics. It was originally postulated by Wolfgang Pauli in 1930, to essentially rescue the principles of conservation of energy and spin angular momentum in beta decay of nuclei. He hypothesized that a chargeless spin- $\frac{1}{2}$ particle existing inside the nucleus is emitted with the electron in the beta decay. He labeled his particle as - ‘neutron’ on the lines of proton and electron. It was such an adhoc solution that Pauli himself considered his postulate as a “desperate remedy” [1]. Later in 1932, when J. Chadwick discovered a neutral particle inside nucleus, it was thought to be Pauli’s particle [2]. But the new particle was too massive as

compared to the postulated mass of neutrino at that time. It wasn't until 1934, that Enrico Fermi put these elusive particles on a strong theoretical basis when he proposed his theory of beta decay [3]. Also, it was he who christened the particle as 'neutrino' (the little neutral one), to signify its properties of neutrality and tiny mass.

1.2 Standard model of particles

The standard model of particle physics has been a huge success in explaining the fundamental building blocks of the physical world. Although the model doesn't include Gravity, it successfully explains the other three fundamental forces of

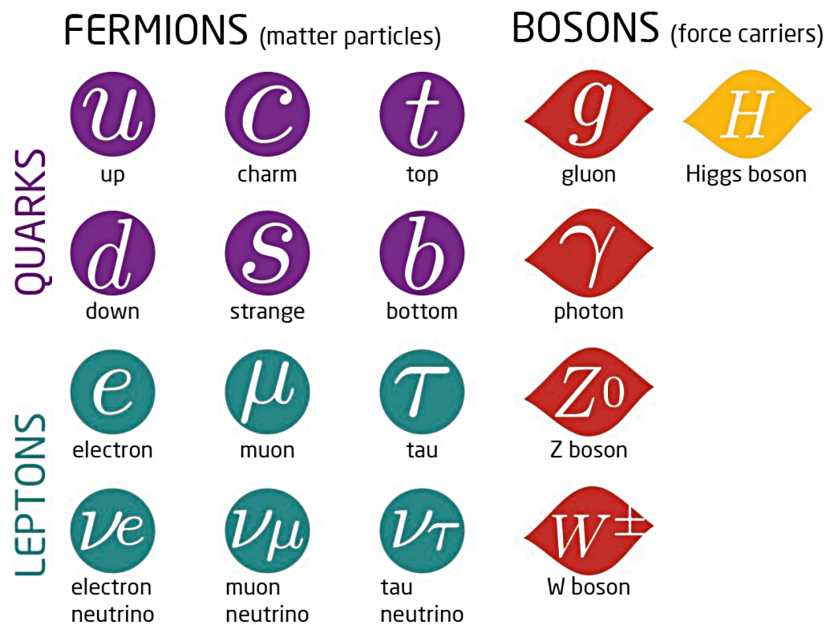


FIGURE 1.1: The standard model of particle physics. (Image source [4])

nature, namely - Electromagnetic, Strong and the Weak force. The model can

be broken down into matter particles which are expected to follow the Fermi-Dirac statistics and called the ‘Fermions’ while the force carrier particles follow the Bose-Einstein statistics and are referred to as the ‘Bosons’. The fundamental fermions are further classified as the quarks and leptons, while the force mediating bosons are - photons for electromagnetic force, gluons for strong force and finally Z and W^\pm bosons for weak force, as listed in Fig 1.1. These fundamental particles together explain all visible matter and their interactions. An important property of all particles is their mass. The mechanism responsible for giving the mass to all the fermions and the W and Z bosons is called the Higgs mechanism [5, 6, 7] and the smallest quanta of the Higgs field called the Higgs boson forms the last ingredient of the standard model. This particle was detected recently at CERN’s large hadron collider (LHC) by the ATLAS [8] and CMS [9] collaborations.

1.2.1 Neutrino in Standard Model

For the first 30 years since the Pauli’s postulate, while the standard model was still in nascent stages, the neutrino produced in the beta decay mechanism was considered the only such particle. But later with the development of electroweak theory and subsequent discoveries of the 2nd and 3rd generation μ and τ leptons [10, 11] (heavier counterparts to electron) the model for neutrinos became more clear. Due to the lepton number conservation rule, these new leptons needed the existence of their own associated neutrinos. Thus, in the fully formed standard model, these new neutrinos were also incorporated.

Putting these facts together, the neutrinos can be summarized as spin- $\frac{1}{2}$ fermions which come in three ‘flavours’. These are the ν_e, ν_μ, ν_τ neutrinos which are ob-

served to have left handed helicity and their corresponding anti-particles $\bar{\nu}_e, \bar{\nu}_\mu, \bar{\nu}_\tau$ with right handed helicity. They interact only via the weak interaction mediated by the heavy W^\pm and Z^0 bosons. Their individual masses are more than 500,000 times smaller than the mass of electron [12]. Neutrinos are the second most abundant particle in the universe after the photon. Their interaction with matter is so weak that a 1 MeV neutrino has a mean free path of 1 light year in Lead.

1.3 Sources of neutrinos

Neutrinos are produced in weak interactions and since these processes are crucial to most natural phenomena they are about 10^{10} times more abundant in the universe than proton, neutrons and electrons. Neutrinos are also produced through man-made sources where their rate and energies may be controlled as per experimental needs. Thus, we can broadly classify neutrino sources as follows:

- Natural sources
- Man-made sources

The following Fig 1.2 collates the spectral information of the various neutrino sources in a single plot. It is easily seen that, not only do a host of different phenomenon emit neutrinos but these neutrinos span sub-eV to EeV energy scales.

The discussion that follows covers the natural and man-made sources and the properties of their emitted neutrinos in brief.

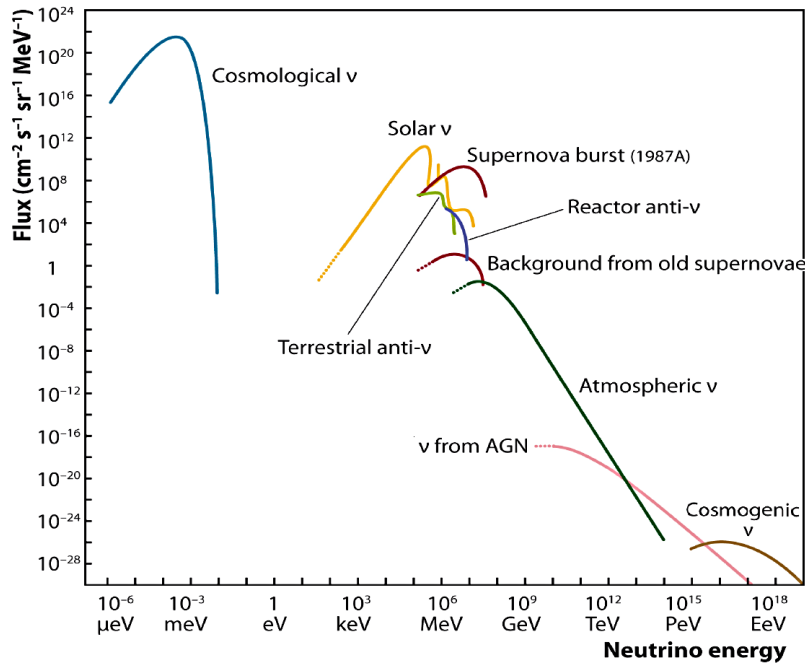


FIGURE 1.2: Neutrino spectra from various natural and man-made sources [13].

1.3.1 Natural sources

Earth's crust

The discovery of radioactivity and radioactive elements found in some rocks and salts extracted from the earth's crust marked the beginning of a new era in physics. The quest to understand this new phenomena led to the theory of beta decay and subsequently to the theory of weak force. As mentioned earlier, beta decay is one of the radioactive processes and it produces an electron and a neutrino. With improved understanding of the process, it was realized that this neutrino is actually $\bar{\nu}_e$. Beta decay is basically a nuclear transformation wherein the atomic number Z of a nucleus changes by one unit while keeping the mass number A same:

$$\begin{aligned}
n &\rightarrow p^+ + e^- + \bar{\nu}_e \\
\Rightarrow {}^A_Z X &\rightarrow {}^A_{Z+1} Y + e^- + \bar{\nu}_e \quad (\beta^- - \text{decay}) \quad (1.1) \\
p^+ &\rightarrow n + e^+ + \nu_e \\
\Rightarrow {}^A_Z X &\rightarrow {}^A_{Z-1} Y + e^+ + \nu_e \quad (\beta^+ - \text{decay})
\end{aligned}$$

Since the β^- - decay is the dominant process, most geoneutrinos are $\bar{\nu}_e$. The isotopes ^{238}U , ^{235}U , ^{232}Th and ^{40}K are the major contributors to their flux. About $\sim 6 \times 10^6 \bar{\nu}_e \text{ cm}^{-2} \text{ s}^{-1}$ are produced, most having energy $< 1 \text{ MeV}$. Only the highest energy neutrinos from ^{238}U , ^{232}Th can exceed the 1.8 MeV threshold for IBD, consequently, ^{40}K geoneutrinos can't be detected in current experiments. New generation of specially designed experiments using interactions like radiochemical reaction or elastic scattering on electrons having better cross-section, lower threshold energy and possibly directionality detection are planned for geoneutrino detection and mapping.

Solar neutrinos

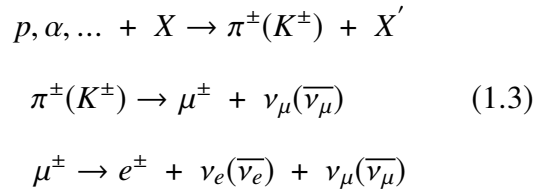
Stars form when a huge mass of gas, predominantly hydrogen, is smashed together by gravity, to create a plasma hot enough to trigger fusion reaction. This reaction leads to emission of ν_e flavoured neutrinos. Because of this reason, our Sun shines not only in photons but also in ν_e particles. The pp chain and the CNO cycle are the two major fusion chains producing energy inside Sun. Both chains essentially fuse protons into helium nucleus as follows:

$$4p^+ \rightarrow {}^4\text{He} + 2e^+ + 2\nu_e \quad Q \sim 26\text{MeV} \quad (1.2)$$

Every second a total of $\sim 2 \times 10^{38}$ ν_e are produced inside the Sun, of which only about $\sim 6 \times 10^{10}$ ν_e in energy range $E \leq 0.42$ MeV and $\sim 5 \times 10^6$ ν_e in energy range $0.8 \text{ MeV} \lesssim E \leq 15$ MeV are incident per second on each cm^2 area of the earth's surface, due to drop in intensity over the distance.

Atmospheric neutrinos

Neutrinos are also produced when high energy cosmic rays, primarily the protons and light nuclei ejected from violent stellar phenomena, scatter hard on the nuclei of the upper earth atmosphere. This is a multi step process wherein the first scattering produces pions and kaons with a preference towards the positively charged particles. A majority of charged pions decay to muons and their neutrinos, while a significant fraction of kaons first decay to pions which can then produce the muons and the neutrinos. Further, many of these muons themselves can decay to electrons producing both muon and electron neutrinos. This whole chain of reactions can be summarized as :



First known account of atmospheric neutrino detection was from the KGF experiment in India parallelly with the ERPM experiment in South Africa [14, 15]. The spectrum of these neutrinos ranges from about 30 MeV to 3000 GeV with flux $\sim 10^{-1} \text{cm}^{-2} \text{s}^{-1}$. Numerous experiments have studied the atmospheric neutrinos. Recently, ICAL a 50 kT magnetized iron calorimeter detector under the India based neutrino observatory (INO) project is planned for gaining further understanding of their behaviour [16].

Supernova neutrinos

Neutrinos and anti-neutrinos of all flavours and covering a range of energies from 10–30 MeV are emitted when a star with enough mass (1.4 times solar mass) goes supernova. These neutrinos carry almost all the energy of the explosion and about $\sim 10^{58}$ of these are emitted within a time period of only 10 seconds. While the photons can take hours or even days to emerge from stellar envelope, neutrinos come out quite instantaneously and therefore are more helpful in understanding the dynamics of collapse from very early on in the process.

The supernova of 1987 - ‘SN 1987A’, that occurred in the large Magellanic cloud within our galaxy was observed by the atmospheric neutrino detectors. About 25 neutrino events were registered across 3 different detectors within 12 seconds and helped confirm our basic understanding of supernova phenomenon [17].

Big Bang neutrinos

The big bang theory predicts a cosmic background of neutrinos much like the CMB photons, as the event itself is supposed to have produced more neutrinos than any other phenomenon. These are the so-called relic neutrinos with an expected density of about 113 cm^{-3} for each neutrino flavour and energies well below 1 eV, making it extremely difficult to detect with current generation detectors.

Ultra High Energy Sources

These are the sources of neutrinos which cannot exist on earth because of the extremely violent and energetic phenomenon needed to produce them. Such ultra high energy neutrinos are produced in the so-called gamma ray bursts (GRBs) and Active galactic nuclei (AGN) jets and can reach energies $> 10^{14}$ eV and requiring detectors, alternatively called neutrino telescopes, of effective area $\sim 1 \text{ km}^2$ [18].

1.3.2 Man-made sources

Accelerator neutrinos

Bombarding of high energy protons from accelerators onto low Z target produces high energy pions which can then be focused and allowed to decay into muons and neutrinos of muon and electron flavours. An array of high Z absorbers can then stop these muons and produce a pure beam of neutrinos. Higher control on the beam parameters reduces the neutrino flux uncertainties making this technique suitable for higher precision neutrino experiments. There is some contamination of electron flavour neutrinos but it can be accounted for by using a near and far detector arrangement. Neutrinos of energies ranging from 30 MeV to 30 GeV can be produced by accelerators.

Neutrino beams can be classified into Wide band beam (WBB), Narrow band beam (NBB) and Off-axis beam (OAB). WBB has highest flux as it includes almost all of the produced neutrinos but suffers from a wide spread in energy and contamination from other flavours. Narrow band beam on other hand rejects pions produced in wider angles away from axis and hence results in narrow energy

spread with downside of much reduced flux. Off-axis beam is a useful scenario where detector is positioned off-axis to use pion decay kinematics and getting energies in a very narrow range independent of the pion's boost and very low contamination of other flavours.

Nuclear explosions

Nuclear explosion produces large numbers of neutrinos. Fission based bombs produces $\bar{\nu}_e$ and fusion based bombs produce both $\bar{\nu}_e$ and ν_e . Interestingly, these nuclear explosion neutrinos were the first choice for C. Cowan and F. Reines from LANL for their neutrino detection experiment. In the current scenario, where development of more and more nuclear weapons is threatening the global security, a detection strategy using these explosion neutrinos can provide a warning of nuclear tests being performed.

Nuclear reactors

Nuclear reactors are probably the most useful source in terms of potential for new discovery and cost effectiveness in conducting an experiment. The core of a nuclear reactor is the most abundant man made source of neutrinos. A standard $\sim 1 \text{ GW}_e$ power output reactor can produce $\sim 10^{20} \bar{\nu}_e \text{ s}^{-1}$. As all of the neutrinos are from beta decay of daughter products of fission, no other flavour of neutrinos is produced, hence no contamination. The flux of these neutrinos extends only up to about an energy of 10 MeV, but beyond 7 MeV the statistics are sparse.

1.4 The Neutrino voyage : From discovery to applications

Neutrino physics has been driven more by the experiments than theory, since existence of neutrinos themselves challenged many of the the accepted frameworks of theoretical physics right from the beginning. The standard model considered neutrinos to be massless, which later turned out to be wrong. The progress of neutrino physics can be better understood from the point of view of experiments, starting from those which established their identity to latter ones studying their behaviour. These experiments usually explore neutrinos based on their sources and the associated characteristics like spectrum and intensity. The detection schemes and overall design of the experiment differs based on the above considerations. Neutrinos being chargeless leptons, interact solely via weak interactions and consequently the detection experiments depend only on the resulting charged daughter particles or atomic transmutations of these interactions in the medium. The electron capture experiment by Rodeback and Allen is amongst the first known experiments to indirectly test the existence of neutrinos. The detection scheme involved accurately measuring the recoil of ^{37}Cl produced from electron capture by ^{37}Ar nucleus which also produced a ν_e . The recoil of the ^{37}Cl nucleus was accurately measured and found in keeping with the production of an accompanying neutrino, based on two-body kinematics [19].



Another such example is the Goldhaber experiment to determine the helicity

of neutrinos [20]. Instead of ^{37}Ar , this time it was the ^{152}Eu nucleus undergoing electron capture. The produced ^{152}Sm is in the excited state and emits a forward photon of 961 keV whose circular polarization is measured.



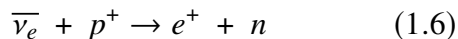
This helps determine the photon's helicity, which, owing to the experimental arrangement, is the same as the helicity of the neutrino. The outcome of the experiment confirmed the helicity(\mathcal{H}) of ν_e to be -1 i.e. left-handed.

1.4.1 The Discovery of neutrino - 'Project Poltergeist'

Direct detection of neutrinos is an equally formidable task due to the extremely small interaction cross section of neutrino (typically $\sim 10^{-44} \text{ cm}^2$). The challenge of direct detection of neutrinos was taken up by F. Reines and C.Cowan from LANL at the Hanford nuclear reactor site in California, USA. To quote an interesting anecdote regarding the above proposal, Pauli himself is said to have advised against granting the funds for the experiment as he was skeptical that neutrino can ever be detected. But, his letter reached late and the experiment was already given a go-ahead. The Hanford site, however, suffered problems of huge background radiation forcing the set up to be moved to an underground site at the Savannah river plant. It was here that the discovery of neutrino was made in 1956 [21] and the physics Nobel prize of 1995 was awarded to this discovery. This experiment relied on the inverse beta decay (IBD) reaction for neutrino detection, which has since been the most popular mechanism for detection of

1.4. THE NEUTRINO VOYAGE : FROM DISCOVERY TO APPLICATIONS 55

reactor neutrinos. The reaction occurs as follows :



The detector was a sandwich like arrangement with two water tanks filled with CdCl₂ between three liquid scintillator (LS) tanks to detect positron annihilation and neutron capture γ -rays in delayed coincidence. The recording of pulses were done on the oscilloscopes connected to the PMTs attached to the scintillator tanks. The concentration of CdCl₂ was adjusted so that expected time delay between prompt and delayed pulses was restricted to few μ s. Indeed such signals were observed and there rates agreed with expectations.

The technique of detection in the Cowan Reines experiment was to use a scin-

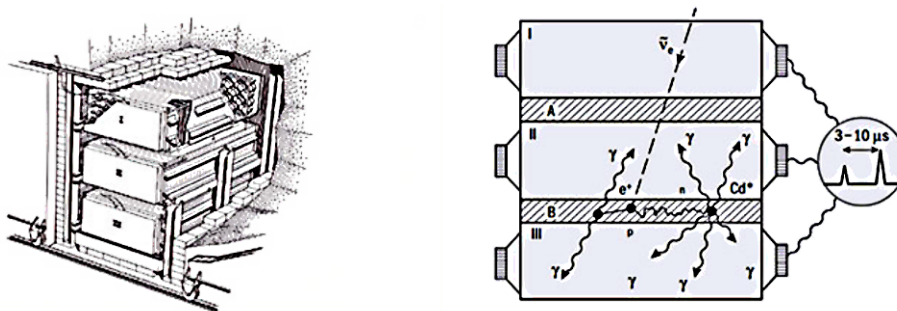


FIGURE 1.3: **Left:** The detector used at the Savannah River plant. **Right:** Visualization of a prompt and delayed event in this detector [22].

tillating material to convert the energy of the particle interaction into detectable signal (scintillation photons) for the readout (PMT). Such a detector can therefore be categorized as a scintillator detector. Since then, there have been many such experiments, particularly looking for β^- -decay neutrinos mostly from reactors. The Kamioka Liquid Scintillator Antineutrino Detector (KamLAND), in Japan is a relatively recent example of a scintillator based reactor neutrino detector.

1.4.2 Discovering the μ and τ flavour neutrinos: AGS and DONUT experiments

The discovery of ' μ ' lepton or muon by C.D. Anderson and S.Neddermeyer in 1936 [11] led to many conjectures about the neutrinos produced in their decay. The task of detecting these neutrinos was undertaken at the AGS accelerator facility of Brookhaven National Laboratory in USA, by Schwartz, Lederman and Steinberger. It is referred to as the AGS Neutrino experiment. The prime goal of this experiment was to check whether the neutrino produced due to muon decays and those produced from beta decay are same or different. The standard scheme of colliding accelerated protons on low Z target was used to produce pions and kaons which would then decay into muons and neutrinos.

The detector was a spark chamber which helped identify a charge particle through tracking of the sparks produced. Photographs of the chamber were taken to register the tracks, when the trigger signal due to the beam was received. If a muon is produced due to the neutrino interaction inside the chamber, a long track of sparks is seen due to minimum ionization while an electron would leave a local cluster of sparks due to electromagnetic shower. 34 long track events and only 6 shower like signature were observed strengthening the argument that neutrinos from muon decay were not the same as those from beta decay. Thus were discovered the $\nu_\mu/\bar{\nu}_\mu$ neutrinos in 1962 [23] and this discovery was awarded the Nobel Prize of 1988.

However, it took more than 30 more years for tau leptons (τ) to be discovered. Their existence was expected considering that the third generations of quarks were already discovered. Finally, in 1977 Martin Lewis Perl and his colleagues,

prominently Yun-su Tsai, at SLAC and LBL, USA, discovered this particle at the $e^+ - e^-$ collider in SLAC [24]. The discovery of τ implied existence of its neutrino, i.e. $\nu_\tau/\bar{\nu}_\tau$. It was in the year 2000, that the DONUT (Direct Observation of Nu Tau) experiment at Fermilab, observed these neutrinos using the Tevatron proton beam. The technique of looking for charged particle tracks in nuclear emulsion target was used in this discovery. Scintillators, calorimeters and drift chambers were also part of the detector to record energy and tracking information for both lepton and hadron daughter products. The tracks and identity of the charged particles were reconstructed later by joining the recorded dots in the set of emulsion plates and the energy information from scintillator planes and drift chambers. A typical tau-neutrino event in the emulsion was expected to have no incoming mother track and a short τ track due to its small lifetime followed by a 'kink' to signify tau-decay into a daughter electron, muon or hadron (mostly pions) which had its own signature. The final results presented in 2008 reported 9 such events in a sample of 578 neutrino events [25].

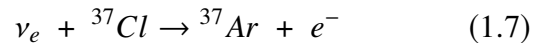
1.5 Neutrino oscillations : Anomalies and experimental results

The period from 1960s onward, can be considered the second epoch of neutrino experiments. A number of neutrino detection experiments reported the observation of a deficit in their flux as compared to expectation. Later, with improvements in detection techniques and greater precision, the next generation experiments confirmed these observations and verified the theoretical claims that

neutrinos changed their flavour. This behaviour had similarities with quark oscillations, and hence this phenomenon came to be termed as ‘neutrino oscillations’. The discussion that follows, outlines the progress in understanding of neutrino oscillations with the aid of experimental inputs.

1.5.1 Solar Neutrino problem

It was known that the fusion reactions inside the Sun produces a large number of neutrinos. The calculations for their flux was given by J. Bahcall who had important contributions in developing the ‘standard solar model’ [26]. The experimentalist R. Davis proposed an experiment in 1964, to detect these neutrinos at the Homestake Gold Mine in Lead, South Dakota, USA. The experiment is referred to as the ‘Homestake experiment’. The detection medium used was perchloroethylene or ‘cleaning liquid’. 400000 L of this chemical was filled in a cylindrical steel tank, 15 m long and with a diameter of 6 m. The technique is called the ‘radiochemical technique’ of neutrino detection as it relied on the interaction of solar neutrinos with ^{37}Cl to produce ^{37}Ar , like a reversed electron capture, as follows :



The ^{37}Ar atoms produced were counted every month-end and such repeated measurements showed counts to be only one-third of the expectation due to the solar model. Due to the unexpected outcome the experiment as well as the model were both in question for quite sometime before other experiments started looking into this anomalous result [27].

1.5.2 Confirmation of Solar neutrino oscillation

Around late 1970s, a new set of experiments looking for nucleon decay reported their findings on the solar neutrino flux, as neutrinos formed a background in such experiments. One such experiment called the kamioka nucleon decay experiment or ‘KamiokaNDE’ was looking for proton decays in a 3 kT purified water detector. The detector was a 16 m height and 15.6 m diameter cylindrical tank, located about 1 km underground with 2700 m.w.e of overburden to reduce cosmic ray backgrounds. The detection signature was high energy positrons and γ -rays due to π^0 , produced from proton decay. The detection technique was to look for Cerenkov photons produced by relativistic charge particles traversing through ultra-pure water using highly sensitive PMTs and called ‘Water-Cerenkov’ method. The topology of Cerenkov emission is reconstructed from multiple PMTs and used for particle ID. A typical electron/ γ event would produce a fuzzy ring due to electromagnetic shower, while a muon event would leave a sharp circular ring due to their MIP-like energy loss. A great advantage of the Cerenkov technique is that the direction of Cerenkov photons help reconstruct the charge particle’s boost and therefore pin-point the source of the incoming particle. Although, the observation of proton decay was the primary goal, the detector had potential for neutrino detection but required more radiopure water and advanced electronics which were introduced in subsequent phase-II and III operation. The subsequent measurements saw deficit in the solar neutrino flux, although about 50 % when the compared on the ^8B neutrinos from Sun [28]. This result was confirmed in later experiments like SAGE (Russia) and GALLEX (Italy), both using radiochemical technique of detection, although with slightly

different percentages [29, 30].

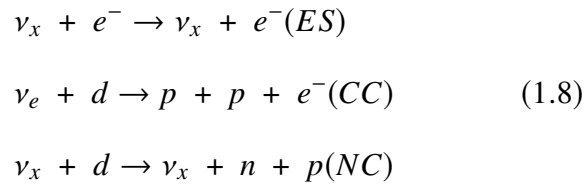


FIGURE 1.4: A schematic of Sudbury Neutrino Observatory 2039 m below the surface in a nickel mine near Sudbury, Ontario [31]

SNO experiment: Observation of neutral current events

The convincing results which put the ‘solar neutrino problem’ to rest came from another water Cerenkov detector at the Sudbury Neutrino Observatory (SNO). It is located 2 km (6010 m.w.e) underground in a nickel mine in Ontario, Canada. The unique advantage of this detector was the use of 1000 tons of heavy water (D_2O) instead of light water, which allowed it to simultaneously be sensitive to three different types of neutrino interactions and hence to the different flavours. The heavy water is contained inside a 6 m radius acrylic vessel instrumented with

9600 PMTs. A schematic of the observatory can be seen in the Fig 1.4. The outside volume was filled with light water which detected cosmic background. The Neutral current scattering (NC) could detect all the flavours, Elastic scattering (ES) which too could detect all flavours but 6 times more sensitive to electron neutrinos, Charge Current scattering (CC) only for the electron type neutrinos.



In 2001, owing to its above capability, SNO experiment could confirm the neutrino oscillations by comparing counts of both the total and the unoscillated neutrinos [32]. The experiment detected ^8B electron neutrino flux of $\sim 1.76 \times 10^6 \text{cm}^{-2}\text{s}^{-1}$ and other flavours at $\sim 3.41 \times 10^6 \text{cm}^{-2}\text{s}^{-1}$. The total flux coming from NC events was at $\sim 5.09 \times 10^6 \text{cm}^{-2}\text{s}^{-1}$ which was a strong evidence for electron neutrino oscillation and consequently that neutrinos had mass.

1.5.3 Atmospheric Neutrino Anomaly

On similar lines as the ‘solar neutrino problem’, experiments studying atmospheric neutrinos detected a deficit in the measured flux. The ratio N_{ν_μ}/N_{ν_e} from charge particle decays in cosmic ray showers, is expected to be around 2 for energies up to 1 GeV and increase for higher energies. One of the experiment to detect nucleon decay called the ‘IMB’ reported lesser muon decay events than expected [33], which was later confirmed by the kamiokande experiment, both of them being water cerenkov detectors [34]. This deficit came to be known as the

‘Atmospheric neutrino anomaly’. Although the kamiokande experimental group were positive that the anomaly was not due to detector or background related problem, yet they did not comment on the issue at the time. But it was evident that the solar and the atmospheric neutrino deficit were pointing to the same phenomenon.

Super-K results

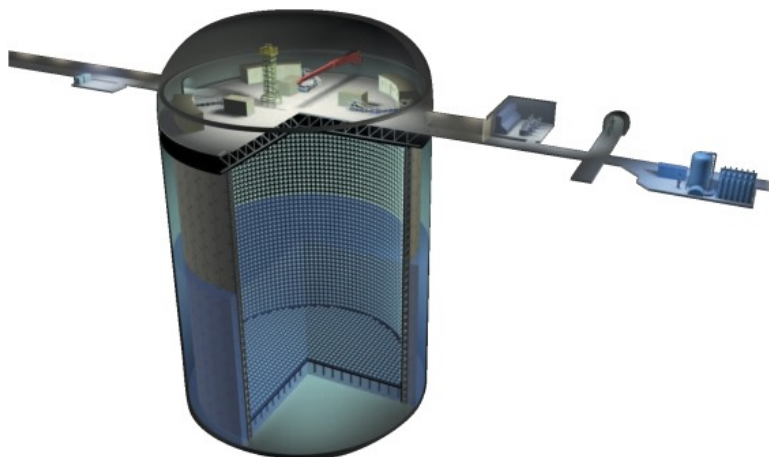


FIGURE 1.5: A cutaway schematic of Super kamiokande detector. The inner and outer detector and the dome with the front end electronics and calibration equipment are visible [35].

The Super Kamiokande (Super-K) detector, a scaled up version of the Kamiokande detector, started taking data in 1996. Super-K had 50kT of ultra-pure water filled inside a cylindrical volume of height 41.4 m and diameter 39.3 m and instrumented with 13,142 PMTs of 20 inch diameter(Fig 1.5). With only two years of data Super-K was able to confirm the atmospheric neutrino oscillations. They found a zenith angle dependent deficit in muon neutrino flux which could not be

explained by experimental biases and prediction uncertainties but found consistent with $\nu_\mu \rightarrow \nu_\tau$ oscillations. More importantly improved statistics from longer operation of Super-K even showed a clear wave like pattern in their results in 2004 [36]. Later experiments using accelerator sources and different detector technologies also observed these oscillations.

1.6 Theoretical background of neutrino oscillation

The phenomenon of flavour oscillations was not new to particle physics when neutrinos came along. The oscillations of neutral particles like $K^0 - \bar{K}^0$, $B^0 - \bar{B}^0$, $B_s^0 - \bar{B}_s^0$ and so on, were already observed. This led to the theory of quark oscillations and derivation of their mixing matrix called the ‘CKM’ matrix. Thus when different anomalies surfaced in the detected neutrino flux, the natural course of action was to turn to this existing theoretical framework with appropriate modifications.

The soviet physicist, B. Pontecorvo was the first to introduce the concept of oscillations in the neutrino sector in the 1950s. He based his argument by drawing analogy to the $K^0 - \bar{K}^0$ oscillation already established from cosmic ray observations [37]. But the initial framework postulated particle-antiparticle oscillations in only the electron neutrino flavour. Later with addition of muon and ν_μ he extended it to the two flavour scenario and also included the right handed states. In 1962, almost parallely to the two flavour theory of Pontecorvo, an independent model of neutrino oscillation was developed by Z. Maki, M. Nakagawa and S. Sakata hypothesizing oscillations amongst the muon and electron neutrino flavours [38]. It wasn’t until the 1970’s that a comprehensive theory of neutrino

oscillations was formulated with mixing among different flavours on the lines of what was observed in the quarks.

According to this theory, neutrino flavor eigenstates can be represented using the mass eigenstates as:

$$|\nu_\alpha\rangle = \sum_i U_{\alpha i}^* |\nu_i\rangle \quad (1.9)$$

where $\alpha = e, \mu, \tau$ represent the flavour eigenstates and $i = 1, 2, 3$ runs over the three mass eigenstates. The full mixing matrix for the three flavours has the form:

$$U = \begin{pmatrix} c_{12}c_{13} & s_{12}c_{13} & s_{13}e^{-i\delta} \\ -s_{12}c_{23} - c_{12}s_{23}s_{13}e^{i\delta} & c_{12}c_{23} - s_{12}s_{23}s_{13}e^{i\delta} & s_{23}c_{13} \\ s_{12}s_{23} - c_{12}c_{23}s_{13}e^{i\delta} & -c_{12}s_{23} - s_{12}c_{23}s_{13}e^{i\delta} & c_{23}c_{13} \end{pmatrix} \quad (1.10)$$

where $c_{ij} = \cos \theta_{ij}$, $s_{ij} = \sin \theta_{ij}$ and δ is ‘Dirac phase’ characterizing CP violation. Here we are assuming neutrinos are Dirac particles, hence majorana phase terms have been ignored. The above matrix is called the PMNS matrix to honor its founders.

The conversion probabilities from one flavour (α) to another (β) can be derived based on this matrix as follows:

$$P_{\alpha \rightarrow \beta} = |\langle \nu_\beta | \nu_\alpha(t) \rangle|^2 = \left| \sum_i U_{\alpha i}^* U_{\beta i} e^{-im_i^2 \frac{L}{2E}} \right|^2 \quad (1.11)$$

or more conveniently,

$$\begin{aligned}
 P_{\alpha \rightarrow \beta}(L, E) = \delta_{\alpha\beta} - 4 \sum_{i>j} \Re \left(U_{\alpha i}^* U_{\beta i} U_{\alpha j} U_{\beta j}^* \right) \sin^2 \left(\frac{1.27 \Delta m_{ij}^2 L}{4E} \right) \\
 + 2 \sum_{i>j} \Im \left(U_{\alpha i}^* U_{\beta i} U_{\alpha j} U_{\beta j}^* \right) \sin \left(\frac{2.54 \Delta m_{ij}^2 L}{2E} \right)
 \end{aligned} \quad (1.12)$$

where $\Delta m_{ij}^2 \equiv m_i^2 - m_j^2$ with $i, j = 1, 2, 3$ and L is the oscillation length in meters while E is the energy of neutrino in MeV.

1.6.1 Two flavour mixing of neutrinos

The solar neutrino experiments mostly deal with Δm_{21}^2 mass difference while the atmospheric neutrino experiments are sensitive to Δm_{32}^2 difference, due to the energies and baselines involved in their oscillations. Thus in most cases the neutrino mixing can be effectively reduced to two flavour calculations. The effective mixing matrix then depends on a single parameter θ and there is a single mass-squared difference Δm^2 . The simplified mixing matrix and conversion probabilities then become:

$$U = \begin{pmatrix} \cos \theta & \sin \theta \\ -\sin \theta & \cos \theta \end{pmatrix} \Rightarrow P_{\alpha \rightarrow \beta} = \sin^2 2\theta \sin^2 \left(\frac{1.27 \Delta m^2 L}{4E} \right) \quad (1.13)$$

The oscillation probabilities calculated up until now are with the assumption that the medium is essentially vacuum, and hence called ‘Vacuum oscillation probabilities’.

1.6.2 Matter oscillations of neutrinos

Once we move to the real scenario of neutrino oscillations in matter, a few additions need to be made to the mixing matrix. The modifications are brought on by the potential that neutrinos face inside matter medium due to coherent forward elastic scattering with electrons and nucleons. These reflect in the mixing matrix in the form new effective mixing angles θ_M leading to enhanced oscillations. Work on matter oscillations by S.P. Mikheev, A.Yu. Smirnov and L. Wolfenstein pointed out the existence of resonant flavour transitions when neutrinos propagate through matter with varying density, later labeled as the MSW effect [39, 40]. This finding explained the large oscillations observed in the solar neutrino sector.

1.6.3 Hierarchy in the neutrino mass eigenstates

The conversion/survival probabilities of oscillating neutrinos depend on the mass-squared differences $\Delta m_{21}^2, \Delta m_{31}^2, \Delta m_{32}^2$ but not on the actual masses m_1, m_2, m_3 . This implies the neutrino oscillation data from experiments performed till date may not be sufficient to comment on their absolute masses or even the ordering of the neutrino masses. Conventionally, the ordering for the two masses in solar neutrino sector is assumed: $m_2 > m_1$ so that Δm_{21}^2 is > 0 . This leaves us with two possibilities:

- Normal mass hierarchy (NH) i.e. $m_3 > m_2 > m_1$ which also implies $\Delta m_{32}^2 > 0$.
- Inverted mass hierarchy (IH) i.e. $m_2 > m_1 > m_3$ which implies $\Delta m_{32}^2 < 0$.

Whether Δm_{32}^2 or Δm_{31}^2 are positive or negative is unknown, but what is known is that $|\Delta m_{21}^2| < \Delta m_{31(32)}^2$ as Δm_{32}^2 and Δm_{31}^2 are almost equal. Determining the sign of Δm_{32}^2 is also one of the prime goal of current and future neutrino oscillation experiments.

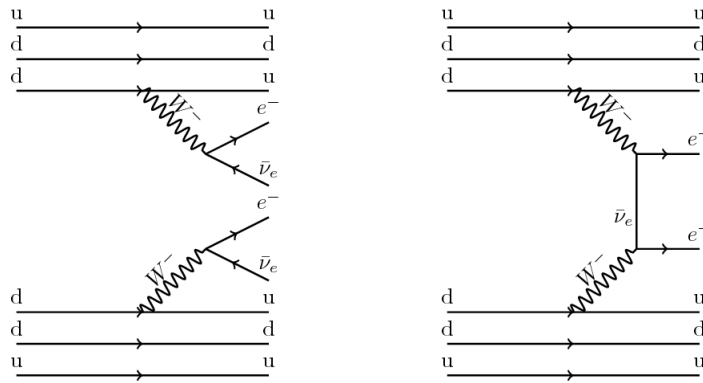


FIGURE 1.6: Feynman diagram of double beta decay for **Left:** Dirac neutrinos and **Right:** Majorana neutrino cases [41].

1.7 Are neutrinos majorana or Dirac particles ?

The fermions which are part of the standard model are all considered ‘Dirac’ particles except neutrinos, which can alternatively be Majorana fermions as they satisfy the primary requirement of being neutral. Ettore Majorana, in the year 1937, showed that beta decay could be explained without having to invoke negative energy states as in the case of Dirac fermions. This approach has an important consequence in the fact that neutral majorana fermions are their own anti-particles. Neutrino-less double beta decay (NDBD) reaction is an important physical process in this context (see Fig 1.6), as its existence requires neutrinos

to be majorana particles [42]. Another useful outcome of the discovery of this rare process would be that it has the potential to provide the absolute scale of neutrino mass based on its theoretical foundations. Experiments like CUORE located in Italy using cryogenic bolometer of TeO_2 (^{130}Te) and KamLAND-Zen using Xenon-LS (^{136}Xe) are examples of efforts currently underway to look for the above event. The current lower limit on NDBD is $\sim 10^{26}$ years.

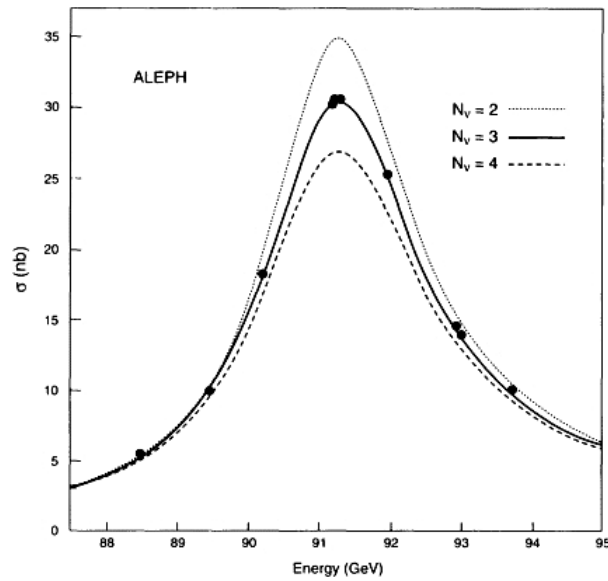


FIGURE 1.7: The invisible decay width of Z boson and fit performed for different neutrino numbers [43].

1.8 Anomalies pointing to more neutrinos

The standard model puts a limit on the number of neutrinos which can interact weakly with matter called the flavour eigenstates of neutrinos. There is strong evidence for existence of exactly 3 flavours of neutrinos based on the invisible decay width of Z boson as measured at the LEP collider at CERN [44]. As shown

in the Fig 1.7 a fit to the experimental data from multiple experiments has been done assuming 2 ν , 3 ν and 4 ν cases and the 3 ν case has the best fit. But, towards the later part of 20th century there were some hints that more neutrinos may exist although not belonging to standard model.

1.8.1 Short baseline oscillations : LSND Anomaly

There have been some new developments in the neutrino oscillation experiments which hint at the existence of more than 3 neutrino. One such instance is that of an accelerator neutrino oscillation experiment called the Liquid Scintillator neutrino detector (LSND) at the Meson physics facility– LAMPF at LANL, USA. LSND was looking for the appearance of $\bar{\nu}_\mu \rightarrow \bar{\nu}_e$ oscillation signature in a 167 tonne scintillator detector at distance of ~ 30 m [45]. Specifically, the neutrinos from muon decay-at-rest (DAR) and pions decay-in-flight (DIF) were observed. The novel detection technique in the setup was to use a diluted concentration of scintillant to allow for simultaneous detection through Cerenkov and scintillation photons. The experiment observed an excess of $\bar{\nu}_e$ events which was unexpected. Oscillations into and back from a heavier neutrino of the order of $\Delta m^2 \sim 1\text{eV}^2$ was considered a possible solution for this excess at such short distances. Since such a neutrino can't be a flavour eigenstate in SM, it is called a sterile neutrino. Interestingly, a similar experiment KARMEN conducted at the ISIS synchrotron source in Oxfordshire, UK didn't see excess in $\bar{\nu}_e$ events at 17 m distance and excluded much of the allowed parameter space of LSND anomaly [46]. MiniBooNE and its successor MicroBooNE experiments were proposed to fully address the LSND results. Recently, MiniBooNE also reported

excess events in their results which when combined with LSND is now at 6σ C.L [47].

The possibility of additional neutrinos which do not interact weakly but mix with the active flavours have been proposed in many beyond standard model (BSM) theories. The Neutrino Minimal Standard Model(nuMSM), Split See-Saw mechanism etc are few examples. Even in the existing standard model, the right handed neutrinos or left handed antineutrinos can't interact weakly and can be considered sterile neutrino candidates. All these theories have very massive sterile candidates but also have room for at least one light sterile neutrinos.

1.9 Reactor Anti-neutrino Anomaly

Using reactor neutrinos to study oscillation parameters started around the 1980s with experiments such as ILL, Bugey(France), Rovno and Moscow(Russia), Gosgen(Germany), Savannah river plant(USA) reporting the first measurements of $\bar{\nu}_e$ rates at different distances. The combined measured rates were slightly lower than the expectation by a factor 0.976 ± 0.024 and a recent re-evaluation of the expected $\bar{\nu}_e$ flux increased the average deficit to 0.943 ± 0.023 i.e. 5.7% at 98.6% C.L with standoff distances ≥ 15 m(See [48] and the reference therein). The phenomenon came to be referred to as the 'Reactor Anti-neutrino Anomaly' (RAA). The Reactor Anti-neutrino Anomaly (RAA) may very well be due to inadequate accounting of the reactor systematics. It can also be a hint towards new physics as it is obvious that this observation cannot be understood in the 3 neutrino framework. Including one additional neutrino called 3+1 neutrino framework is considered a viable option. But this 4th neutrino has to be sterile i.e. it should

have no standard model interaction and satisfy the requirements for short distance mixing.

1.9.1 Search for sterile neutrinos

To test the sterile neutrino hypothesis as an explanation for RAA, experiments are needed with baseline of ~ 10 m with preference for < 10 m standoff. Preparedness for background removal or rejection at these close distances is a must. Also, better energy resolution is required for improved sensitivity. In this context, few of the experiments are worthwhile for discussion.

One of the early experiments is the ‘Neutrino Experiment for Oscillation at Short baseline’ (NEOS) at ~ 25 m distance from 2.8 GW_{th} LEU core at Hanbit Nuclear Power Complex in Yeonggwang, South Korea. It used a 1 m^3 cylindrical core volume of LS with homogeneous Gd doping (0.5%) and placed 10 m (20 m.w.e) underground. The S:B ratio reported is 22 and the uncertainty in the energy scale is only 0.5%. The event detection was based on recoil pulse shape discrimination (PSD) technique. NEOS compared its prompt spectra with unfolded spectrum of Daya Bay (longer baseline) and also the spectrum predicted by Huber-Mueller-Vogel model. The comparison with Daya Bay data showed no signature of oscillation excluding almost of all of the sterile oscillation parameter space and the RAA best fit point. [49]

Neutrino-4 experiment in Russia (SM-3 reactor - 3.1 GW_{th} HEU) and STEREO experiment in France (ILL research reactor - 58 MW_{th} HEU) used similar detector as NEOS but increased volume $\sim 1.8 \text{ m}^3$ with Gd-doping. The important

difference being 2D segmentation in detector design. Neutrino-4 had movable platform giving baseline range from 6–12 m, while STEREO is stationary at 10 m. Both experiments excluded the major sterile parameter space, with Neutrino-4 reporting oscillations with large mixing angle and mass splitting $\sim 7.3\text{eV}^2$ [50]. The Precision Oscillation and Spectrum Experiment (PROSPECT) in operation at HFIR research reactor at ORNL, Oak Ridge, USA is perhaps the best equipped to address the short baseline oscillations. The PROSPECT detector is a 4 tonne by weight 3D segmented LS detector doped with ${}^6\text{Li}$ and boasts an impressive 4.5% energy resolution at 1 MeV. The detector is at 7.9 m from the 85 MW_{th} ${}^{235}\text{U}$ highly compact core. This allows PROSPECT to provide first model independent reactor neutrino flux measurement. The 2D segmentation leads to 154 individual LS bar like geometry each $117.6 \times 14.5 \times 14.5\text{cm}^3$ in dimensions with 5-inch PMTs at both ends. The spatial coverage of the detector is expected to be sensitive to spectral distortions in oscillations. One of the challenges to the detection is the <1 m.w.e overburden leading to large backgrounds. The detector takes advantage of topology, recoil and capture PSD and therefore has excellent separation of e^-/γ -like events against the recoil delayed events and an S:B better than 1:1. Results from about 96 days of data disfavor the RAA best fit point with 2.2σ C.L. [51].

All the experiments described till now had detection medium of LS. But there are detectors using plastic scintillators (PS) such as the DANSS (Russia) [52] and SoLiD (Belgium) [53] experiments at short baselines. The DANSS detector is located near the LEU core of Kalinin nuclear power plant with 3.1 GW_{th} output. It had provision for varying baseline through detector displacement between 10.7-12.7 m with 50 m.w.e overburden. The total volume was 1 m³ formed

with 2500 PS strips of dimensions $1 \times 4 \times 100\text{cm}^3$ with reflective polystyrene coat containing Gd oxide (0.35% by wt) to capture IBD neutrons. The strips are interleaved in a X-Y arrangement with both SiPMs and PMTs being used for readout. The result of measurement at different positions allowed for a ratio study excluding most of the sterile oscillation parameter space and the RAA best fit point.

The ‘Search for oscillation with ${}^6\text{Li}$ detector’ – SoLiD detector is operated at

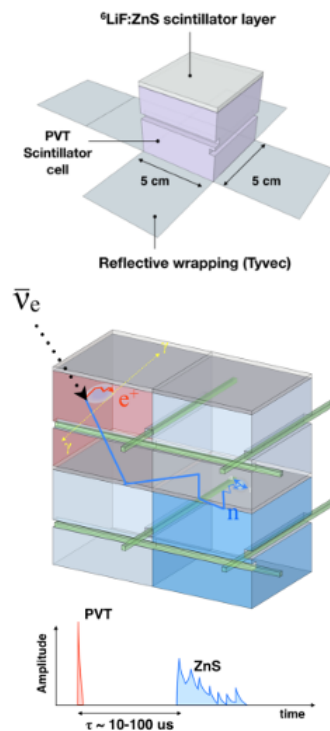


FIGURE 1.8: The basic element of SoLiD detector – ‘PVT cube’ with its components shown on top. An IBD event inside the detector is visualized in middle and time delay signature of prompt and delayed event shown at the bottom [53]

the BR2 HEU reactor (compact $80 \text{ MW}_{\text{th}}$ output) in Belgium with one of the closest and variable baseline between 6–9 m and under $\sim 10 \text{ m.w.e}$ overburden.

The novel 3D segmented detector aims at precise localisation of IBD events and efficient PSD. The target volume is made up of polyvinyl toluene (PVT) cubes of 5 cm each and wrapped with Tyvek wrapping for optical isolation. 10 layers of 16×16 such cubes form the phase I. There are grooves in each cube to carry wavelength shifting (WLS) fibers in orthogonal direction which guide scintillation signal to SiPM readouts. It employs a shielding of water filled PE tanks on sides and top. The annihilation γ -rays can be tagged in two adjacent cubes as prompt event. The detector technology employed was tested using a prototype module weighing 288 kg for both reactor ON and OFF duration. The IBD neutron gets thermalized inside a cube and then captured on the ${}^6\text{Li}$ present in the $250\mu\text{m}$ thick neutron sensitive layer of ${}^6\text{LiF} : \text{ZnS}(\text{Ag})$ on the two faces of the cube. The characteristic time profile and signature due to events in PVT and those in ZnS allow for good background discrimination. The efficiency of SoLid for IBD detection is estimated at 30% with S:B of 1:3. The phase I with a sensitive mass of 1.6 t and started operation in early 2018.

1.9.2 Spectral distortion at 5 MeV : The ‘Bump’

The discussion till now touched upon a number of anomalies which were basically deficits found in neutrino flux measurements when compared to a model/theory prediction for their production and propagation. However, recent results from many of the experiments probing the RAA have come across a new anomaly, which is not a deficit but rather an excess of events in the measured reactor neutrino spectra in the energy region 4-6 MeV. The ratio of prediction from the popular ‘Huber-Meuller-Vogel’ model of reactor neutrino flux to that observed

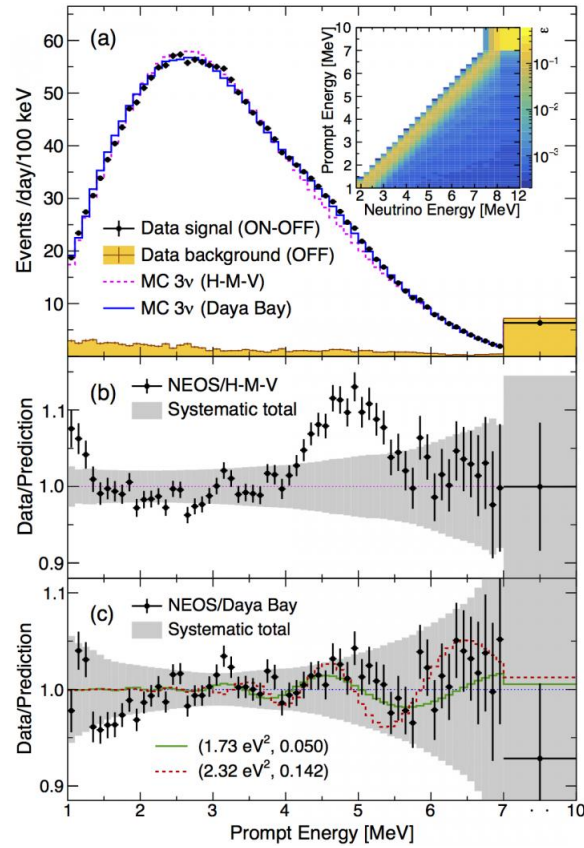


FIGURE 1.9: NEOS and Daya Bay experimental results compared with ‘H-M-V’ model [54].

at the experiments, has a bumpy feature from 4 to 6 MeV which peaks at 5 MeV, referred to as the ‘5 MeV bump’ [54]. This has triggered searches for potential origins of the bump with some researchers re-assessing individual contributions due to different isotopes (especially whether ^{238}U hard neutron spectrum is responsible), some revisiting the beta decay spectra measurements of ILL, while others treating it as possible manifestation of BSM physics.

1.10 Neutrinos as messenger particles

In addition to being portals to physics beyond standard model, neutrinos can also be ideal as messenger particles. Towards the last quarter of the 20th century, physicists started exploring the possibilities of applying the understanding of neutrinos in probing a variety of other phenomenon. The long mean free paths of neutrinos coupled with the fact that most fundamental and interesting physical processes in nature produce them, makes them ideal tool for such studies. A prevalent practice is to use neutrinos to probe their sources based on the intensity and spectrum of neutrinos being emitted from them.

As we have already seen in our discussion on the sources of neutrinos, geoneutrinos can help map the geological abundance and density profile of their radioactive sources, mostly the ^{238}U , ^{235}U , ^{232}Th and ^{40}K nuclei. On the astrophysical scale, neutrinos streaming down on earth from violent events like supernova, jets from active galactic nuclei carry signature of their internal dynamics. Due to the light mass and neutral nature of neutrinos, galactic, interstellar and even earth's electromagnetic fields cannot disturb their trajectory.

1.10.1 Multi-messenger astronomy : IceCube experiment

In the context of ultra high energy cosmic neutrinos, the IceCube experiment is worthwhile to be discussed simply because of its novel detection setup, scale of operation and challenging location. As the name suggests, IceCube is a cube of ice, but the volume of this cube is 1 km^3 . The only place such a huge volume of ice can be found is at the South Pole. IceCube is a km^3 volume of ice

between depths of 1450 m to 2450 m located near the Amundsen-Scott South Pole station. It is a detector primarily designed for detection of ultra high energy cosmic neutrinos produced in phenomena like GRBs, AGN jets, WIMP annihilation neutrinos from Sun, Supernova and even sufficiently energetic atmospheric neutrinos [18]. The detection mechanism is dependent on the Cerenkov photon detection as high energy products of neutrino interactions travel faster than light in ice. The timing and intensity of light signals are important variables. The primary detection element is a spherical optical sensor called Digital Optical Module (DOM) equipped with a PMT and a single-board data acquisition computer. In the very first installation phase in 2005, 60 such DOMs were strung together at equidistant heights as part of a single string and lowered at the designated depth through a hole melted in ice using hot water drill. By 2010, a total of 86 such strings had been lowered to the required depths and the construction was completed.

Figure 1.10 shows the full schematic of the IceCube detector with the different parts of the array. There are three major sections of IceCube setup - 1) A surface level Cerenkov detector array with two detectors approximately above each IceCube string called the 'IceTop array'. This serves as a veto and also to study the cosmic ray shower 2) The main 'In-Ice array' itself described earlier 3) A relatively new extension called the 'Deep Core' has extra density of instrumentation deployed from the central region of IceCube and to the bottom where the ice is the clearest. A Precision IceCube Next Generation Upgrade or PINGU detector which is another in-fill array like DeepCore is in pipeline for further bringing down the neutrino detection energy threshold to be sensitive to the SM neutrino oscillation and mass ordering.

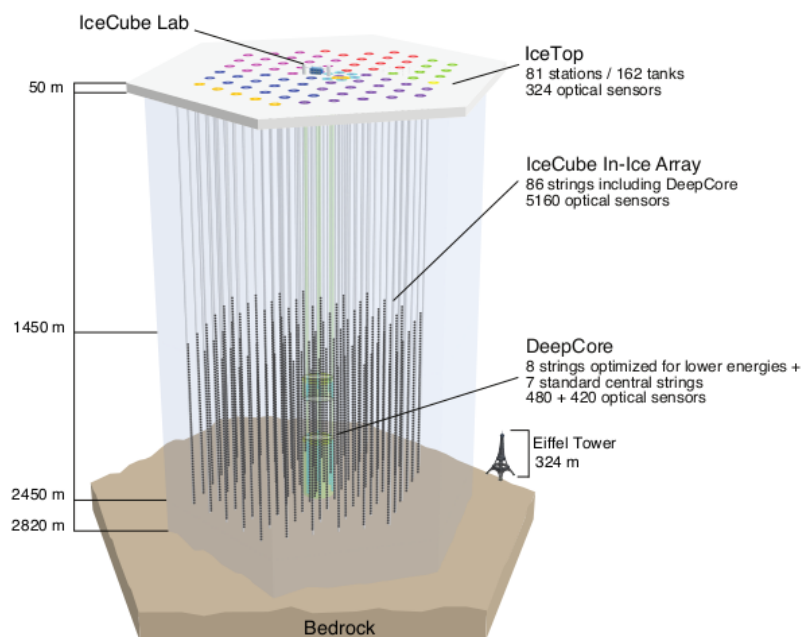


FIGURE 1.10: The schematic of IceCube Neutrino Observatory [18]

The Cerenkov detection help find the direction of the point sources of high energy neutrinos. The range of energies to which IceCube is sensitive starts from few 100 GeVs to few 1000 EeVs. Muon neutrino events are more desirable as they leave clean long tracks, while electron and tau neutrino events produce confined showers. Due to heavy flux of atmospheric neutrinos the IceCube depends more on events coming from Northern hemisphere. The Deep Core extension reduces the energy thresholds for neutrino detection below 100 GeV with most sensitivity to ~ 25 GeV neutrinos. Interestingly IceCube can also comment on the neutrino mass hierarchy due to possibility of observing a characteristic modification of oscillation pattern at ~ 15 GeV. Two PeV scale neutrino events named ‘Bert’, ‘Ernie’ in 2013 and an even higher energy event in 2017 called ‘Big Bird’ are amongst the highest energy particles detected in history.

1.11 Reactor monitoring

Application of neutrinos as messenger particles is also useful to non-intrusively probe the reactor core for changes in power output and evolution of the isotopic content of the fuel [55]. Traditional approaches to perform such measurements either involved instruments which are part of the reactor system loop or shutting down the reactor and accessing the core fuel assembly. The high flux $\sim 10^{21}$ of $\bar{\nu}_e$ s from a $\sim 1\text{GW}_e$ power output reactor allows for moderate scale ~ 1 tonne weight detectors to record sufficient statistics when placed at few meter distance. The dominant fissioning isotopes are ^{235}U , ^{238}U , ^{239}Pu and ^{241}Pu contributing 99.9% of the total thermal power.

$$N_{\bar{\nu}_e} = \gamma \cdot (1 + k) \cdot P_{th} \quad (1.14)$$

with γ being constant specific to the detector and geometry, P_{th} is the thermal power and k is the factor sensitive to the fuel's isotopic evolution. Normally, the fuel assembly starts off with having highest fraction of fissions due to nuclei of ^{235}U , but as the fuel 'burn-up' occurs, contribution from other isotopes especially from the increasing ^{239}Pu concentration reduces the neutrino rates as the decay chain of Pu produces less neutrinos. The detection medium usually comprises of a proton rich volume like water or scintillator where the $\bar{\nu}_e$ can undergo IBD reaction. Using sufficiently shielded detector assembly, these IBD events can be detected even with small S:B (close to 0.1) [56, 57].

This method is particularly of interest to the International Atomic Energy Agency (IAEA) which wants to utilize this technique as means to realize its reactor safeguards regime to ensure nuclear non-proliferation.

1.11.1 Worldwide efforts

The earliest research into the antineutrino based monitoring of reactor dates back to the 1970s, when the Kurchatov Institute in Russia conducted studies of reactor antineutrino spectra due to the different isotopes present in the fuel. They showed that the number of $\bar{\nu}_e$ /fission due to ^{239}Pu is less than those due to ^{235}U [55]. Subsequently, many types of such detectors were developed and in period from 1983-1994 feasibility studies for such a monitoring was performed at the Rovno NPS in USSR and later at Bugey NPP in France.

From early 2000 onward, many laboratories in Russia, USA, Germany and France started developing such detectors at their nuclear power/research facilities. Among these, SONGS1 experiment using LS based monitoring detector is probably one of the first moderate scale detectors. The SONGS experiment is named after the San Onofre Nuclear Generating Station. It was jointly conducted by the Sandia and Lawrence Livermore National Laboratories in California, USA in the tendon gallery of its PWR Unit-2, ~ 25 m from the core. The usual IBD based detection with prompt and delay coincidence is used for measuring $\bar{\nu}_e$ rates and spectrum for monitoring. The focus of the experiment was to develop a detector which is simple in construction as well operation and maintenance in keeping with the IAEA safeguards requirement. It was a 0.64 ton Gd-doped (0.1%) liquid scintillator filled in 4 stainless steel cells each of dimensions $\sim 0.4 \times 0.4 \times 1\text{m}^3$ and internally wrapped with reflective sheets and read out with two PMTs each. The overburden at the location was ~ 25 m.w.e, with six sides of the detector shielded with passive water or polyethylene shielding and 2 cm thick active muon veto scintillators shielded all sides except the bottom. Discrete

modules like ADCs, CFDs, Logic and TAC modules comprise the DAQ. ^{208}Tl Compton edge and continuum is the major source to derive energy calibration and especially useful for run-time drifts of energy scale and for relative calibration of PMTs. The estimates of detection efficiency from detector simulations comes at about 11% which is small but due to the high power output the expected rates are still ~ 400 events/day. Statistical separation of true correlated pairs from random coincidences done using two exponential fit and subtracting the reactor OFF data from ON. Inspection of prompt event energies in the two conditions and comparison of ON spectra with simulation also gives confirmation of the $\bar{\nu}_e$ detection [58]. The resulting antineutrino detection rate of 459 ± 16 /day is close to the expectation and demonstrated the feasibility of performing reactor neutrino detection with modest cubic meter scale detector. It was able to report a refueling shutdown with 99% C.L. within 5 hours and a net deficit ($\sim 50\%$) of antineutrinos due to ^{239}Pu build-up. The ruggedness of the setup and ability for standalone unmanned operation for longer durations make it an ideal template for similar detectors.

A similar detector, called NUCIFER, but with a bulk LS volume of ~ 850 L, was demonstrated to observe reactor neutrinos at the Osiris ($70 \text{ MW}_{\text{th}}$) research reactor in Saclay, France [60]. It was positioned at a very short baseline of ~ 7 m from core. Being inside the reactor hall environment, this detector required heavy shielding of 10 cm Pb and 14 cm borated polyethylene along with the usual active muon veto shielding. The NUCIFER LS tank and fully shielded setup are as shown in Fig 1.11. Using reactor simulations and comparison to the measured change in $\bar{\nu}_e$ rates the usefulness of these detectors for Plutonium monitoring was shown. Although, the detector was at ideal distance for short baseline oscillation

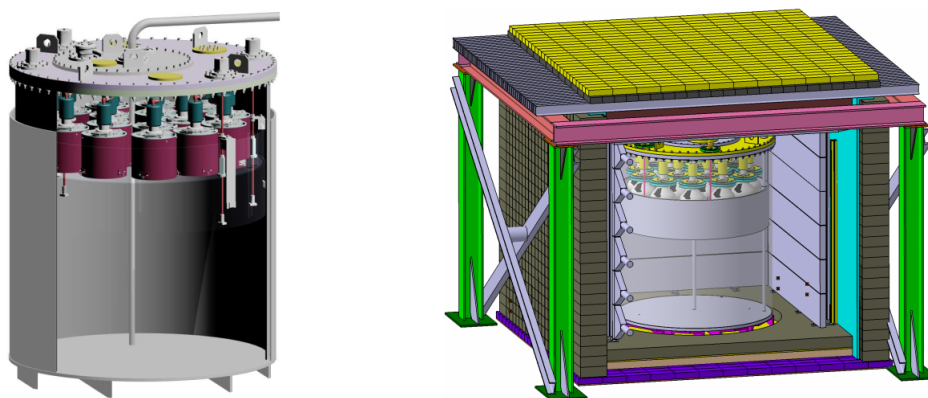


FIGURE 1.11: **Left:** The main LS tank of NUCIFER and **Right:** Final shielded setup of NUCIFER detector [59]

detection the overwhelming background didn't permit conclusive results. There are efforts in progress at bigger scales also, for R&D on a multi-purpose neutrino detection platform. AIT (Advanced Instrumentation Testbed)-WATCHMAN (WATER CHerenkov Monitor for AntiNeutrinos) is such a collaborative effort by USA and UK. The AIT-WATCHMAN facility will study neutrinos emitted by reactors, the Earth, the Sun, and other stellar sources covering both nuclear security and fundamental science applications [61]. The first stage of the AIT-WATCHMAN project is detection of reactor antineutrinos using a large water-based detector particularly at a significant distance from a nuclear reactor complex. The WATCHMAN detector will consist of approximately 5kT of highly purified water with trace amounts of gadolinium. Its relatively low cost and ease of scaling makes it a significant step towards building large detectors with sensitivity even at long baseline from nuclear reactors. WATCHMAN will also act as a high-sensitivity astrophysics detector built to detect neutrino emission from nearby supernovae neutrino events and analysis of these bursts to understand stel-

lar growth and collapse, element formation beyond helium and other unsolved problems in neutrino physics. The detector will operate 1.1 kilometers underground at the site of the Boulby Underground Laboratory, inside Boulby Mine in U.K. The mine is located on the north-eastern coast of England, 25 kilometers away from the Hartlepool nuclear power station. The Hartlepool station has two cores with $\sim 1.5 \text{ GW}_{\text{th}}$ thermal power output each, helpful to WATCHMAN for the exploration and development of antineutrino detection capabilities. The naturally occurring cosmic ray particles are reduced in rate by several orders of magnitude at the depth of 1.1 km, removing most of the cosmic background.

Liquid scintillators can be inconvenient to handle and even a fire hazard when operated close to the reactor core and the facilities might not permit such an operation inside the hall. Also, they can act like a toxic solvent for the container material. Plastic scintillators (PS) don't have such problems. Keeping this in view a more desirable detection material is PS volume which can even be in segmented form. A quintessential example of such a detector is the 1 ton by weight Plastic AntiNeutrino Detector Array (PANDA) developed by the Kitasato University and University of Tokyo collaborators in Japan [62]. It is planned for operation at the Ohi reactor. The experiment had gotten delayed due to the Fukushima-Daichi reactor accident leading to shutdown of power reactors across Japan. As the reactors are slowly resuming operation the experiment is again gaining momentum. The upside of going from LS to PS, in experiments like PANDA, apart from the ones pointed out earlier are better timing and event topology information for highly segmented volume which is usually the case. However, poor energy resolution and unavailability of uniform doping are two of the major drawbacks. The PANDA detector uses Gd-foil wrappings for neutron

capture. The location is expected to be ~ 30 m from core and simulated efficiency of about 11% is seen. A difference in the reactor ON and OFF period's antineutrino event rate with a 36 bar prototype – PANDA36 has been shown to be 21.8 ± 11.4 events/day while the predicted difference is 17.3 ± 6.2 events/day [63].

1.12 Indian Scintillator Matrix for Reactor AntiNeutrinos (ISMРАН)

A 1 ton by weight plastic scintillator based detector - 'ISMРАН' is being constructed at the Bhabha Atomic Research Centre (BARC), Trombay, as India's effort in the direction of monitoring reactor core and looking for sterile neutrino oscillations at short baseline. As an above ground setup, it is amongst the few such experiments, PANDA being another example, which conform more with the IAEA's guidelines for such detectors. A proof of principle experiment will be conducted at the Dhruva research reactor facility, BARC, where the above detector is planned to be positioned at a distance of 13 m from core center inside the reactor hall. The core detector of ISMРАН will be an array of 100 PS bars each of $100 \text{ cm} \times 10 \text{ cm} \times 10 \text{ cm}$ dimension and wrapped with foils having Gd_2O_3 coat (areal density 4.8 mg/cm^2). Each PS bar has two 3" PMTs coupled directly at both of its ends. As shown in schematic Fig 1.12 The 100 PS bars (black) will be arranged in a 10×10 array forming a 1 m^3 volume and housed inside a mobile trolley structure with provision for mounting a hermetic shielding of 10 cm Pb inside (pink) and 10 cm borated polyethylene (BP) (gray) outside. Muon veto scintillators (red) of 3 cm thickness will also be used to veto cosmic muons.

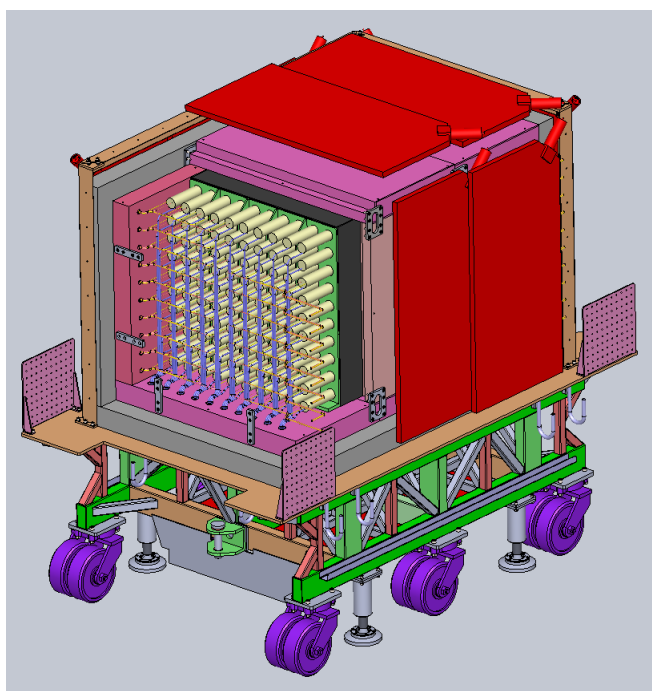


FIGURE 1.12: Schematic of ISMRAN setup

The trigger for IBD event inside ISMRAN will depend solely on the detection of prompt γ -rays due to positron annihilation and cascade γ -rays from delayed neutron capture preferably on Gd present in the foils. Once the event has been identified, summing up the positron event energy will give the energy of the $\bar{\nu}_e$ as they are related ($E_{\bar{\nu}_e} = E_{\text{prompt}} + 0.784 \text{ MeV}$). Obtaining a sum energy of $\sim 8 \text{ MeV}$ due to neutron capture provides a strong confirmation, without ambiguities due to cosmic or reactor specific backgrounds. A waveform digitizer based VME DAQ will acquire the signal from 200 channels. The full shielding along with complete DAQ electronics have already been tested using a 16% by volume prototype setup 'mini-ISMARAN' consisting of 16 PS bars in a 4×4 matrix at the reactor site.

1.13 Summary

Since their inception, neutrinos have been challenging the established physics by virtue of their nature and interactions. The most successful theory in physics - the Standard model of particles also struggles to accommodate the physical properties that neutrinos are proven to have. Much of the latter part of 20th century and even the early 21st century physics is driven by studies of neutrino properties and understanding their interactions. A brief account of the journey from the very first postulate to the theoretical and experimental studies on neutrino oscillation, masses have been presented.

The application of neutrinos as a monitoring tool, led to the idea of reactor core monitoring. The rates and spectrum of reactor neutrino play a central role in such applications. Although being very challenging, the feasibility of such an exercise has been demonstrated, but requiring some overburden to shield cosmic events. Parallel to this, a new direction to neutrino physics came with the reported anomalies in their flux from different sources including nuclear reactors (RAA). This has opened up the possibility for existence of a fourth neutrino.

This thesis work addresses the development of the reactor neutrino experiment - ISMRAN proposed at BARC, India. The different activities such as characterization and studies of the detector elements, setting up of a prototype detector- mini-ISMRAN, monte-carlo simulations, measurements of backgrounds and mini-ISMRAN data analysis are part of the thesis.

ORGANIZATION OF THESIS

Chapter 2: Indian Scintillator Matrix for Reactor AntiNeutrinos This chapter describes the ISMRAN detector and its prototype in depth followed by characterization studies with plastic scintillators.

Chapter 3: Detector Simulations This chapter deals with simulation studies carried out for the ISMRAN and miniISMRAN detector geometries for both the pure IBD events and cosmic muon and neutron events.

Chapter 4: Machine learning technique to improve the ISMRAN detection efficiency. This chapter deals with application of machine learning algorithm : multi-layer perceptron to improve upon prompt event selection and consequently the detection efficiency.

Chapter 5: Analysis of mini-ISMRAN reactor data This chapter presents the cut based analysis and preliminary estimates of $\bar{\nu}_e$ -like events from the long run data from mini-ISMRAN at Dhruva reactor site.

Chapter 6: Conclusions The work done till now for the ISMRAN experiment is summarized and the thesis is concluded in this chapter.

Chapter 7: Outlook Finally an outlook for the ISMRAN experiment and future activities planned are presented.

Chapter 2

Indian Scintillator Matrix for Reactor AntiNeutrinos

2.1 Reactor safeguards and anti-neutrino monitors

The IAEA conference of 2008, organized in Vienna to discuss nuclear non-proliferation laid down a roadmap for ensuring adherence to IAEA safeguards regime [64]. The use of antineutrino flux monitors for non-intrusive monitoring of the reactor cores formed an important part of the conference agenda. The feasibility aspect of reactor monitoring using such monitors has already been demonstrated by experiments, few of which have been discussed (see section 1.11.1). The future expectations, chalked out by the IAEA, for such detectors

include 1) the use of non-flammable materials, 2) reduced shielding requirement for less tonnage and 3) smaller footprint. The short term and medium term goals envisaged for such detectors also stresses that such detectors be above-ground and low costing. Also, measurements at different variety of reactor cores is advised, to establish the versatility of such a detector. The Indian Scintillator Matrix for Reactor AntiNeutrinos – ISMRAN a plastic scintillator (PS) based detector is proposed with the above guidelines in view for detection of electron antineutrino ($\bar{\nu}_e$) emitted by reactor cores [65]. The measurement of $\bar{\nu}_e$ rates closer to the neutrino source is also useful to detect sterile oscillation signature at short baselines $O(10\text{ m})$. For this purpose the rate and spectrum of antineutrinos being emitted by the reactor needs to be measured. The ISMRAN experiment, aims to perform such measurements at the Indian reactor facilities. It is currently hosted at the Dhruva research reactor facility at the Bhabha Atomic Research Centre, Mumbai, India, for a proof-of-principle study. In the following section we will discuss the Dhruva reactor facility. The subsequent sections will discuss the ISMRAN detector design and its prototype.

2.2 The Dhruva reactor

The Dhruva reactor was conceptualised in the 1970s to provide high neutron flux for radioisotope production and to facilitate research in basic sciences and engineering [66]. The reactor became critical on 8th August 1985 and started operation at full power on 17th January 1988. It has a host of features which are suitable for reactor neutrino related measurements, especially monitoring and sterile oscillation searches. Most of the reactor neutrino experiments conducted



FIGURE 2.1: **Left:** Dhruva reactor building at BARC from outside. **Right:** Inside the Dhruva reactor hall.

till now have been hosted at a reactor whose core has some amount of enrichment, either low or high, many of these being power reactors. Also due to this enrichment the moderator has been light water. Dhruva reactor differs on many of these accounts from the existing power and research reactors used for neutrino physics.

Core fuel : Dhruva uses metallic natural uranium (^{238}U : 99.3% & ^{235}U : 0.7%) as fuel and heavy water as moderator, coolant and reflector. This makes it unique, as it can provide a first measurement of neutrino spectrum and evolution for natural uranium fuel. Also, it can probe the spectral distortion in such a fuel composition.

High power research reactor: Compared to many of the existing research reactors, Dhruva has a higher thermal power output : $100 \text{ MW}_{\text{th}}$. More power translates to higher rate of neutrinos.

Baseline range : The site selected for placing ISMRAN inside Dhruva reactor hall has the leverage to go closer to the core, with least standoff at slightly more than 7 m (where the biological shield ends) and farther upto 14 m. Although, currently the measurement is being carried out at 13 m distance, the setup has

possibility and readiness for moving near or far from the core between these limits.

There are some drawbacks too, that need to be pointed out. Dhruva has a non-compact cylindrical core (3.72 m diameter and 3.87 m height) which leads to slightly different baselines for antineutrinos coming from different fuel elements. Also, as it is designed for radioisotope production it has a high neutron flux $\sim 1.8 \times 10^{14} \text{ n cm}^{-2}\text{sec}^{-1}$ at the core which gives about $10^5 \text{ n cm}^{-2}\text{sec}^{-1}$ flux at the beam ports. Due to presence of multiple such ports for neutron related experiments, the background inside the hall and closer to the setup is quite high. The diametrical spread of the fuel elements and the multiple beam ports can be seen in Fig 2.2.

These drawbacks can be overcome by taking into account the effect of finite

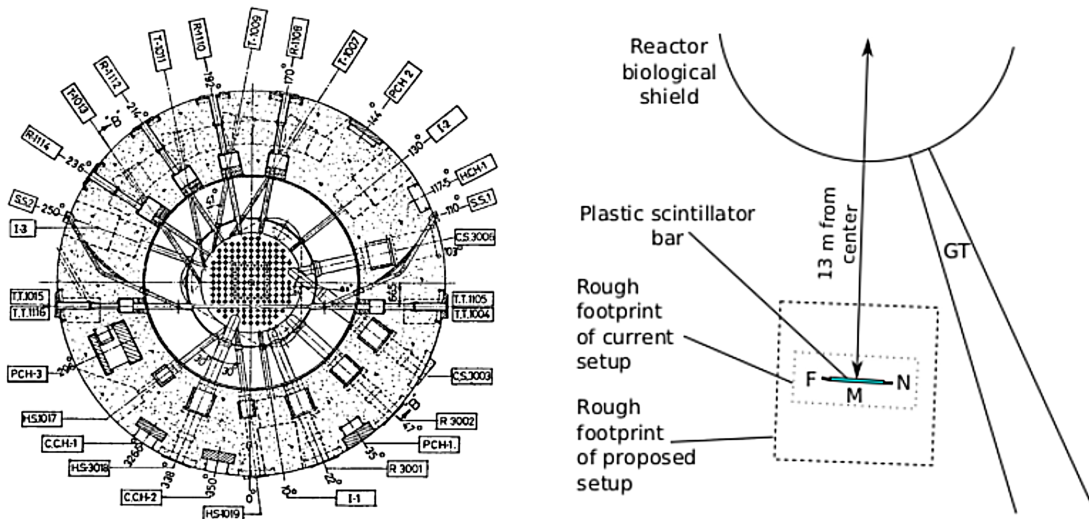


FIGURE 2.2: **Left:** Cross-sectional view of Dhruva reactor core [66]. **Right:** ISMRAN footprint location and orientation w.r.t core center in reactor hall.

core size while generating the source $\bar{\nu}_e$ spectrum in simulations and ensuring that the extra sources of backgrounds are properly shielded during operation.

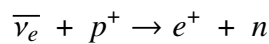
TABLE 2.1: Specifications of the Dhruva reactor [67].

Reactor Type	Vertical Tank Type / Thermal Reactor
Reactor Power	100 MW _{th} (Maximum)
Fuel Material	Natural Uranium Metal
Fuel Element	Cluster of fuel rods
Fuel Cladding	Aluminium
Total weight of Fuel	6.35 T
Core Size	3.72m(D) x 3.87m(H)
Max Neutron Flux	$1.8 \times 10^{14} \text{ncm}^{-2}\text{s}^{-1}$
Moderator	Heavy water
Coolant	Heavy water
Shut off Rods	Cadmium
Uses	Basic research; isotope production; manpower training; neutron activation analysis; testing of neutron

The reactor operations division keeps record of the change in the power levels which comes useful for cross-checking observed rates in experiment and hence for accurate accounting and precision analysis. The table 2.1 summarizes the Dhruva reactor specifications.

2.3 $\bar{\nu}_e$ event detection and rates in ISMRAN

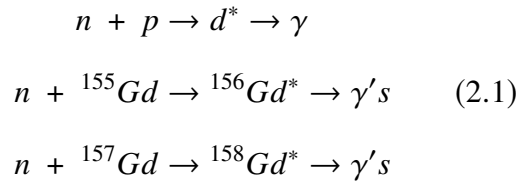
Since the Inverse Beta Decay (IBD) reaction offers a relatively high cross-section and convenient method for $\bar{\nu}_e$ detection, most experiments including ISMRAN use scintillators as the detection medium for detecting reactor $\bar{\nu}_e$. The IBD reaction in a scintillator volume takes place as:



Thus an emitted $\bar{\nu}_e$ from Dhruva core will interact with a quasi free proton inside

the ISMRAN volume and produce a positron and neutron. The products of the reaction being more massive, the reaction has a threshold of 1.806 MeV. The neutrino is assumed as massless due to the high kinetic energy.

The positron loses energy quickly via ionization of the scintillator medium and annihilates with an electron to produce two 511 keV γ -rays which themselves undergo multiple compton scatterings and lose energy in one or more bars. These energy losses produce scintillation photons inside the PS bar and all of this happens almost within a few nanoseconds (ns) of the IBD interaction and hence called a “prompt event”. The neutron produced in the IBD has energy ~ 10 keV and undergoes elastic collisions with the H and C nuclei to reach thermal energies. These thermalizing neutrons can get captured on the H nuclei in the bulk or Gd nuclei present in the wrapping as follows:



Thermal neutron capture on Gd nucleus is followed by emission of γ -ray cascades from its de-excitation. These γ -rays undergo compton scattering and deposit energy in large number of PS bars, which comprises the “delayed event”. The neutron thermalization and capture takes $O(10)$ to $O(100)$ of μs . The sum

TABLE 2.2: Energy released and cross-section for neutron capture in ISMRAN geometry

Reaction	Total energy of γ -rays (MeV)	$\sigma_{n\text{-capture}}$ (barns)
H-Capture	2.2	0.3
^{155}Gd capture	8.5	61000
^{157}Gd capture	7.9	254000

of these deposited energies in PS bars is expected to be around 8 MeV, for a fully contained event. Such pairs of prompt positron signals and delayed neutron capture signals form the $\bar{\nu}_e$ IBD event. The capture of neutron on H nucleus produces a mono-energetic γ -ray of energy 2.2 MeV. But due to its lower energy, this signal is easily swamped by the reactor background and hence not used for $\bar{\nu}_e$ detection in most near-field experiments.

The rate of $\bar{\nu}_e$ events recorded in a scintillator volume can be estimated for a detector like ISMRAN using the knowledge of detector geometry, IBD cross-section and emitted spectrum for different fissioning nuclei and the standoff distance. The nuclei ^{235}U , ^{239}Pu , ^{238}U and ^{241}Pu together contribute 99.9% of the total thermal power with major contribution of the emitted $\bar{\nu}_e$ coming from the fission of ^{235}U and ^{239}Pu isotopes. The rate of interaction of reactor $\bar{\nu}_e$ with energies $E_{\bar{\nu}_e}$ inside the scintillator volume depends on the $\bar{\nu}_e$ spectrum per fission $f(E_{\bar{\nu}_e})$, the number of free protons N_p , detector efficiency η , thermal power P_{th} of the reactor (MW), average energy per fission \bar{E}_f (MeV) released in the reactor core and the distance D (cm) between the detector and center of the core. Hence, the total interaction rate in the detector volume obtained by integrating over energies [56] is given as:

$$N_{\bar{\nu}_e} = \frac{N_p \cdot P_{th} \cdot \bar{\sigma}_{IBD} \cdot \eta}{4\pi D^2 \cdot \bar{E}_f \cdot 1.6 \cdot 10^{-19}}, \quad (2.2)$$

where, $\bar{\sigma}_{IBD} = \int \sigma(E_{\bar{\nu}_e}) f(E_{\bar{\nu}_e}) dN_{\bar{\nu}_e}(E_{\bar{\nu}_e})$ is the cross section of IBD averaged over

the $\bar{\nu}_e$ spectrum. The cross-section $\bar{\sigma}_f$ and energy released \bar{E}_f are usually expressed in terms of the corresponding quantities σ_i and E_i for the four dominant isotopes, i.e. ^{235}U , ^{239}Pu , ^{238}U and ^{241}Pu , along with α_i as the contribution of each isotope to the total number of fissions.

$$\bar{\sigma}_{\text{IBD}} = \sum \alpha_i \sigma_i \quad \bar{E}_f = \sum \alpha_i E_i \quad (2.3)$$

where $\sum \alpha_i = 1$. Thus both the thermal power P_{th} and the contribution from the isotopes to the cross-section ($\alpha_i \sigma_i$) are directly reflected in the $\bar{\nu}_e$ rate in the detector. For the ISMRAN setup which is at 13 m distance from a 100 MW_{th} Dhruva core the $\bar{\nu}_e$ event rate from calculation is ~60 per day. This value is calculated assuming a compact core and a 15 % detection efficiency and no sterile oscillation scenario. The $\bar{\nu}_e$ event rate scales with reactor power and hence power level monitoring can be achieved by establishing a relation of the observed rates with the reactor power values. Additionally, monitoring the fuel changes requires knowledge of expected $\bar{\nu}_e$ spectrum specific to Dhruva core. Both these steps need the simulation of Dhruva reactor core to obtain its $\bar{\nu}_e$ flux and a separate group of reactor physicists are working on it.

2.4 ISMRAN PS bar

The primary detection element of ISMRAN detector is the PS bar. The ISMRAN PS bar has a linear geometry with dimensions 100 cm × 10 cm × 10 cm. They are wrapped with aluminized mylar foils for reflecting the scintillation light inside. The outside of this mylar film is coated with neutron capture agent Gd₂O₃ (natural Gd) in the form of a paint whose areal density is 4.8mg/cm². A light tight vinyl wrapping covers the PS and the mylar from outside.

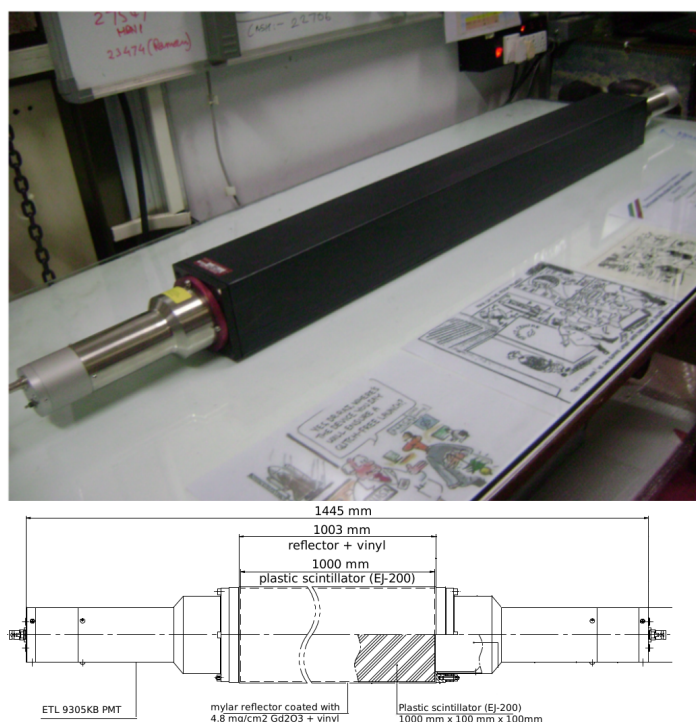


FIGURE 2.3: **Top:** ISMRAN PS bar in lab. **Bottom:** Drawing of the PS bar showing different parts and dimensions.

Figure 2.3 shows the ISMRAN PS bar in lab and with a detailed drawing showing different parts and their dimensions. Each of the PS detectors is of the commercially available EJ200 composition from ELJEN technology [68]. Long optical attenuation length and fast timing are two important properties which make it particularly useful for larger geometries like ISMRAN. The emitted scintillation photon spectrum of EJ200 is shown in figure 2.4. The emission spectrum peaks at around 430 nm which is in the blue light region, and slowly tapers off towards green light. The various properties of the scintillator composition are listed in table 2.3.

TABLE 2.3: Properties of EJ200 scintillator [68]

Properties	EJ200 specifications
Light Output (% Anthracene)	64
Scintillation Efficiency (photons/1 MeV e ⁻)	10,000
Wavelength of Maximum Emission (nm)	425
Light Attenuation Length (cm)	380
Rise Time (ns)	0.9
Decay Time (ns)	2.1
Pulse Width, FWHM (ns)	2.5
No. of H Atoms per cm ³ (x10 ²²)	5.17
No. of C Atoms per cm ³ (x10 ²²)	4.69
No. of Electrons per cm ³ (x10 ²³)	3.33
Density (g/cm ³)	1.023
Polymer Base	Polyvinyltoluene
Refractive Index	1.58
Light Output vs. Temperature	At 60°C, L.O. = 95% of that at 20°C No change from 20°C to -60°
Temperature Range	-20°C to 60°C

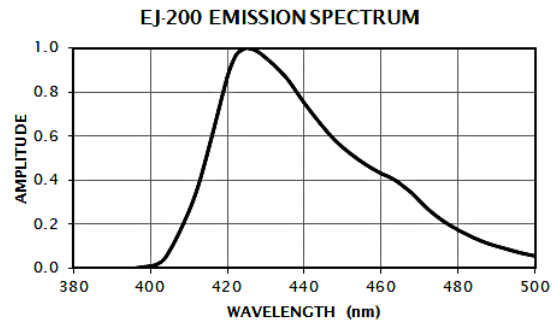


FIGURE 2.4: Emission spectrum or wavelengths of scintillation photons for EJ200 scintillator [68].

The scintillator output is recorded by PMTs directly attached at both ends of the PS bar. No light guide interface is used between the PMT and the PS bar. The PMT model is ETL9305KB 2.4 by Electron enterprises [69]. It has a 78mm (3-inch) diameter end-window PMT, with bialkali photocathode sensitive to blue-green spectral range. Ten high gain, high stability, SbCs dynodes of linear focused design are used for good linearity and timing in this model. This PMT is specifically designed for scintillation spectroscopy, as it has good resolution. The

spectral response of the 9305KB shows high sensitivity in the emission range of EJ200 which is ideal efficient PMT response. A 12 stage counterpart of this PMT– ETL9821B with almost similar performance but requiring higher bias voltage have been used only for the first set of 20 bars procured earlier.

TABLE 2.4: Properties of ETL 9305KB PMT [69]

Characteristics	typical values
photocathode: bialkali SbCs	
Quantum efficiency	30%
Luminous sensitivity	75 $\mu\text{A}/\text{lm}$
dark current at 20°C :	
dc at nominal A/lm	0.5 nA (up to 10 nA max.)
dark count rate	500 s^{-1}
pulse height resolution :	
single electron peak to valley (ratio)	2
^{137}Cs with 3" \times 3" NaI(Tl)	7.3%
timing :	
Single electron rise time	3 ns
single electron fwhm	4 ns
maximum ratings :	
anode current	100 μA (max)
cathode current	200 nA (max)
gain	3×10^6
sensitivity	200 A/lm (max)
operating temperature	-30° to 60°

2.5 ISMRAN detector

The full ISMRAN detector will have 100 of the above PS bars in a 10×10 – 2D array or matrix. The whole setup will form a 1 m^3 volume having 1 tonne weight. The completely assembled detector will be housed inside a shielding of 10 cm Lead (Pb) and 10 cm borated polyethylene (BP) having 30% boron. The Pb bricks will be 5 cm thick (~10 kg) with chevron inter-locking form and put together as a double layer to form 10 cm thick shield, followed by BP sheets of 50 cm \times 50 cm area and 5 cm thick (~60 Kg) with 4 sheets covering one side of the

detector. The total weight of the setup with the detectors, shielding and trolley structure is expected to be about 20 tonnes. Additional high density polyethylene structure is expected to be about 20 tonnes. Additional high density polyethylene

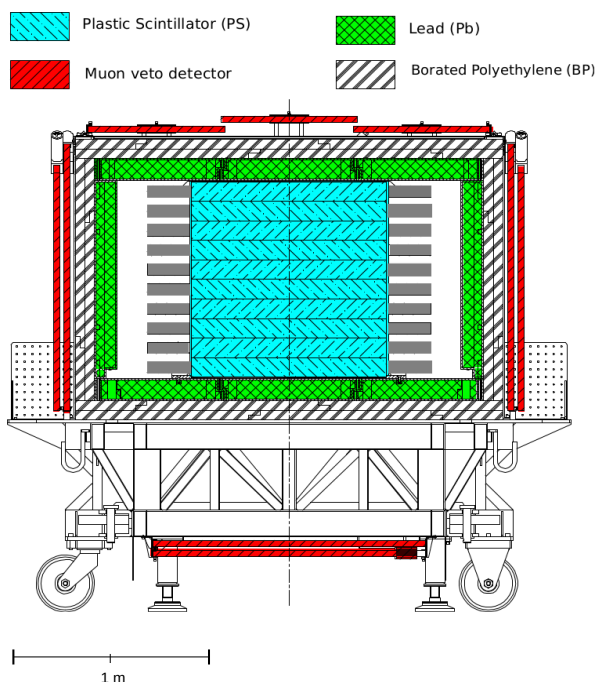


FIGURE 2.5: Proposed ISMRAN detector setup comprising of shielding trolley and 100 PS bars. The major components of the setup are listed in their respective colors at top.

or composite shielding of HDPE, BP and Pb may be incorporated but most likely independent of the setup. For vetoing the cosmic muons an active shield of muon veto scintillators will be covering all the sides of the detector assembly. See figure 2.5 for the schematic of the setup. A trolley structure which is a combination of stainless steel and mild steel components supports the shielding and the ISMRAN setup. Additional sheets of high density polyethylene (HDPE) may be used but not necessarily attached to the final setup. Four nylon caster

wheels will be used to move the setup while stainless steel pads with rubber grips will anchor it in position. The proposed ISMRAN detector has a host of qualities which make it suitable for near-field reactor monitoring as per IAEA guidelines:

- The use of PS instead of LS makes it non hazardous as PS is not easily flammable.
- The overall shielding weight is not so extraneous as to exceed permissible floor burden and make it hard to move.
- The full assembly has a footprint of only 3 m × 3 m and does not occupy much surface area inside the reactor hall.
- It will be positioned above ground, which is more convenient and straightforward compared to underground locations.
- Also in case of Dhruva, ISMRAN will be measuring $\bar{\nu}_e$ spectrum at a CANDU type reactor core which will be a novel monitoring exercise.

When operating multiple detector (PS bar) geometry like ISMRAN the individual detectors' response uniformity and health needs to be monitored throughout operation. This involves inserting radioactive sources for in-situ calibration inside the closed detector assembly.

The previous design didn't have this facility, so a modified design with provision for introducing sources inside the detector was finalised. To create additional space inside the ISMRAN matrix for calibration slots the array had to be reduced to 9×10 with the newly formed 10 cm space distributed in 5 vertical slot positions. The new design is shown in the figure 2.6. To actually insert the sources the top shielding has provisions for shielding plugs of Pb and BP which can be removed

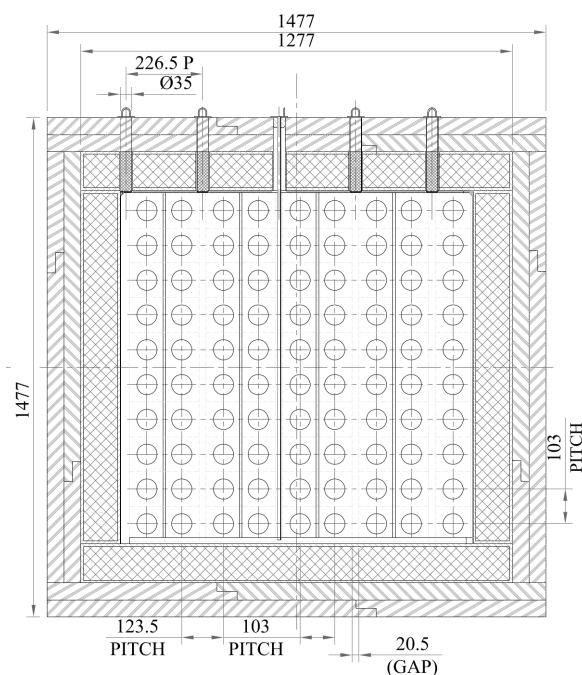


FIGURE 2.6: Cross-sectional view of modified ISMRAN assembly design with provision of in-situ calibration. The shielding plugs and slots are visible.

and reinserted in place. Possible widening of the trolley design in future might again bring back the possibility of having 10×10 array.

2.6 Pulse processing electronics and DAQ

The high background environment of reactor hall requires faster signal processing and event recording so as to avoid losing signal events. The constraints on the weight of the setup and mobility considerations also don't allow extra shielding to be introduced for reducing background. To have, a near deadtime-less acquisition, the ISMRAN DAQ uses the CAEN V1730 VME waveform digitizers as the primary pulse processing component. It is a 16 channel digitizer with

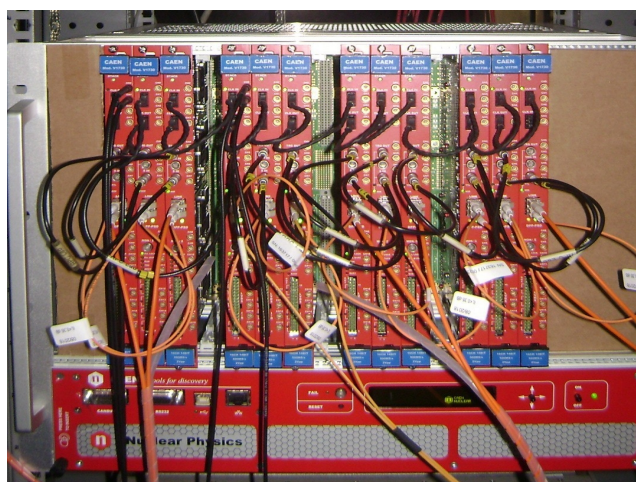


FIGURE 2.7: V1730 digitizer based system of 12 boards, synchronized and daisy-chained for data taking operation.

sampling capability of 500 Million Samples per second (MS/s) [70]. 13 such digitizers will be reading the output of 200 PMT channels of ISMRAN. Figure 2.7 shows, multiple digitizers being synchronized and daisy-chained during DAQ benchmarking for the full setup. The different data acquisition operations such as discrimination, extracting energy and timing information of the signal pulse, coincidence filtering etc. are performed on each channel by the on-board Altera Cyclone-IV family FPGAs. The digitizer output is fed to the DAQ PC using optical fiber cables which can transmit at 80 MB/s. The operations such as trigger generation, charge integration for energy information, constant fraction discrimination and timestamp extraction are performed by the Digital Pulse Processing (DPP) algorithm. For ISMRAN application both pulse height and pulse shape information can be used, but pulse shape discrimination (PSD) capability allows γ -neutron event discrimination, which is useful if neutron backgrounds is to be quantified with liquid scintillators and also as a preparedness for future

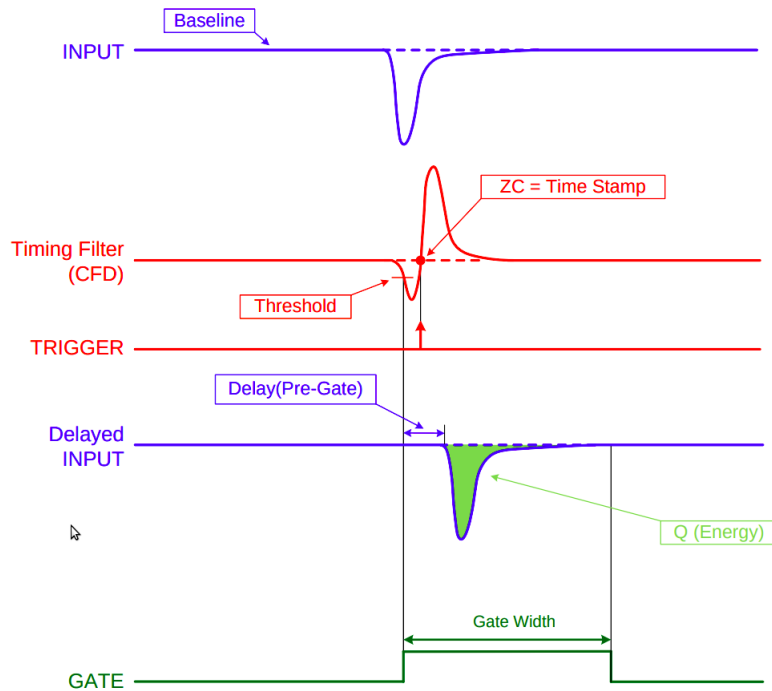


FIGURE 2.8: Typical pulse acquisition for waveform digitizers showing trigger and gating information [71].

switch to liquid scintillator based detector. All the operations desired from the digitizers, are decided by parameters such as integration gate, triggering thresholds, sample length etc. and are provided by the user to the FPGA firmware in a configuration file in each digitizer run. These are then applied on the acquired samples of pulse waveforms and accepted pulses are processed further. An important property of a sampled event is the ‘timestamp’. This is obtained after the sampled waveform is passed through constant fraction algorithm where the cross-over point is obtained through a linear interpolation of sampled points. The interpolated point is assigned a ‘fine timestamp’ while the sample nearest to this point gives the ‘coarse timestamp’. This interpolation allows going up to a precision of picoseconds between events in two different channels. See figure 2.8

for a typical pulse acquisition and figure 2.9 for the CFD interpolated timestamp derivation.

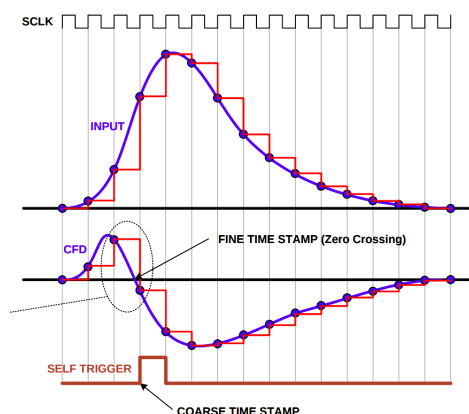


FIGURE 2.9: Timestamp derivation from cross-over in digitizer pulse processing algorithm [70]

For operating a multi-board system like ISMRAN, a crucial step is to synchronize the operation of all digitizers when recording data together, as the timestamps are required to be aligned for faithful reconstruction of events. Also, acquiring data from these digitizers together requires ‘daisy-chaining’ of their outputs which is basically a co-ordinated or sequenced read-out procedure for the combined hardware and software system. For ISMRAN data taking, each digitizer can trigger individually, but, their clock and start reference needs to be shared and the output optical read-outs need to be ‘daisy-chained’. In the case of CAEN V1730 digitizers, the boards acquire events independently through their channel auto-triggers (waveforms crossing the thresholds set). Two CAEN softwares, which helped establish synchronization are the ‘CAEN Upgrader’ and ‘CAEN SyncTest’. The following major steps are involved in synchronization:

- **Same clock propagated to all boards:** One digitizer board generates its internal clock and distributes it by the use of external clock output connectors to other boards in a master–slave fashion. This is called ‘Clock Synthesis and distribution’. In CAEN digitizers the clock management is provided by a PLL (Phase-locked Loop) and a Clock Distributor. The PLL can be set to receive a reference clock from either an internal oscillator or an external clock source through the clock input (CLK-IN) connector, using a mechanical switch. The role of the PLL is therefore to align the phase of a Voltage Controlled Crystal Oscillator (VCXO) of the digitizers to the reference one. The clock generated by the VCXO is passed to the Clock Distributor, which splits the clock signal in different branches sent to board subsystems. The remaining branch is connected to the clock output (CLK OUT) connector. The Clock Distributor can send a different sub multiple of the VCXO frequency to each branch. The Clock Distributor can also apply a delay to the CLK OUT connector. This is a key feature of the synchronization since it can compensate the effect of the clock shift due to the daisy chain between different boards. PLL is programmed to synthesize the right operation frequency.

- **Same time reference for all boards:** Input and output connectors are used to synchronize the start of the data taking and the time reference. The start logic signal can be propagated in daisy chain to all boards belonging to the acquisition system. This involves clock and output synchronization. In the multi-board acquisition system, the master board, will act as clock master (or simply ‘Master’) providing a reference clock to the other one,

that therefore will be a clock slave (hereafter 'Slave'). The CLK OUT of the Master is connected to the CLK IN of Slave through the A317 cable. As can be seen in figure 2.7, each the master board's clock is connected to the nearest slave using the this cable and each slave then receives as well as shares the same clock down the chain. Also, parallelly the TRGOUT to SIN connection ensures same reference time for triggering of each board. The 'daisy-chaining' of output that we discussed involves similar interconnection where Transmitter of master is connected to receiver of slave and likewise for all boards thereafter till a new block is started again. For the 12 digitizer system 4 blocks of 3 digitizers are daisy chained together and fed to the computer using optical controllers.

- **Trigger propagation and/or correlation:** Digitizers are able to receive external trigger signals and propagate them outside, for e.g. to propagate a global trigger signal in daisy chain. ISMRAN currently doesn't use external or global triggers but if they are introduced in future, trigger propagation will become crucial.
- **Readout synchronization and event alignment:** The mechanism that prevents an asynchronous data taking, which may happen when at least one of the boards enters in a busy condition. There are BUSY and VETO states included in the digitizer boards to ensure this behaviour.

To perform the actual procedure using CAENUpgrader and CAEN SyncTest utilities following sequence of actions were followed.

- Identifying/Setting-up the base address of each digitizer for programming

purposes.

- Programming the PLL (using a .rbf file) of master to use the 125 MHz VCXO frequency for its operation and to provide output clock of 62.5 MHz for slave. The slaves then share the same clock – 62.5 MHz, down the chain and implemented through similar PLL programming of slaves.
- Following this the synchronization is tested using the ‘SyncTest’ code, which routes the now programmed operation clock to TRGOUT (output trigger connector) for checking the synchronicity between the master and slave. This delay, if present, can be seen on the oscilloscope and its value can be obtained.
- If a small delay is present between the master and slave clocks, it can be again adjusted using PLL upgrade. The fine adjustment option in PLL upgrade allows changes down to few 100 ps level depending on the digitizer model. In our case a 2.5 ns delay was found and adjusted in PLL upgrade.
- After this adjustment, the synchronization was again checked on oscilloscope and the edges of the clock pulse were found to be aligned. The synchronization is thus complete.

To verify the effectiveness of synchronization, an exercise was performed simultaneously with the above procedure. Timestamps of each slave board in the chain are recorded at a time with the master using cosmic muon events passing through two PS bars, connected to two selected boards. A simple threshold energy cut of $E_{Th} > 15\text{MeV}$ ensured triggering on muon events as the PS bar is 10 cm wide (MIP energy loss is $\sim 20\text{ MeV}$). Keeping a coincidence requirement

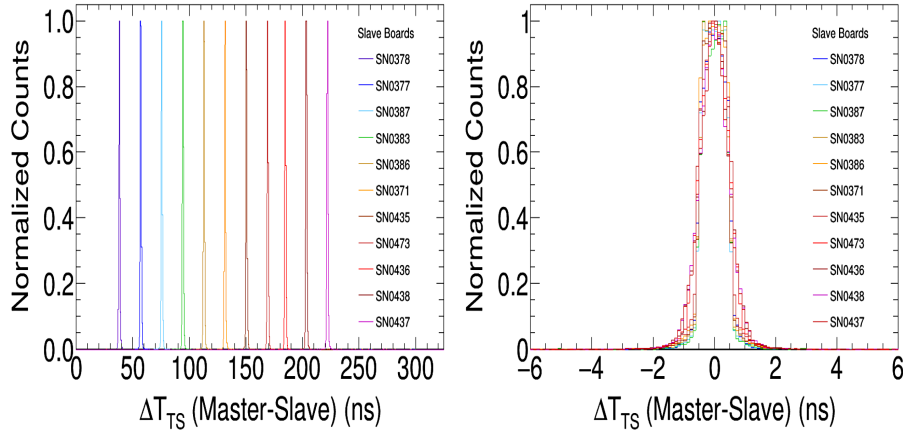


FIGURE 2.10: The timestamp difference ΔT_{TS} between master and slave digitizers for the muon events **Left:** Before synchronization and **Right:** After synchronization.

of few 100 ns, events were recorded and ΔT_{TS} between master and slave boards were plotted progressively for slaves by moving down the chain till the last board. The figure 2.10 shows this comparison for timestamps before and after synchronization procedure. The image on the left shows the shift in the ΔT_{TS} as we move away from the master with the first difference being the highest ~ 38 ns while a constant shift of ~ 19 ns is observed amongst the slaves in the chain. This was corrected with the synchronization procedure outlined before. After synchronization the muon events were again acquired and the right image in figure 2.10 shows the resulting ΔT_{TS} between master and all the slaves in the chain. It is evident that the shift in timestamps is now well within the resolution of the PS bar and digitizer system. This result ensures that the synchronization procedure is indeed working.

2.6.1 Acquisition software - digiTES

The data acquisition system in ISMRAN is more software or FPGA (firmware) driven than hardware modules due to absence of separate discriminators, ADCs, TDCs and logic builders. For the processing, receiving and writing of events communication between PC and digitizer is necessary. This is realized using an open source bare bone software available from CAEN website called the 'digiTES' [72] abbreviated form of 'digital acquisition of Time, Energy and Shape' which is a simplified interface between FPGA registers and the user. All the signal operations are programmed into the FPGA firmware through this software. The 'digiTES' forms the software arm of the 'Multiparametric DAQ', the hardware being the waveform digitizer. The FPGA then samples the raw pulse signals and processes it as per user settings of the different acquisition parameters. The digitizer output is also not the final processed version. But it contains information such as ADC charge information of the two PMT signals passing the discrimination criteria, digitizer channel numbers (continued over all boards), timestamp of PMT signals and epoch time of computer. Without any instructions given to it the digitizer would simply acquire raw samples of the pulse waveform and write list(.txt) files. It takes in a configuration (xxx.cfg) file which conveys the various parameter settings to the digitizer at the start of every run. These parameters both configure the digitizer firmware for the specific run, as well as, set the signal filtering criteria. The configuration settings are therefore divided into blocks such as – global run parameters (start/stop, write format and disk location etc.), triggering, discrimination and thresholds, pulse gating, charge sensitivity or gain, coincidence windows and so on. A number of

discriminator (CFD or LED). The FineTimeStamp is expressed in ps.

Energy: (16 bit); this is the pulse height in the DPP – PHA or the pulse charge in the DPP – PSD

PSD: (float in the range 0.0 – 1.0); this is a pulse shape discrimination factor. In pulse shape discrimination firmware, it is the ratio between the charge in the tail of the signal (slow component) and the total energy: $PSD = (Q_L - Q_S)/Q_L$. For other modes this field is normally meaningless (set to 0), but can be reformulated as some other variable to discriminate pulses.

Flags: (16 bits) these are various flags indicating pile-up, overflow, etc.

Waveform: (pointer to the waveform data structure); this field is NULL if the waveform readout is not enabled, otherwise it points to a memory buffer from where the waveform data can be retrieved.

This unique data format is then passed on to be stored in sufficiently large memory buffers called ‘QUEUES’ where each channel data is parallely held. In case correlation filters are to be applied, these are pulled out of queues and criteria are applied in the ‘SELECTION’ block. Then onwards the filtered events are passed on to ‘ANALYSIS’ where histograms and other statistical objects are built. The ‘PLOTS’ then plots it on to a plotting interface. Thus ‘digiTES’ sees through the overall operation of the DAQ and provides data in the user defined format.

2.7 Prototype detector – mini-ISMARAN

To understand the background levels inside the reactor hall and to test the feasibility of unmanned operation for long duration, a prototype setup mini-ISMARAN



FIGURE 2.12: mini-ISMARAN 4×4 matrix in laboratory environment.

was operated at the ISMRAN location inside the Dhruva hall. The mini-ISMARAN is a 16% by volume version of ISMRAN. It is made up of 4×4 matrix of 16 PS bars with 32 PMT channels being read out by two V1730 digitizers as can be seen in figure 2.12. These two digitizers are also synchronized before operation. The mini-ISMARAN served as an important testbed for later scaling to ISMRAN. The mini-ISMARAN setup was first setup in the laboratory. Multiple studies have been performed using the mini-ISMARAN setup in laboratory. These include, PS bar characterization, group operation of PS bars with DAQ digitizers, natural background quantification, benchmarking studies etc.

After completion of laboratory based studies the setup was shifted to Dhruva reactor hall at the allocated location. The step-wise assembly of the mini-ISMARAN is shown in the figure 2.13. A $2.5 \text{ m} \times 1.5 \text{ m}$ dimension steel table was used as the base. A layer of 10 cm Pb bricks was laid on the table over two 5 cm thick layers (4 sheets) of borated polyethylene (30% boron) sheets at base. The



FIGURE 2.13: mini-ISMARAN 4×4 matrix with progressively increasing shielding in reactor environment.

matrix was then shifted on to this bottom shield and the other side shields were assembled. To hold the top plane of shielding from collapsing onto the matrix, a 1 cm thick stainless steel sheet was again kept on the side shields. Finally, the matrix was surrounded from all sides by the shielding and held in place using steel angles bolted together. The final prototype setup weighs around 8 tons.

This setup was operated in the reactor 1.5 years. A number of background studies and have been performed using this setup. Also, analysis on the datasets generated for the duration of operation has helped develop the selection schemes for signal events. Long term operation of mini-ISMARAN in reactor environment also indicated feasibility of monitoring Dhruva core using ISMRAN, which is expected to be commissioned with full shielding and trolley structure by first

quarter of 2021.

2.8 ISMRAN PS characterization studies

Plastic scintillators have been used for many years in particle detection for their fast timing response (few 100 picoseconds), wherein energy measurement was derived from the time-of-flight or tracking information. ISMRAN detector on the other hand is utilizing the bulk of PS for energy measurement like a calorimeter, and using the timing information only for filtering out signal events. For these purposes, deriving the energy scale of the PS bars and quantifying their timing response are necessary part of the characterization studies for ISMRAN PS bars. In the studies presented here, the PS bars will be referred using the ID assigned to them, which is of the form: SFXXX, where XXX is the serial number starting from 873 upto 892 for the first set of 20 bars procured for miniISMARAN. Two bars (SF891, SF892) out of these were deliberately ordered without Gd wrapping for study purposes, while 2 more (SF875, SF888) suffered very low PMT gain. Extra Gd foils of the ISMRAN specifications are available and later used for wrapping the SF891 and SF892 bars. For all the bars chosen for miniISMARAN, individual PMT (intra-bar) spectrums and a global (inter-bar) spectral matching needs to be done for achieving uniformity in response for the complete matrix. Corrections for the signal attenuation effects inside each bar need to be taken into account for this matching to be successful. This gain-matching procedure ensures the application of uniform energy scale for the whole volume. Extracting the energy resolution of the PS bar also forms a crucial study. One of the simplest

way to realize this is through the data and simulation comparison for a known γ -ray source. This procedure is discussed in detail after the radioactive source simulation presented in the next chapter. On the timing side, the resolution to events happening inside the bar, whether due to γ -rays or natural radiations such as cosmic muons needs to be studied. Due to the long and linear geometry of the PS bar, its also worthwhile to explore the possibility of using timestamp differences from end PMTs for deducing the interaction position. Following sections elaborate upon the studies performed to address the above discussed characterization aspects for ISMRAN PS bars and the miniISMRAN matrix.

2.8.1 Gain matching

The digitizer output provides the integrated charge of each PMT channel in the form of a raw ADC distribution. These distributions are recorded and studied for the 16 miniISMRAN PS bars using known radioactive sources and the natural background activity. Before starting the gain-matching process, it is necessary to arrive at an optimal setting of factors such as the PMT bias voltages, digitizer input settings of range and threshold and so on. For the PMTs used in miniISMRAN, the maximum allowed bias voltage is -2kV and the advised bias setting for operation as mentioned in the datasheet is at -1800 V. But due to the disparity in the gain of each PMT, the optimum operating bias can range from as low as -1500V to -1900V. Each raw data recorded in ISMRAN PS bars uses digitizer input dynamic range setting of ± 2 V. This range is divided into 32K ADC channels with each channel representing a bin width of 20 fC of integrated charge. This setting is broad enough to accomodate an energy range up to 40 MeV covering low energy

γ -ray energies as well as high energy cosmic muon and any intermediate energy phenomena if present. The chosen threshold is at ADC value of 13 (13×0.12 mV). Figure 2.14 shows the different gains seen in the ADC spectrum of the end PMTs for a ^{22}Na radioactive source placed at the center of PS bar and at the standard voltage of -1800V with above digitizer settings. The distributions shown here covers only about 2.5 MeV and is for representation purpose. To

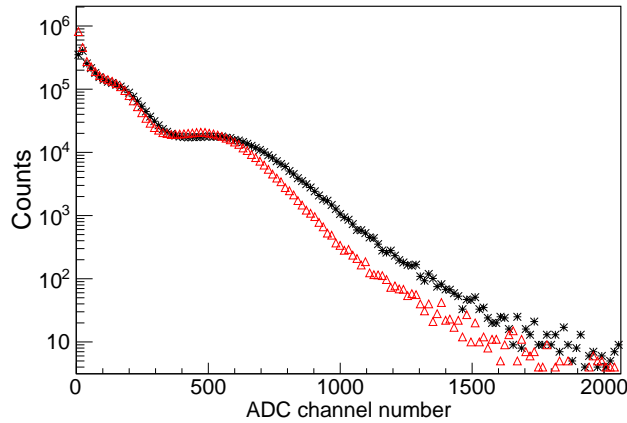


FIGURE 2.14: ADC spectrum of the Near (black) and Far (red) end PMTs of an ISMRAN PS bar at standard operating voltage of -1800V.

realize the gain matching a feature in the source spectrum needs to be used as the common reference point. The compton edge of the 1.274 MeV ^{22}Na peak whose value lies approximately at 1 MeV provides this reference for intra bar PMT gain matching. Later, using the same reference for each bar, automatically achieves the inter-bar matching of gains too. Since the matching is to be done before calibration, a channel number in the raw ADC data needs to be assigned to this feature. We choose the ADC value of 300 to force this feature to lie by giving suitable bias when the source is placed at center of bar. Now, there can be two ways of achieving this requirement 1) repetitive physical adjustments of

PMT bias of each bar to fulfil the above requirement or 2) recording and plotting the channel number of 1 MeV feature for a range of bias voltages and deriving the right bias voltage from a functional fit to this graph. The later procedure is convenient as it eliminates the need of tedious physical re-adjustments to the bias in case of PMT gain drift which is quite likely over long operations. Also physical adjustments may not be possible due to the detector location and access issues. The figures 2.15 2.16 summarize these recorded values for each of the 16 PS bars. It can be seen that with increasing voltage the channel number for the 1 MeV point shifts slightly parabolically. Therefore, a second order polynomial fit is performed and is superimposed on the data points in the plots. Extracting the right bias value then only requires evaluating the inverse function value for ADC value of 300.

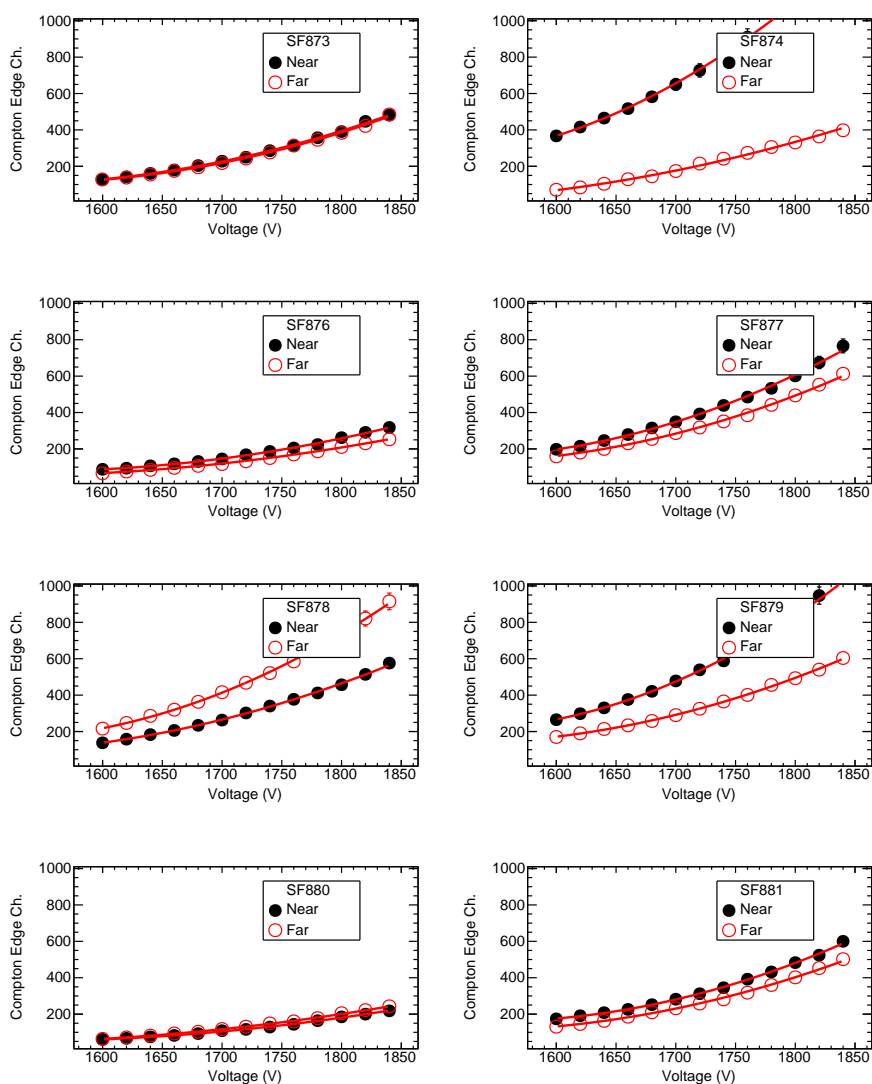


FIGURE 2.15: Compton edge channel numbers for 1.274 MeV ^{22}Na γ -ray plotted for Near and Far PMT ADC spectra at different bias voltages. The resulting graph is fitted with a polynomial function for gain matching purposes.

The result of this procedure can be seen in the natural activity data recorded and overlaid for PS bars. The exact matching of the responses is not ideally possible due to choice of a single feature, but the PS energy resolution is 3–4

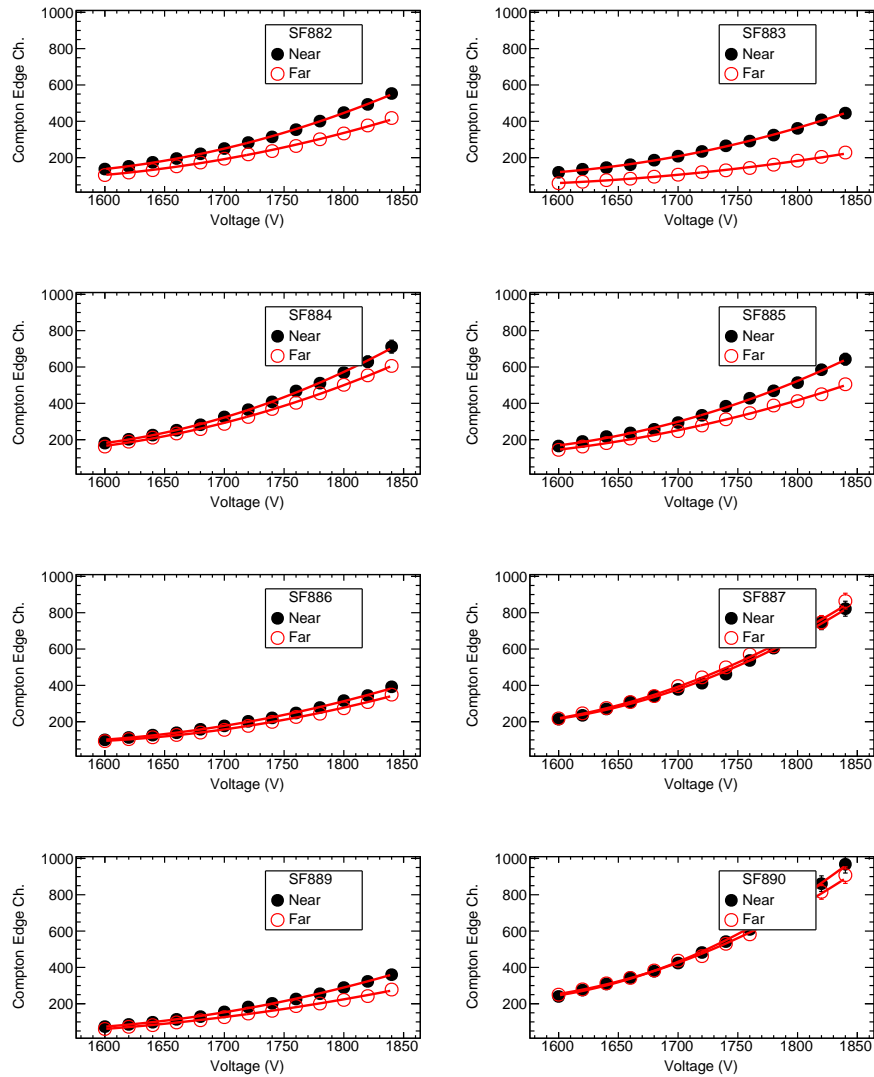


FIGURE 2.16: Compton edge ADC value for 1.274 MeV γ -ray of ^{22}Na source extracted from the ADC spectrum of Near and Far PMT of PS bars SF882 to SF890 at different bias voltages. The resulting graph is fitted with a polynomial function for gain matching purposes.

times broader than the matching deviation. Fig 2.17 shows the unmatched and matched natural background spectra for the 18 PS bars for comparison.

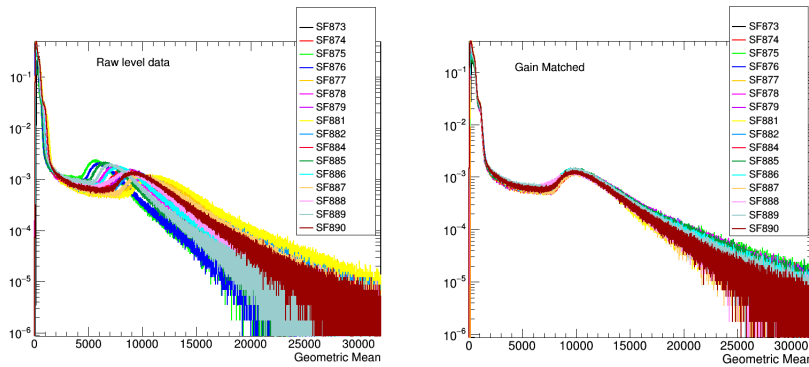


FIGURE 2.17: ADC spectrum of natural activity recorded in 18 of the PS bars. **Left:**Before gain matching. **Right:**After gain matching.

Light attenuation and Geometric mean:

A point worth highlighting is that the gain matching data was taken with radioactive source placed at the center of the PS bar. But in real scenario an event can happen at any location inside the PS bar. In case of an ideal scintillator detector, a simple sum of the PMT output can very well describe the energy deposit since there is no intensity loss expected, but usually there is always a loss. This loss can usually be approximated by an exponential decay formula and is signified by the inclusion of the attenuation length (λ) information for each scintillator composition and assembly. In our case the wrapped EJ200 PS bar has a $\lambda \sim 3.8$ m which is approximately 4 times the length of the PS bar. Even with such a high attenuation length there is a substantial light loss observed. This loss can be quantified by measuring the shift in energy value of a known γ -ray at different distances from the end PMTs. This exercise is carried out by recording ^{137}Cs source data in ISMRAN PS bar starting from center '0' (± 1 cm) to 50 cm on both sides at intervals of 10 cm. Figure 2.18 shows a multipanel plot for the near and far PMT ADC spectra recorded in the above exercise. The compton edge

ADC value is obtained for each distance and plotted as a function of distance with origin at center of PS bar. An exponentially falling distribution is seen as in figure 2.19. The maximum attenuation as measured for the farthest distance i.e. 1 m away from a PMT is $\sim 40\%$.

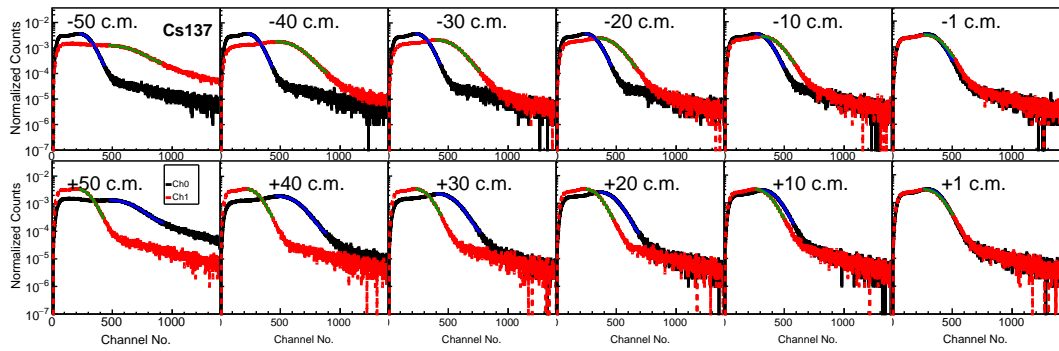


FIGURE 2.18: ADC spectrum of the end PMTs of a single PS bar as the source data is recorded for intervals of 10 cm, from one end to other.

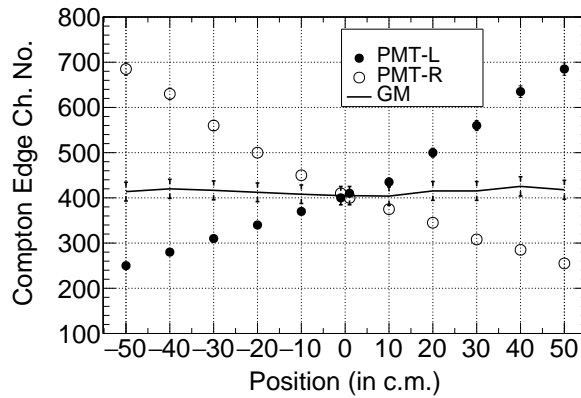


FIGURE 2.19: ADC values of ^{137}Cs compton edge plotted for the near and far PMT at 10 cm intervals. The G.M. is plotted in solid line seen along the center.

Suppose Q_{Tot} , Q_N and Q_F are the total charge and charge recorded by near PMT and far PMT respectively, the approximately exponential nature of light

loss allows a function such as the geometric mean (G.M.) or some form of logarithmic function of the product of charges to be constructed which doesn't have dependence on the distance of ionization site. Among these the geometric mean is often used as it gives a positive real number proportional to the total charge deposited. For a deposit at distance 'x' from near PMT, the function works as follows:

$$\begin{aligned}
 Q_N &= Q_0 \times e^{-\frac{x}{\lambda}} \\
 Q_F &= Q_0 \times e^{-\frac{(L-x)}{\lambda}} \\
 \text{Geometric Mean : } G.M. &= \sqrt{Q_N \times Q_F} \\
 &= \sqrt{Q_0^2 \times e^{-\frac{(L)}{\lambda}}} \\
 &= Q_0 \times \text{constant}
 \end{aligned}$$

The G.M curve obtained for the end PMTs is shown in the solid curve in the middle in figure 2.19. For most of the central region of the bar the G.M. flattens the exponential behaviour, but as we move further away from the center and closer to the PMT some additional non-linear terms start dominating the loss function and the curve deviates. This deviation is well within 4% of the expected channel value. These deviations are also corrected w.r.t a certain chosen bar and universally applied so that the bar responses conform.

The inter-bar gain matching uses these G.M. corrected responses. During the operation, it is very likely that the gain of PMTs may drift unequally. In such a case the fit function for the channel number vs bias voltage helps find a higher

or lower voltage (depending on which way the gain drifts) such that the 1 MeV feature is again shifted to 300th channel. Thus, the ADC scale throughout the volume remains same.

2.9 Calibration

Once the gains are matched the calibration of the PS bars is done for known radioactive sources such as ^{137}Cs (0.662 MeV), ^{22}Na (0.511 MeV and 1.274 MeV), ^{60}Co (1.173 MeV and 1.332 MeV), Am – Be (4.438 MeV). Am-Be also has average 3–4 MeV energy neutrons which can help understand how PS bar responds in a mixed γ -ray and neutron environment. These sources are placed at the center for each bar and about 2 million events each are recorded. Geometric mean of the PMT signals is calculated on event by event basis and spectrum is derived. The crucial part is extracting the compton edge channel value from this distribution. Due to the low-Z composition of the PS, most γ -rays compton scatter and there is negligible amount of photo-electric effect. Thus the ADC spectrum is just a continuum with the highest energy gaussian forming the so-called ‘compton-edge’. The compton continuum is more or less a plateau region and the edge has a gaussian fall as seen in figure 2.14, hence a heaviside function (a reverse turn-ON curve) with a gaussian at its edge is fitted through adjustments of parameters like normalization, gaussian mean and resolution. The edge value is extracted from the fit function. Same procedure is followed for all datasets across all bars. Energy values known for these compton edges are used to derive the energy scale or calibration for upto about 4 MeV energy i.e. compton edge for Am-Be γ -ray, and the energy response is found to be linear within this range.

Figure 2.20 panel (a) shows the calibrated source distributions for three of the γ -ray sources: ^{137}Cs , ^{22}Na and ^{60}Co with activity of $\sim 2\mu\text{Ci}$. Likewise, the PS bar is exposed to 10mCi Am-Be γ -ray and neutron source and the spectrum is recorded. The compton edge of 4.4 MeV γ -ray is visible towards the right end in the spectrum shown in panel (b) of figure 2.20. A slight bump observed at lower energy can be attributed to the mono-energetic γ -ray from neutron capture on H nuclei, as it falls at ~ 2 MeV (compton edge of 2.2 MeV).

The systematic uncertainty due to the gain matching and geometric mean can be grouped together and included with the energy scale uncertainty. The final gain matched spectrum has an uncertainty of 4% and coupled with the compton edge determination uncertainty of 3% an uncertainty of about 5% can be quoted for the final calibrated spectra.

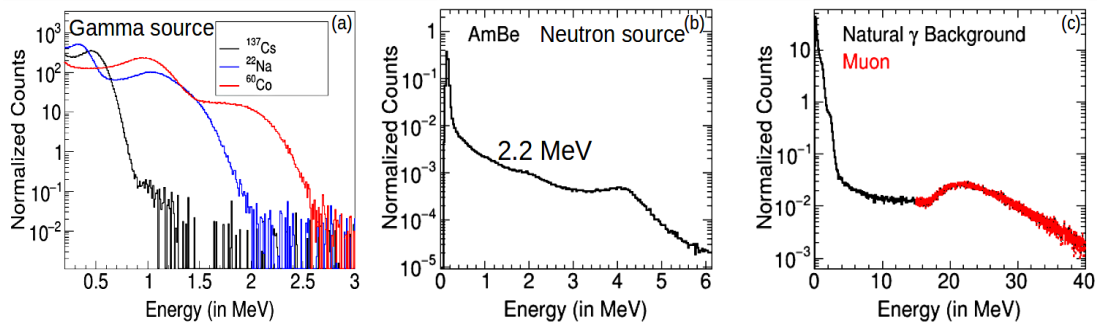


FIGURE 2.20: Energy calibrated distributions for ISMRAN PS bar. Panel (a) shows ^{137}Cs (black), ^{22}Na (blue) and ^{60}Co (red) γ -ray source response. Panel (b) shows the recorded and calibrated Am-Be response. Panel (c) shows the natural background and cosmic muon activity.

High energy cosmic muons are present everywhere and especially for above ground setups their rates are significant. A major component of this cosmic muon flux is in the vertically downward direction in the minimum ionizing region and

hence lose $\sim 2 \text{ MeV g}^{-1} \text{ cm}^{-2}$ (MIP loss). This adds up to about 20 MeV in the 10 cm deep ISMRAN PS bar volume. This is the expected most-probable-value (MPV) of the landau distribution of cosmic muon ionization losses in the bar. Natural γ -ray activities, predominantly the ^{40}K (1460 keV) and ^{208}Tl (2614 keV) are also omnipresent as a background, especially for an unshielded detector. Natural potassium (having 0.012% ^{40}K content) or heavy lanthanide and actinide series elements decaying to ^{208}Tl over long durations, can be part of the setup material (e.g. PMT photocathode) or present in the surroundings SF891, SF892 forming a source for such activity. Figure 2.20 panel (c), shows these backgrounds also calibrated in the PS bar using the source calibration. The ^{40}K and ^{208}Tl compton edges are as seen in left most part of spectrum with cosmic muon distribution on the right marked in red. The coincidence of these compton edges with the right values on the calibration curve help validate the accuracy and long-range linearity of calibration. In a closed detector system with problems of regular access these natural activity features can also help re-calibrate the bar response and is often done in similar experiments.

Event timestamps and timing resolution:

Apart from the integrated charge the digitizer assigns a timestamp to the each pulse. It is done inside its FPGA firmware using a 14 digit counter working on a 50 MHz physical clock in the circuit. The counter can count up to picosecond (ps) level precision in between two timestamps. Each timestamp has two components 1) coarse timestamp and 2) fine timestamp. The coarse timestamp is determined to nanoseconds (ns) due to the sampling rate restriction (2 ns for V1730). The

fine timestamp which corresponds to zero-crossover point of CFD is obtained by interpolating between two neighbouring sample points. This fine-timestamp is the one which helps separate two different events in two channels of digitizer to the single picosecond level. Uncertainties can appear in the fine timestamps due to finite ADC sampling rate (quantization error) and also due to the shape of the pulse. Similarly, the timing resolution is also impacted by the phase of the sampling clock which affects the calculation of delay between two signals. PS are already known to have $O(100)$ ps of resolution possible. This resolution value is possible only for two different detection channels as the PMT response usually has a dead time of 2-3 ns. But even the two channel resolution might vary depending on the nature of EM interaction.

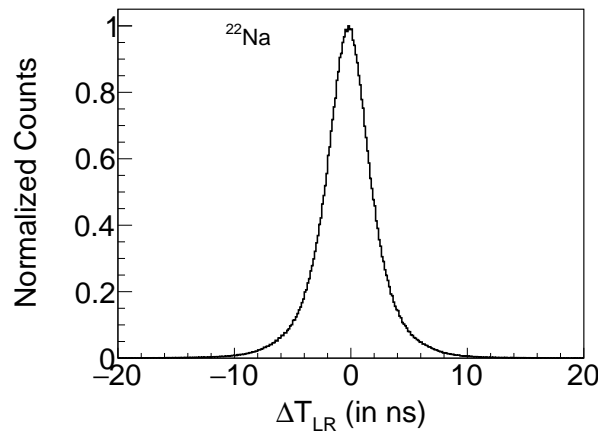


FIGURE 2.21: ΔT_{LR} distribution for ^{22}Na source placed at center of the PS bar.

Intra bar time resolution using γ -ray event:

The IBD detection technique in ISMRAN relies primarily on the γ -ray interaction in PS. Measurements are therefore performed with radioactive γ -ray sources,

with the source placed at the center and the difference of timestamp between left and right PMTs i.e. ΔT_{LR} is recorded and plotted as shown in figure 2.21. The ΔT between two PMT signals is plotted in 16k channel range ($\pm 8K$). The result presented here is without source collimation as the precision improvement expected through collimation is well below a ns. The σ value obtained from a gaussian fit to the distribution is ~ 2 ns. The bottom spread seen in the distribution

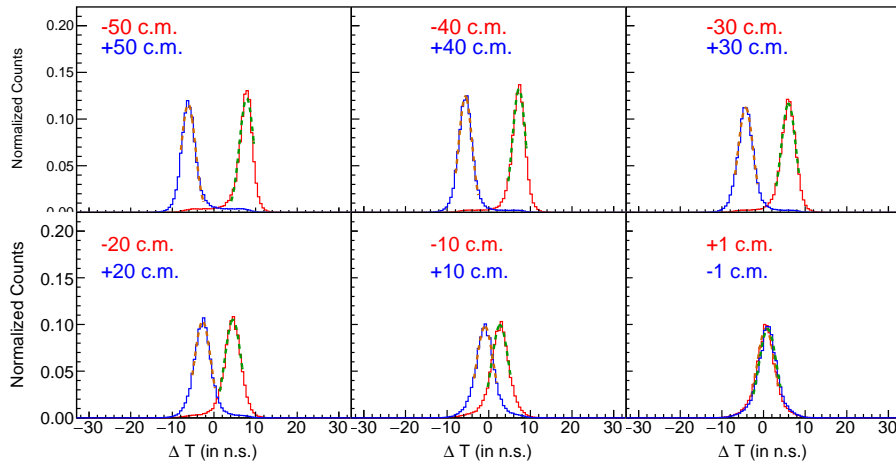


FIGURE 2.22: ΔT_{LR} distribution for ^{137}Cs source placed at different positions along the length of the PS bar.

is due to background and hence the sides have an exponential decay nature. But, due to the very high activity of source, the background contributions can be ignored. To measure the position dependence of the timestamps, the source is placed at different positions at 10 cm intervals starting from center to the edges of the PS bar. For each position offset from the center ($\pm 1\text{cm}$ taken for symmetry) a timestamp offset is observed, as shown in figure 2.22 where the positive and negative equidistant positions from center are plotted together. The multiple timestamp gaussians recorded at each 10 cm interval starting from center of the

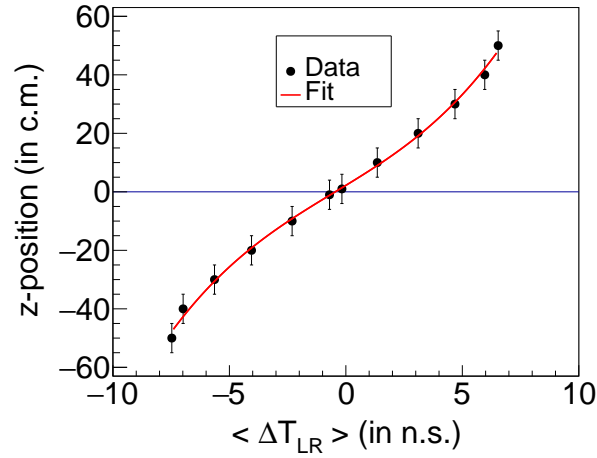


FIGURE 2.23: ΔT_{LR} vs source position graph fitted with polynomial function.

PS bar to the edges are separated from each other just close to the 2 ns value. This implies position resolution of 10 cm for the measured time difference of 2 ns along the length of the PS bar. As shown in figure 2.23, plotting the ΔT vs position data and fitting with a second order polynomial shows small non-linearity towards the edges i.e. beyond 20 cm on both sides from center. Between these marks the relation is more or less linear. The parametrization of ΔT vs Z positions can help isolate the event location along the bar from its ΔT value and this knowledge is utilized in data analysis discussed in chapter 5.

Time resolution from muon events:

The signals due to two γ -ray interaction event in the PS bars are dictated by the Compton scattering phenomenon and the implicit excitation and de-excitation of recoil electron producing the signal. This process is relatively slower as compared to a direct charge particle interaction especially if it's simply dE/dx ionization where there is no shower formation or similar signal broadening phe-

nomenon. The readily available vertical flux of GeV energy cosmic muons is in the minimum ionizing energy region and therefore suitable for determining the timing resolution as they take least amount of time to travel from one detector to another being highly relativistic. The pulses due to cosmic muon interactions have a very steep rising edge and introduce the least latency possible. Thus a study is performed to test the limits of timing resolution achievable in the such a best case scenario. The ΔT measurement for cosmic muons involved using an experimental setup of two PS bars firing within 5 ns coincidence window. The width of the bar causes a substantial energy loss of 20 MeV even for MIP muons as seen earlier. Thus, high energy cut range of 18 to 24 MeV is used to trigger on muons. To ensure triggering on ‘vertically passing’ muons, a selection on $\Delta T_{LR} < 2.0$ ns between end PMTs is chosen. Also, for choosing the cosmic muon events at the center of both bars a cut of $-3.0 \text{ cm} < Z_{\text{pos}} < 3.0 \text{ cm}$ on the event Z position is also used. Figure 2.24 shows the ΔT_{LR} values obtained for such events with a mean of about 1.7 ns representing the average time in which muon is traversing the two bars. A gaussian fit to the distribution yields a σ of 220 ps which is an order of magnitude lower than the 2 ns limit obtained earlier. Repeating the above procedure for two different locations 1) Towards the left at -27 cm and 2) Towards the right at +28 cm from the center shows a shift in the ΔT mean values. The mean obtained in the first case is 1.5 ns and in the second case it is 1.9 ns. But, the σ value doesn’t change from the 220 ps validating that the resolution is not affected by the position.

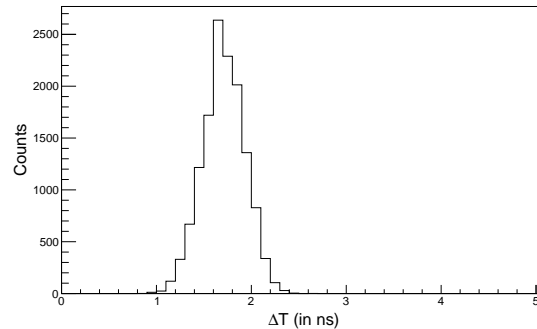


FIGURE 2.24: ΔT distribution for cosmic muons passing vertically through the center of two PS bars.

Correlated event reconstruction using ^{60}Co :

Once the gain matching, calibration and timing response is known we can move to the benchmarking of the whole machinery using event reconstruction. The 4×4 , 16 bar miniISMARAN array in laboratory is used for taking natural background data and also to study correlated events mimicking the IBD like signature. Correlated γ -ray events from known radioactive sources can be studied for the above purpose. ^{60}Co has two correlated medium energy γ -rays of 1173 keV and 1332 keV produced in the same decay separated by only a few picoseconds and is useful test bench for the IBD annihilation γ -ray and the cascade γ -ray events inside miniISMARAN geometry. Am-Be source with its γ -ray and neutron signature is also a potential source candidate. But, its γ -ray is of high energy 4.4 MeV which is capable of producing a shower event. Also, the neutron spectrum is in the MeV range unlike the IBD neutron which is only a few keV. Both features can be hard to contain inside the limited miniISMARAN volume.

To carry out the exercise, two data sets are recorded. Firstly, the ^{60}Co source is placed at the center of 4×4 matrix. Data is recorded in minimum bias condition,

with each PS bar in the couples mode i.e. coincident PMT hits above 0.2 Mev and within 16 ns window are recorded. Energy deposits or hits are sorted and summed up in successive 40 ns windows using their timestamp information. These summed up hits are tagged as individual events and analysed. This same procedure is repeated with the natural background activity. For the ^{60}Co γ -rays the sum of the energies is known to be 2.505 MeV. This information can be used to differentiate signal events from background. Events are further categorized as 2 bar, 3 bar, 4 bar, 5 bar, 6 bar events and so on. Each such category of events has its own sum energy distribution. By comparison of these sum energy distributions (figure 2.25), it is observed that for events upto 4 bar groupings i.e. 2, 3 and 4 bars the sum energy of recorded events progressively increases. There are two features in the sum energy distribution, first is an intense peaky structure at low energy which can be attributed to the ^{60}Co signal events and second is a broad and low gaussian feature scaling with the natural background.

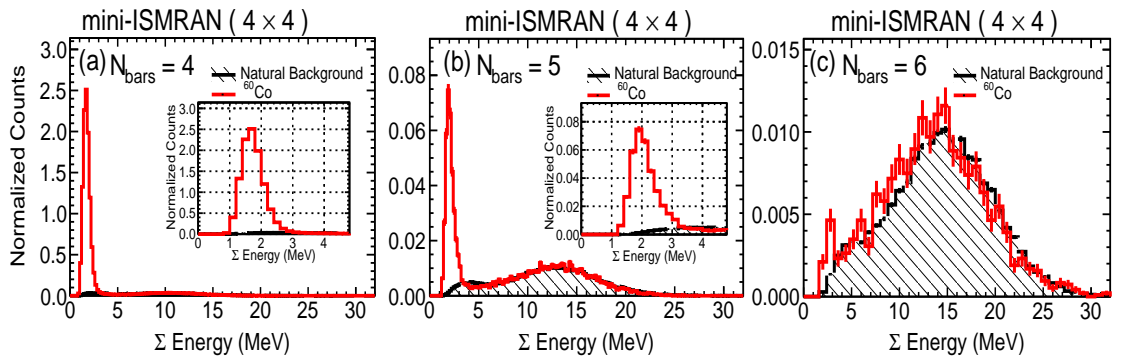


FIGURE 2.25: The sum energy distribution within 40 ns time window, (a) $N_{\text{bars}} = 4$, (b) $N_{\text{bars}} = 5$ and (c) $N_{\text{bars}} = 6$, for the ^{60}Co (solid histogram) and natural background (filled histogram) events. The insets in panel (a) and (b) shows the zoomed x-axis of the sum energy distribution for the ^{60}Co source and natural background.

For 5 bar events the low energy peak is at ~ 2.1 MeV close to the 2.5 MeV expectation while the average background is close to 12 MeV. But, including one more bar in summation i.e. 6 bar groups has non-significant low energy peak compared to the background gaussian. This implies that the 5 bar category allows to select the signal events with high purity and that the expected sum energy has a specific bar multiplicity signature. In more elaborate terms, the γ -ray event being summed up for energy decides the number of bars that are needed to fully contain it. Thus event classification in a segmented but moderately bulky volume like ISMRAN can use these two characteristic features.

2.10 Summary

ISMARAN a moderate ton-scale detector is in development at BARC, for monitoring and short baseline oscillation searches. The Dhruva reactor offers a unique facility of a sufficiently powerful research core using natural Uranium fuel. ISMRAN uses plastic scintillators as the detection medium which is relatively uncommon in the context of reactor $\bar{\nu}_e$ detection but due to its non hazardous nature and convenient handling offers a safe approach to monitoring. The high backgrounds in the reactor hall are expected to be countered by the combination of a moderate 10 cm Pb and 10 cm BP shield and a powerful DAQ based on digitizers. The digitizer DAQ has been benchmarked and ready for operation with the 200 channel ISMRAN array.

A prototype mini-ISMARAN has been setup and operated in laboratory environment for characterization and benchmarking studies. Synchronized operation of DAQ has been tested in the laboratory using cosmic muons. PS energy and

timing response has been studied using the available PS bars. Correlated events from ^{60}Co γ -rays have been reconstructed in miniISM-RAN using optimal sum energy and N_{bars} combination.

Chapter 3

Detector Simulations

3.1 Simulation setup for ISMRAN

Monte-Carlo simulations for the ISMRAN detector are carried out using the GEANT4 [73] package. The ISMRAN detector geometry as simulated in GEANT4 is shown in the Fig 3.1. The scintillator volume is a modular geometry of 100 individual sensitive PS detectors of EJ200 composition and dimensions $100\text{ cm} \times 10\text{ cm} \times 10\text{ cm}$ forming a matrix of ~ 1 tonne weight. The Gd wrapping of 4.8 mg cm^{-2} on each bar amounts to a total of 0.18 %w/w of the full detector [65]. The properties/parameters of the whole ISMRAN volume, PS and PMTs used in the simulation are listed in the table 3.1. Each PS bar has a wrapping of 98% reflectivity diffuse reflector. The shielding of 10 cm thick

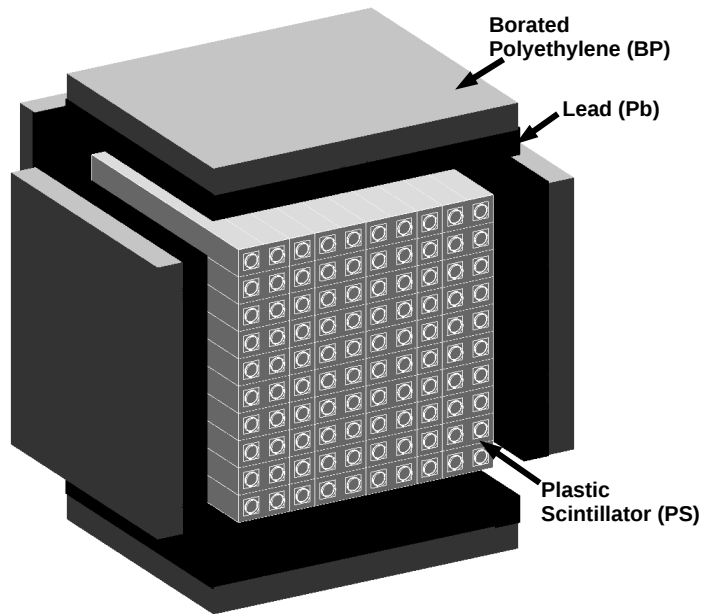


FIGURE 3.1: Cross-sectional view of ISMRAN detector in simulation.

Pb and 10 cm thick BP, each in the form of single uniform $100\text{ cm} \times 100\text{ cm}$ sheets for all sides is used in simulation. Due to the closely packed chevron (interlocking) design of Pb bricks and large (50 cm^2) sections of BP kept in a staggered arrangement, there is negligible free-streaming of particles and hence the uniform shield approximation is valid.

GEANT4 offers a variety of physics lists i.e. sets of physics interactions which users can include as per their simulation needs. For the case of ISMRAN, the primary physics requirements include electromagnetic interactions for positrons, electrons, γ -rays and hadronic interactions for neutrons, mostly low energy ones, produced in IBD. High energy particles such as cosmic muons, neutrons and ions also need to be simulated. To simulate these particles and their interactions in the expected energy ranges, the standard electromagnetic physics, ion physics and

TABLE 3.1: Detector parameters in simulation

Parameter	ISMРАН detector components
ISMРАН detector:	
Detector Volume (m ³)	1
No. of PS (PMT)	100 (200)
PS bar [68]:	
Scintillator composition	EJ-200
Gd conc. (% w/w)	0.18
Free proton per cm ³ of scintillator	5.17×10^{22}
Light Output (% Anthracene)	64
Light Attenuation Length (cm)	380
Density (g/cm ³)	1.023
Polymer Base	Polyvinyl-toluene
Birk's constant ($10^{-3} \text{g} \cdot \text{cm}^{-2} \cdot \text{MeV}^{-1}$)	11.5 [74]
Detector Mass (tonne)	~1
Quantum efficiency of PMT	~30%

radioactive decay physics are incorporated. Optical processes for scintillation photons have not been turned ON for reducing simulation time and efficient use of computational resources. The production thresholds for secondary particles are kept to the default values except for the electrons and positrons which are at 0.01 mm. An important inclusion is of the QGSP_BIC_HP physics specially for hadron interactions [75]. This physics implementation in GEANT4 uses the binary cascade model which better describes the secondary particles production in interactions of protons and neutrons with nuclei. It also includes the 'G4NeutronHPCapture', which is high precision, data-driven physics package for transport of neutrons below 20 MeV to thermal energies. For the radiative neutron capture, the default process for the de-excitation of Gadolinium nucleus to produce γ -ray cascades is the 'final state' (FS) method in the chosen physics

package.

Fuel monitoring and input $\bar{\nu}_e$ spectrum

A $\bar{\nu}_e$ detector with a modest S:B ratio $\lesssim 1$ can discriminate the reactor ON state from the OFF state, and, with better background rejection and reduced uncertainties following the reactor power level changes is also achievable in a quasi real-time manner. However, for a moderate size detector to gain sensitivity to the fuel evolution or sterile oscillations requires accurate modeling of the $\bar{\nu}_e$ spectrum emitted by the reactor core. This model when compared to the

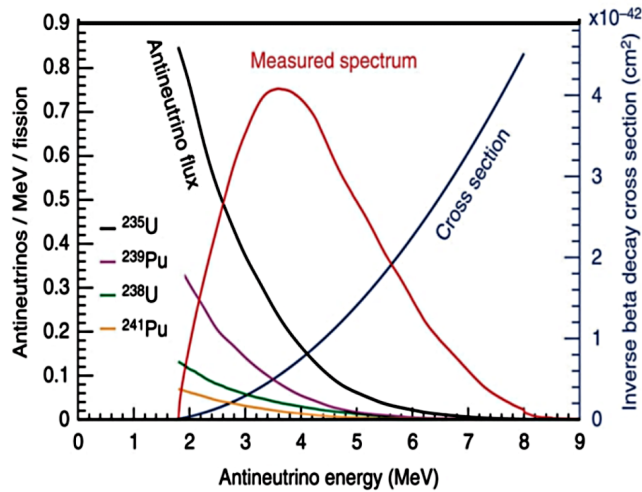


FIGURE 3.2: Relative $\bar{\nu}_e$ flux due to different isotopes convoluted with IBD cross-section to give measured spectrum in detector [76].

measured spectral shape of reactor $\bar{\nu}_e$, helps in determining the source of the spectral distortion. This can be illustrated using the example of a low-enriched uranium (LEU), light water reactor having $\sim 4\%$ ^{235}U . This has been the most common type of reactor for generating power using nuclear technology. The

number of fissioning nuclei at the start of operation is dominated by ^{235}U with relatively lower contribution from ^{238}U , since ^{235}U has the highest $\bar{\nu}_e$ flux. With time, the uranium fuel gets used up in the fission process for producing energy output referred to as the ‘burn-up’ which is expressed in terms of GW-day/tHM (Gigawatt-day per tonne of heavy metal (Uranium)) units. Consequently, ^{239}Pu and ^{241}Pu content builds up and increasingly more fission happens from these isotopes, unless, a refueling is done.

The $\bar{\nu}_e$ spectrum as measured in an IBD based detector is a convoluted product of the $\bar{\nu}_e$ flux from the reactor core and IBD cross section as shown in Fig 3.2. Due to the changing fuel composition with burn-up, increasingly more neutrinos due to ^{239}Pu form part of the emitted flux and consequently in the spectrum measured by an IBD detector. The Fig 3.3 shows this changing flux contributions and the difference between the detected $\bar{\nu}_e$ rates and spectral shape for fission neutrinos due to the dominant Uranium and Plutonium isotopes. The observed rates due to plutonium are significantly lower and the spectral shape is shifted to lower energies. Quantifying this change can facilitate commenting upon the plutonium build-up.

For a realistic simulation of IBD events in ISMRAN, fission fractions and flux parametrization from [79, 80] are chosen. The cross-section calculations are taken from [48, 81]. Using these inputs, and two body kinematics the energies of daughter particles of IBD interaction – positron and neutron, are derived, while their momentum direction are randomized. The source co-ordinates of the neutrinos inside the core are generated randomly in its cylindrical volume using Bessel function. Their interaction vertices in detector are randomly generated throughout the volume. In the following sections the results from simulation

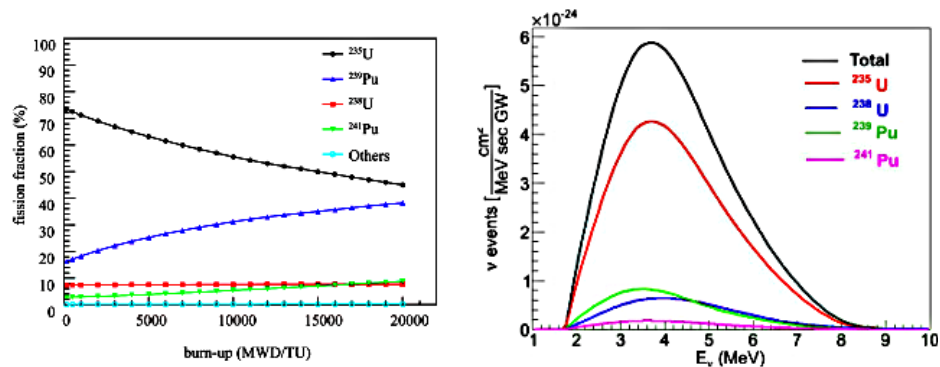


FIGURE 3.3: **Left:** Evolution of isotopic fission fractions with fuel burn-up [77] and **Right:** The IBD spectrum due to the dominant core fuel isotopes highlighting the disparity in their spectrum [78].

of ISMRAN shielding are discussed first, followed by IBD event simulations to obtain event variable distributions. An estimate of the $\bar{\nu}_e$ detection efficiency is then derived, based on the suitable selection criteria on simulated IBD events.

3.2 ISMRAN simulation results:

Results from shielding simulations

ISMRAN is planned to be operated inside the reactor hall and above-ground. A neutron guide tube runs close to the setup at about 2 m distance away from the allotted location. This setting exposes the detector to plenty of background radiations like γ -rays and neutrons. The energies of penetrating background γ -rays can extend from few 100 keVs to 10 MeV and so is the case for the neutrons. As the proposed ISMRAN setup is expected to be a standalone structure with arrangement for movement using a trolley base, the overall tonnage of the detector and shielding needs to be constrained. Increased shielding will increase

the load and will require a more robust and heavy trolley base structure for a steel based composition. Also, the average load bearing capacity of the Dhruva reactor floor (30 tonnes/m^2) is not to be exceeded. Similar considerations are likely for any other site where ISMRAN could be operated in future. Keeping these constraints in view, shielding simulations are carried out to arrive at an optimal shielding arrangement to balance the needs of background suppression and tonnage constraints.

The γ shielding structures involve the use of high-Z materials, preferably

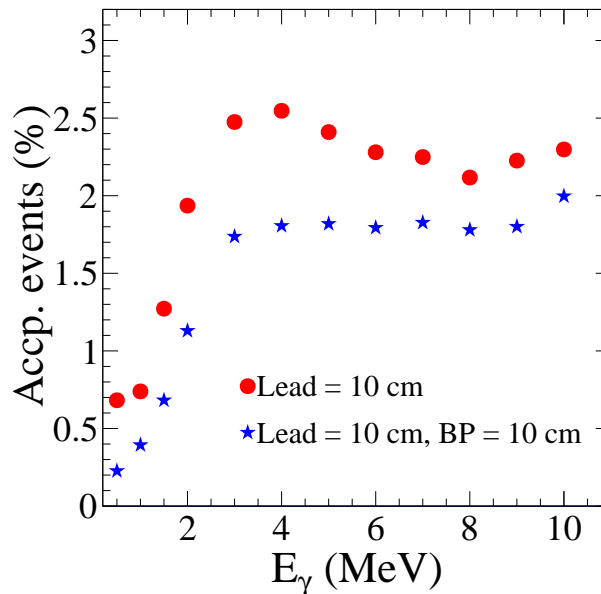


FIGURE 3.4: γ -ray acceptance of Pb and Pb+BP shield for ISMRAN.

Lead(Pb) as it is the highest atomic number element with a naturally abundant stable isotope ^{208}Pb . Neutrons on the other hand, can't be simply absorbed due to their neutral nature and hence are more penetrating. But they can be made to lose energy and undergo capture in low-Z elements like Hydrogen, Boron. For the γ shielding, simulation is carried out in GEANT4 using γ photons as

primary particles incident on a uniform Pb shield. Due to ready availability of 10 cm thickness lead (Pb) bricks from a previous experimental setup, this thickness was tested in simulation. The Fig 3.4 shows the result of this simulation in red markers. The γ acceptance of 10 cm Pb shield rises from about 0.5% for energies below 1 MeV, to maximum of $\sim 2.5\%$ for energies above 3 MeV. The acceptance nearly saturates around this value and the slight dip seen in the distribution at energies between 5–9 MeV is due to the shift in the energy loss mechanism from Compton scattering towards pair production. To incorporate neutron shielding also, a 10 cm thick borated polyethylene (BP) sheet with 30% natural boron doping (19.9% ^{10}B and rest 80.1% ^{11}B) is then introduced in simulation outside the 10 cm Pb shield. The hydrogenous polyethylene material is good for energy loss through elastic scattering while boron captures neutrons with high cross-section (~ 3840 b for ^{10}B) once they reach thermal energies. Boron is also easy for doping into polyethylene than higher elements and also has lower energies of emitted γ photons which can be absorbed by the following layer of Pb. With inclusion of the 10 cm BP shielding the γ acceptance percentage is even reduced below 2% for all energies of incident γ -rays, shown in blue markers in Fig 3.4. Subsequently, the acceptance of this double-layered arrangement to intermediate and fast neutrons is tested in simulation, using a 10 cm Pb shield in combination with increasing thicknesses: 7 cm, 10 cm and 15 cm of BP shielding on the outside. The results for these simulations are shown in Fig 3.5. Neutrons below 1 MeV are significantly suppressed for both 15 cm and 10 cm BP thickness, while 7 cm thick sheet is already not much effective. For energies beyond 1 MeV, all configurations approach a similar acceptance of 10–12% and don't allow most neutrons of energies > 10 MeV. The 15 cm BP sheet is obviously the best among

the three, but not an order of magnitude improvement, over the 10 cm thick BP configuration.

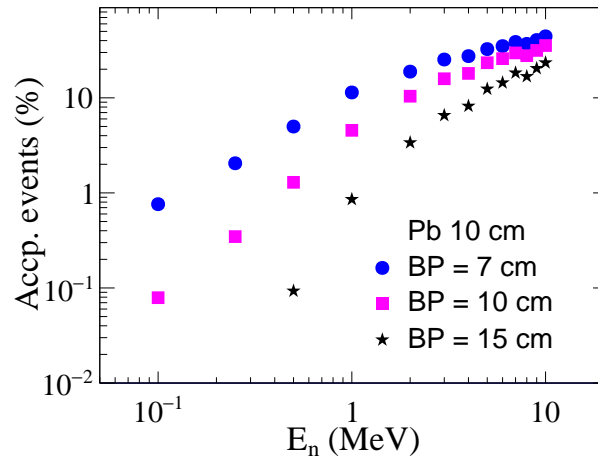


FIGURE 3.5: Fast neutron acceptance of different thickness of Pb+BP shield.

A study to evaluate flux of cosmic ray induced neutrons penetrating the ISMRAN shielding is also done on the same lines as the above exercise. Neutrons which are part of the cosmic ray showers range over energies from meV to 100s of GeV by the time they reach sea level. Due to availability of an inch thick HDPE for neutron thermalization, and a plan for their incorporation in future specially for neutron background, the simulation was performed by putting a single sheet in addition to the 10 cm Pb and BP arrangement. The sea level flux is taken from the Ref [82] and incident vertically upon the ISMRAN setup. The Fig 3.6 shows the results of this study. Again the neutrons with energies beyond 1 MeV are not effectively shielded. These events need to be studied for their signature in ISMRAN as they can create correlated hits in multiple bars. This will be discussed in the later section on cosmic background simulations.

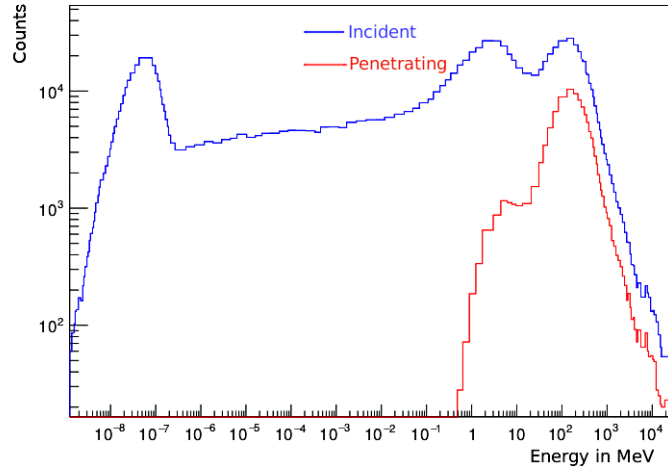


FIGURE 3.6: The incident (blue) and penetrating (red) cosmic neutron flux for the ISMRAN shielding.

Extracting energy resolution

ISM-RAN detects $\bar{\nu}_e$ through a two-fold signature of positron annihilation and neutron capture γ -rays. Thus, known γ -ray source data recorded in the ISMRAN PS bar is necessary to understand its energy response for calibration and energy resolution. Out of these two properties, finding energy resolution of the detector becomes foremost exercise for such experiments which require precision energy spectroscopy. In most γ -ray detectors, the background or continuum part is subtracted out or is negligible as compared the full energy deposition peak (photo-peak). Obtaining the energy resolution in such cases is straightforward, and is defined as a ratio of full width at half maximum (FWHM) to the mean value H_0 of this photo-peak, usually expressed as a percentage

$$\text{Resolution} : R = \frac{FWHM_{overall}}{H_0}$$

$$\text{where, } FWHM_{overall}^2 = FWHM_{statistical}^2 + FWHM_{noise}^2 + FWHM_{drift}^2 + \dots$$

The energy response, having these different random fluctuations, can be represented by a Gaussian distribution and its ‘ σ ’ is usually considered a representation of the resolution. Taking an ideal case of an infinite size detector (ideal calorimeter) with no instrumental effects, the intrinsic energy resolution is simply due to the stochastic processes involved such as ionization of medium and other processes of charge particle production. The energy resolution $\sigma(E)$ for such an ideal detector is given by:

$$\sigma(E) = \sqrt{E};$$

and is expressed in the fractional form as,

$$\frac{\sigma(E)}{E} \equiv \frac{1}{\sqrt{E}}$$

For a realistic detector, where additional contributions to fluctuations deteriorates the resolution, the above expression is generalized as,

$$\frac{\sigma(E)}{E} = a \oplus \frac{b}{\sqrt{E}} \oplus \frac{c}{E}$$

The \oplus sign is used to signify quadrature sum. The different terms in the summation are:

- Constant term : This is the first term ‘a’ which represents the energy independent contributions to resolution for e.g. due to instrumental effects.

These effects may originate from the detector geometry, mechanical structure imperfections, readout system, detector ageing and radiation damage etc. The problems in detector geometry and readout can be corrected, but, mechanical imperfections are difficult to completely remove.

- Noise term : This is the third term ' $\frac{c}{E}$ ' which represents the readout electronic noise and has its source in the technique used in detector and features like detector capacitance and cables etc. Scintillator based systems collect signal in the form of light produced using PMTs which have high gain multiplication with very low noise, while charge based signal collection involves pre-amplifier which introduce a lot of noise especially at higher signal rates. This factor increases with decreasing energy of incident particle and its allowed level is usually decided based on operational energies of the experiment.
- Stochastic term : This is the most fundamental term ' $\frac{b}{\sqrt{E}}$ ', and represents the intrinsic fluctuations in charge particle production in processes like ionization, electromagnetic shower or similar phenomena of signal production. The value of this term usually range from 5–20%/ \sqrt{E} for scintillator based setups like ISMRAN.

Using this three term function and appropriate parameter adjustments the γ -ray response of ISMRAN PS bar is smeared in simulation. For validation purpose, the ^{137}Cs source data is used to compare measurement and simulations. This comparison of measured calibrated energy distribution from data (solid symbols) and simulated energy distribution (dashed histogram) in GEANT4 for a single PS bar is shown in figure 3.7. The energy range used in this comparison

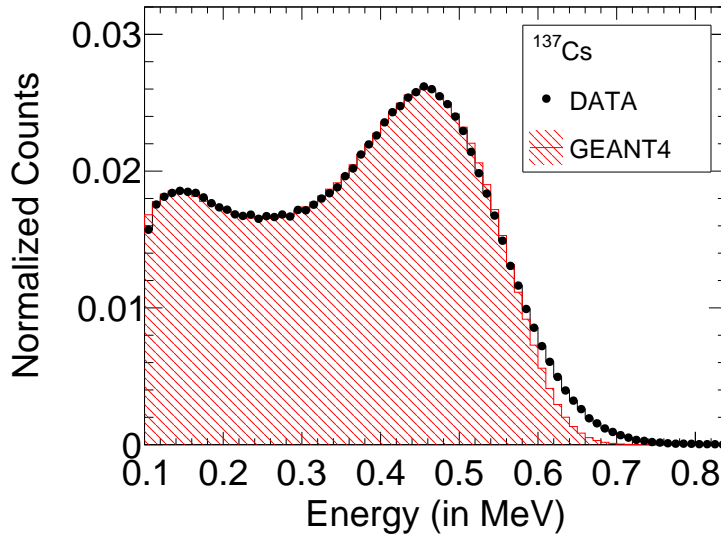


FIGURE 3.7: Comparison of energy distribution between data (solid) and simulation (dashed) from a ^{137}Cs source spectrum in a $100\text{cm} \times 10\text{cm} \times 10\text{cm}$ PS bar. The simulation results are smeared for the energy resolution of the plastic scintillator bar.

is from 0.2 MeV to 8 MeV which are the lower and upper threshold energies for ISMRAN event selection. The dominant factor i.e. the stochastic term in energy resolution function is found to be : $\sim \frac{20\%}{\sqrt{E}}$ to get a reasonable agreement with the measured data. Although there are still disagreement between data and simulation observed in the results beyond 0.5 MeV, these are mainly due to lack of modeling of natural background component in the simulation results. The linearity of energy response using the radioactive source data and the full energy resolution function as obtained from simulation fit is shown in figure 3.8.

3.2.1 Results from IBD event simulations

Once the positron and neutron particles are produced using the IBD reaction kinematics, they are propagated and tracked by GEANT4 inside the ISMRAN

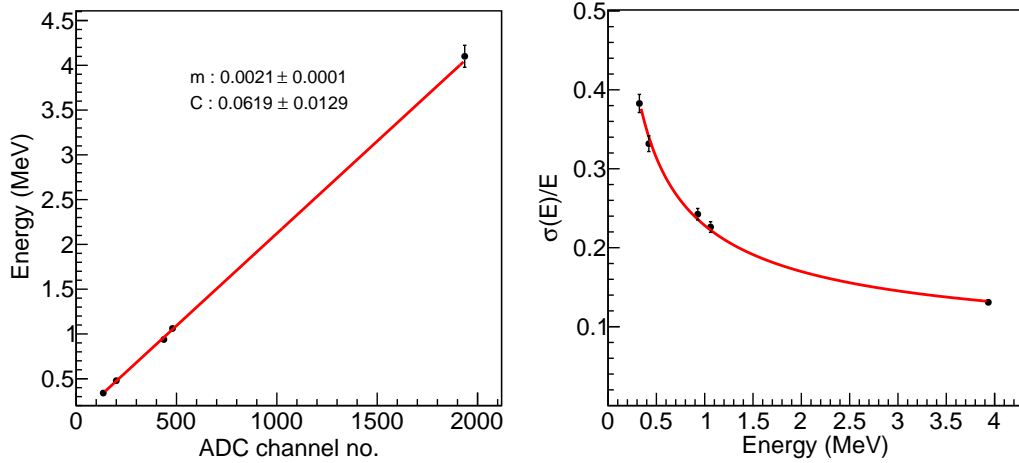


FIGURE 3.8: **Left:** Linear energy response curve for ISMRAN PS bar showing γ -ray source data points, **Right:** Energy resolution curve for ISMRAN PS bar obtained from the same source data points.

volume. GEANT4 directly provides all the required variables including energy signature while in case of the recorded data, the bar energy deposit is obtained by integrating the charge output of PMT signal into digital channels using a charge to digital converter or ‘QDC’. The time window for charge integration or the so-called ‘Long-gate’ is set at 144 ns. This specific gate width was chosen, as it was found sufficient for the containment of both, the lower energy pulses due to γ -rays as well as high energy pulses due to cosmic muons without saturation effect. The figure 3.9 shows a simulated IBD event inside the ISMRAN. The tracks due to positron (pink), neutron (yellow) and γ -rays (green) are depicted. For a segmented volume like ISMRAN, the number of segment hits registered in an event is a useful information, while, this advantage is not present in the case for a homogeneous volume. Three primary event variables that characterize an IBD event for the ISMRAN geometry are :

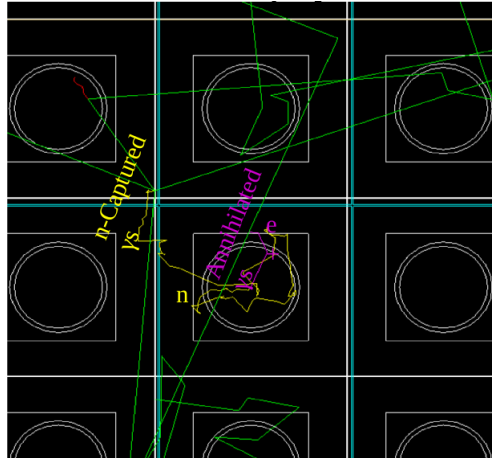


FIGURE 3.9: IBD event simulated inside ISMRAN geometry depicted using separate color coding for each particle.

- **Sum Energy** : As the name suggests, the ‘sum energy’ variable is just the addition of total energy deposits in the detection volume. This variable is common for any energy based event detection where multiple signal readouts are involved. This can be the case for a bulk volume being readout using multiple sensors e.g. a homogeneous LS volume with multiple PMTs, or where the detector itself is segmented and each segment has its own readout as in ISMRAN. In case of an IBD event, the ‘sum energy’ variable can be calculated for the positron annihilation event as E_{prompt} and the neutron capture event as E_{delayed} . Their expected values are:

$E_{\text{prompt}} = (E_{\bar{\nu}_e} - 0.784) \text{ MeV}$. This implies that prompt spectrum follows the $\bar{\nu}_e$ spectrum and its expected energy range and shape is therefore more or less known.

E_{delayed} is $\sim 8 \text{ MeV}$ since the neutron capture reaction takes place on Gd which goes into an excited state of its more massive isotope. This isotope then de-excites and emits cascades of γ -rays adding up to values specific

to the isotope. For ^{157}Gd it is 7.9 MeV and for ^{155}Gd it is 8.5 MeV.

- N_{bars} : This variable is specific to ISMRAN segmented geometry of multiple PS bars. Since the signal is dependent on γ -ray interactions, the event becomes more spread out as it scatters in multiple PS bars and deposits energy (hits). N_{bars} is the number of different PS bars hit in a prompt or delayed event. As the interaction length and shower formation probability for γ -rays in scintillator volume increases with increasing energies, the 511 keV positron annihilation γ -rays are expected to produce hits in less number of bars as compared to higher energy cascade γ -rays due to neutron capture. Thus, a distinction can be made between prompt and delayed events based on the N_{bars} variables.
- Mean time delay : This variable is the average time delay expected between the prompt and delayed events from IBD. This mean time delay is different for different detectors and depends mostly on the neutron capture agent concentration and location in the volume. Homogeneous doping in LS detector leads to smaller time delays while in detectors like ISMRAN, where Gd is around the PS bar edges the mean time delay is larger.

The typical values for these three variables are studied in the ISMRAN geometry for prompt and delayed signature of IBD event. A lower threshold of $E_{\text{Th}}^{\text{bar}} > 0.2$ MeV, is applied on the deposited energy of each PS bar in simulation along with an upper threshold of 7.5 MeV to reject cosmics. This is done to achieve spectral uniformity among different bars similar to PS bar data from reactor environment. The scintillator volume of each PS bar is considered as

sensitive detector in GEANT4 and each bar's hits are stored in a container for processing. A tree structure holds the event by event information of antineutrino energy, corresponding positron and neutron energy, the different PS bars hit and their energies for the prompt and delayed event. These prompt and delayed events also have further classification of hits, as in, whether a hit is due to the primary particle (positron or neutron) or a secondary i.e. γ -ray interaction. The 'sum energy' for an event is calculated in analysis as the sum total of all the deposited energies in all bars, in that event, with energy above the 0.2 MeV threshold. Similarly, the N_{bars} is the count of bars with hits above this threshold where repeating bars are excluded in counting. These variables are evaluated for 10^6 IBD events simulated in ISMRAN geometry. The prompt positron event and delayed neutron event can be studied separately as two separate components of the $\bar{\nu}_e$ induced IBD reaction due to the different physics processes involved and the time scales of their occurrence.

Prompt positron event

The N_{bars} distribution obtained for the prompt positron event in IBD simulations are compared for nominal threshold and 0.2 MeV threshold applied in data, as shown in figure 3.10(b). The reduced N_{bars} range of events under 0.2 MeV threshold is indicative of the fact that there are multiple low energy deposit bars in the nominal threshold case which get rejected by the threshold condition. The threshold also brings out a peaky structure around 2–3 bars which is then used to further improve prompt event selection by including the $1 < N_{\text{bars}} < 4$ cut. The simulations also provide the prompt sum energy distribution which are again compared for nominal threshold and 0.2 MeV threshold is shown in figure 3.10(a).

The prompt event signature comprises of ionization energy loss by positron and energy deposited by recoil electrons in the Compton scattering of annihilation γ -rays. Due to its tiny mass as compared to the neutron, positron carries most of the kinetic energy of the $\bar{\nu}_e$ in IBD. This fact is reflected in both the prompt sum energy distributions which resemble the $\bar{\nu}_e$ spectrum above the 1.806 MeV IBD reaction threshold. The imposed 0.2 MeV threshold and $1 < N_{\text{bars}} < 4$ condition, causes the overall sum energy distribution to shift to lower energy but keeps the spectral shape intact. The mini-ISMARAN which is the prototype detector having a 4×4 geometry of 16 PS bars is also studied in IBD simulations. Due to the limited spread of the positron event the sum energy and N_{bars} signature remain the similar even in its reduced volume. The difference appears in the efficiency (event count rates) which is significantly reduced.

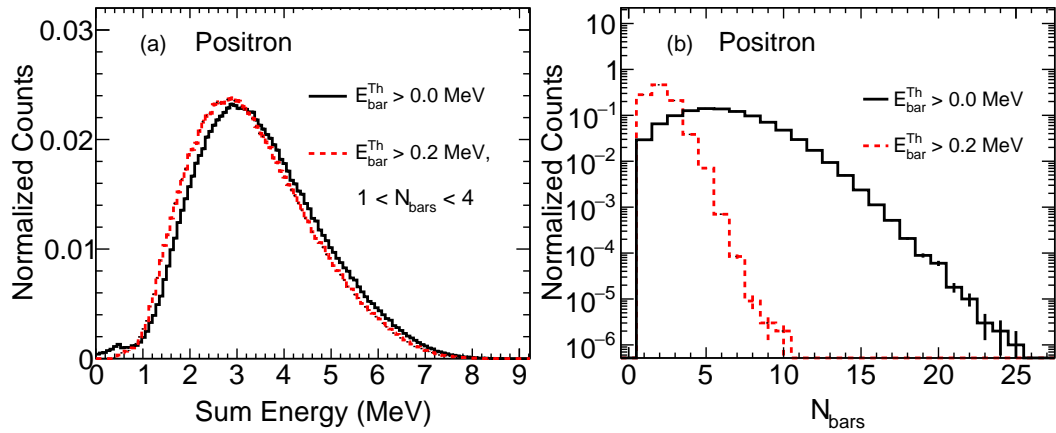


FIGURE 3.10: Sum energy (left) and N_{bars} (right) distributions for prompt positron event in ISMRAN for nominal and 0.2 MeV threshold.

Delayed neutron event

IBD simulations in ISMRAN geometry, also helps to understand the element-wise capture percentages of IBD neutrons. The very high thermal neutron capture cross-section of Gd, $\sim 10^5$ barns, leads to a high percentage of captures to happen on Gd, while due to the abundance of H nuclei in the bulk volume a good fraction of captures also take place on H even though its thermal neutron capture cross-section is only about 0.3 barn. Small fraction of the IBD neutrons, produced around the edges, could come out and get captured on the Pb shielding, while a tiny fraction completely escaped the setup. The actual percentage of captures observed for the different nuclei are as listed in table 3.2. The location of the majority captures due to Gd and H nuclei can be seen in a cross-sectional profile view of the ISMRAN geometry as shown in figure 3.11 which brings forth the wrapping-arrangement of Gd neutron capture agent.

TABLE 3.2: Element-wise capture fractions for IBD neutron in ISMRAN, sorted in descending order.

Element	Fraction of captures (%)
Gd	73.0
H	25.0
Pb	1.0
C	0.5
Others or escaping	0.5

An important variable which can be extracted at this stage is the ‘mean time delay’ between the prompt and delayed events which is characteristic to the capture profile obtained and hence to the adopted detector geometry. The impact of capture agent concentration and location inside an inhomogeneous detection

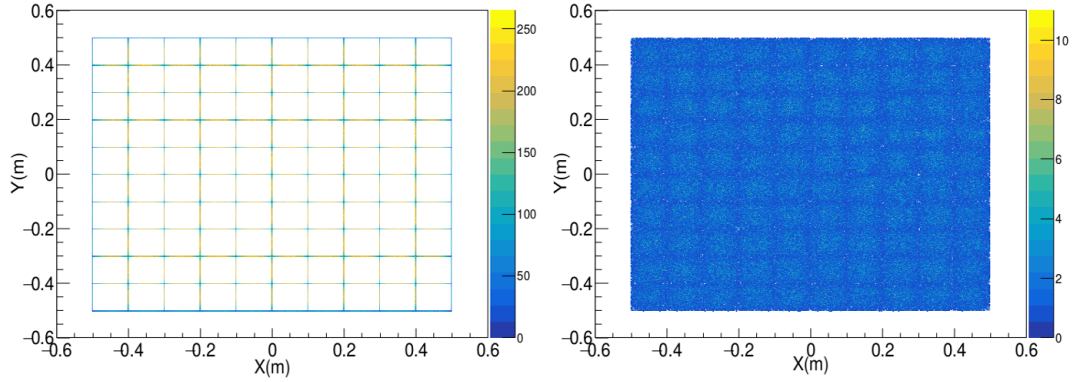


FIGURE 3.11: IBD neutron capture event position profile highlighting the two major capture location due to elements: Gd on left panel and due to H on right panel

volume is studied in detail in the Ref [83]. The mean time delay variable helps select $\bar{\nu}_e$ candidate events in ISMRAN by studying the time correlation between the prompt and delayed events due to IBD interaction. Using GEANT4, we have studied the capture time of the emitted neutron from IBD events in the ISMRAN detector volume. Figure 3.12, shows the neutron capture time

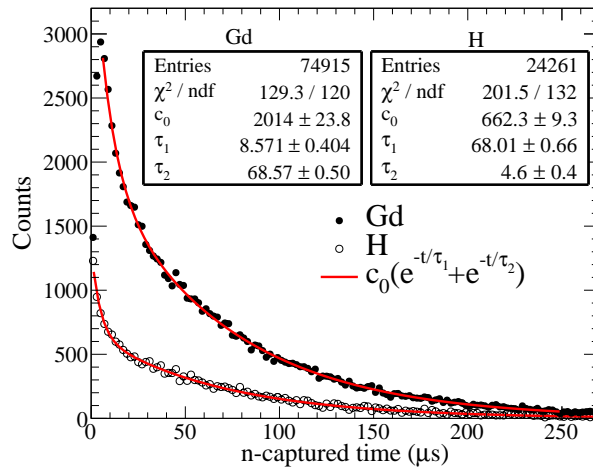


FIGURE 3.12: ΔT between prompt and delay event from simulation in ISMRAN geometry for the two dominant capture elements Gd and H.

distribution between the prompt positron annihilation event and γ -ray(s) from neutron capture either on H or Gd. The neutron capture time distributions are fitted with a double exponential function to obtain the mean neutron capture time of $\sim 68 \mu\text{s}$ in ISMRAN setup.

The capture of neutron and subsequent de-excitation differs between smaller nuclei like H and heavier ones, especially, Gd. Obtaining the capture event's sum energy and N_{bars} distribution is useful to know the ISMRAN delayed neutron event signature. As already discussed, neutron capture on Gd will give cascades of γ -rays adding up to about 8 MeV. On the contrary, captures on H will result in a mono-energetic γ -ray of energy 2.2 MeV. Figure 3.13(a) shows these distributions with the 0.2 MeV threshold applied on each bar and in the ISMRAN detector geometry. An intense ~ 2.0 MeV peak is observed in the sum energy distribution

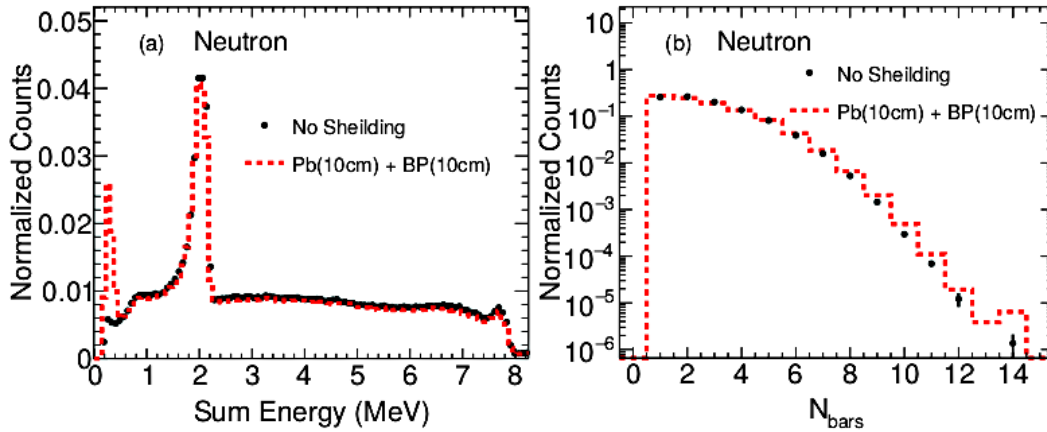


FIGURE 3.13: Sum energy (left) and N_{bars} (right) distributions for delayed neutron event in ISMRAN geometry with and without shielding.

due to the capture of neutrons on H nuclei. The H-capture γ -ray being a single emission and at relatively low energy is seen to be contained within the 10×10 ISMRAN setup. While the deficit of 0.2 MeV energy from expectation points at

removal of low energy γ -ray scatters due to threshold. Beyond this 2 MeV peak a continuum feature is seen in the sum energy distribution due to the incomplete containment of γ -ray cascades of Gd-capture events in ISMRAN. A suppressed Gaussian edge feature just before 8 MeV may be attributed to the ‘final state’ de-excitation method adopted which has high probability of single high energy γ -ray emission. Figure 3.13(b) shows the event by event distribution of N_{bars} from the neutron capture events in ISMRAN. The distributions in this study are chosen for the ‘No shielding’ and ‘Fully shielded’ setup, so as to bring out the effect of shielding when high energy γ -rays produced inside the detector volume interact with the shielding. A systematic reduction in events in the entire energy range is observed in the shielding case, more so around the H-capture and Gd-capture energies. A low energy peak is visible at ~ 0.3 MeV in the sum energy distribution, as seen in the histogram for full shielding (dashed histogram) in figure 3.13(a), corresponding to these capture γ -ray events, since they escape the scintillator volume and undergo Compton back-scattering from the shielding material (Pb (10 cm) + BP (10 cm)) and enter back in the sensitive volume of the detector. The effect of shielding is also visible in the N_{bars} distribution where the back-scattering produces more higher bar number events as seen in figure 3.13(b). The geometrical acceptance of the detector which is reflected in the incomplete containment of cascade γ -rays is also studied in simulation for the mini-ISMARAN (4×4) setup. Figure 3.14(a) shows the effect of the limited volume of the prototype mini-ISMARAN detector on the delayed neutron sum energy distribution and Figure 3.14(b) shows the N_{bars} distribution of the neutron capture events. The sum energy distribution in mini-ISMARAN is shifted to lower energy, around 1 MeV, as compared to the full ISMRAN setup. This is due to the partial

containment of the cascade γ -rays in the mini-ISMRAN. This effect can also be seen in the N_{bars} distribution in both the cases. Also, the 0.3 MeV feature has been verified to be present in the mini-ISMRAN geometry also. Prompt event doesn't suffer from energy containment issue as majority of the energy is in the form of positron dE/dx loss. Also, γ -rays from positron annihilation being low energy lose almost all energy inside the miniISMRAN volume.

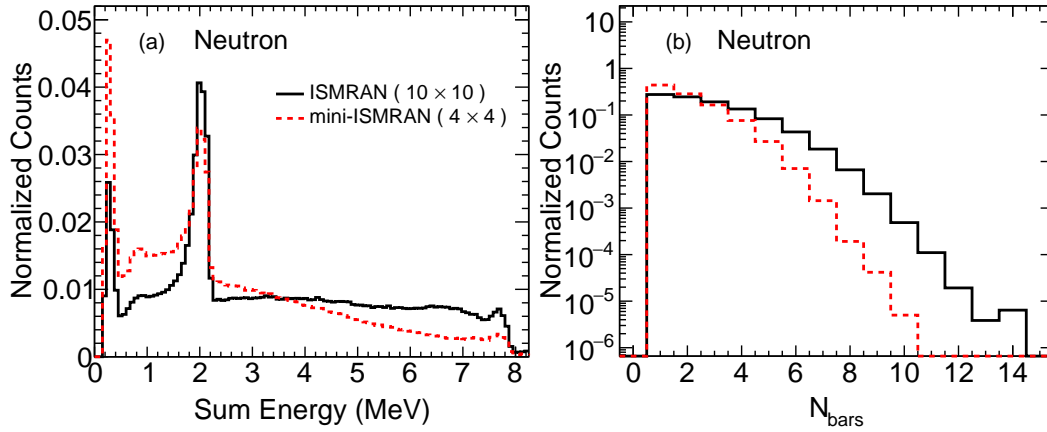


FIGURE 3.14: Comparison of sum energy (left) and N_{bars} (right) distributions for delayed neutron event in ISMRAN and mini-ISMRAN geometries.

3.3 Detection efficiency for pure IBD events in ISMRAN

Evaluation of the $\bar{\nu}_e$ detection efficiency in a pure IBD event data set involves identifying the prompt and delayed event using the sum energy and N_{bars} variable. The presented values of efficiency in this study is without the consideration of background in the simulation. It has been observed in the background measure-

ments, that the cosmogenic and reactor specific activities, especially the reactor γ -rays are dominant below the energy of 2 MeV (energies are shifted below due to Compton scatterings and resolution effect). To make use of this fact, the cut on E^{prompt} is started from 1.8 MeV which is a cut chosen to select most signal events possible while being at risk of introducing known backgrounds and hence lower purity. A higher cut of 2.2 MeV is expected to remove almost all known backgrounds, especially the H capture events, allowing for higher purity but at the same time sacrificing the left tail events of the prompt energy distribution. For the E^{delayed} i.e. neutron signal, again two cuts are evaluated with sum energy selection starting from 0.8 and 3.0 MeV respectively.

Although the 0.8 MeV cut is expected to introduce a lot of background but the requirement of higher value of $N_{\text{bars}}^{\text{delayed}}$ is expected to reject most uncorrelated background. The cosmogenic activity, predominantly due to the cosmic muons can be removed by the veto shielding, and also by their energy and tracking (straight) signature. In terms of energy, cosmic muon events deposit energies around 20 MeV (MIP loss) which is anyways removed by the upper threshold of 8.0 MeV in energy selection. This cut is representative of the fact that antineutrino spectra doesn't have enough statistics beyond this energy. Any low energy activity introduced by the cosmic muon interactions in shielding and metallic structures is also removed within $250\mu\text{s}$ window using timestamp information.

The $\bar{\nu}_e$ detection efficiency in ISMRAN are presented using the two sets of selections on sum energy, N_{bars} and mean time delay are summarized in Table 3.3. The two selections are named 'loose (Selection 1)' and 'tight (Selection 2)' signifying whether the above criteria are relaxed or stringent respectively. The cuts on sum energies : E^{prompt} and E^{delayed} and PS bar hits : $N_{\text{bars}}^{\text{prompt}}$ and $N_{\text{bars}}^{\text{delayed}}$ are

3.3. DETECTION EFFICIENCY FOR PURE IBD EVENTS IN ISMRAN 159

TABLE 3.3: Detection efficiencies of $\bar{\nu}_e$ events in ISMRAN with different prompt and delayed event selections.

Selection 1	Efficiency (%)	Selection 2	Efficiency (%)
$1.8 < E^{\text{prompt}}(\text{MeV}) < 8.0$	98	$2.2 < E^{\text{prompt}}(\text{MeV}) < 8.0$	96
$1.8 < E^{\text{prompt}}(\text{MeV}) < 8.0,$ $1 < N_{\text{bars}}^{\text{prompt}} < 4$	69	$2.2 < E^{\text{prompt}}(\text{MeV}) < 8.0,$ $1 < N_{\text{bars}}^{\text{prompt}} < 4$	67
$0.8 < E^{\text{delayed}}(\text{MeV}) < 8.0$	84	$3.0 < E^{\text{delayed}}(\text{MeV}) < 8.0$	56
$0.8 < E^{\text{delayed}}(\text{MeV}) < 8.0,$ $N_{\text{bars}}^{\text{delayed}} > 3$	29	$3.0 < E^{\text{delayed}}(\text{MeV}) < 8.0,$ $N_{\text{bars}}^{\text{delayed}} > 3$	27
$1.8 < E^{\text{prompt}}(\text{MeV}) < 8.0,$ $1 < N_{\text{bars}}^{\text{prompt}} < 4$ $0.8 < E^{\text{delayed}}(\text{MeV}) < 8.0,$ $N_{\text{bars}}^{\text{delayed}} > 3$	20	$2.2 < E^{\text{prompt}}(\text{MeV}) < 8.0,$ $1 < N_{\text{bars}}^{\text{prompt}} < 4$ $3.0 < E^{\text{delayed}}(\text{MeV}) < 8.0,$ $N_{\text{bars}}^{\text{delayed}} > 3$	18
$1.8 < E^{\text{prompt}}(\text{MeV}) < 8.0,$ $1 < N_{\text{bars}}^{\text{prompt}} < 4$ $0.8 < E^{\text{delayed}}(\text{MeV}) < 8.0,$ $N_{\text{bars}}^{\text{delayed}} > 3$ $4.0 < \Delta T(\mu\text{s}) < 200.0$	19	$2.2 < E^{\text{prompt}}(\text{MeV}) < 8.0,$ $1 < N_{\text{bars}}^{\text{prompt}} < 4$ $3.0 < E^{\text{delayed}}(\text{MeV}) < 8.0,$ $N_{\text{bars}}^{\text{delayed}} > 3$ $8.0 < \Delta T(\mu\text{s}) < 200.0$	16

listed along with the efficiency values for these events. A final selection cut, on the time difference (ΔT) between prompt and delayed events, is then made. This helps to further reduce the correlated backgrounds with their origin in cosmic or reactor activity.

The successive application of cuts on sum energies and then the N_{bars} variables reduces the overall efficiency significantly, as this method treats each variable as independent sets and takes their intersection. The only factor effectively classifying prompt and delayed events is the N_{bars} variable which rejects a lot of signal events. One of the observations from the above table is that the gap between the efficiency values for ‘loose’ and ‘stringent’ cuts is not very wide. The efficiency turns ON gradually and doesn’t reach the maximum efficiency, till slightly above 3 MeV energy, beyond which it remains uniform. Thus events

with energy below this value need to be treated with energy dependent efficiency corrections in selection. An increase in the lower energy cut of prompt event is anticipated in the analysis presented for the miniISMARAN data, as the reactor and natural (prominently ^{208}Tl :2.614 MeV) background activity in the reactor don't decay completely till 2.2 MeV. An increase of the lower sum energy threshold to 2.6 MeV, is therefore done. This increase is expected to shift the efficiency turn ON even further to about 3.5 MeV. Future cuts to be introduced later, on topology and event profile are expected to be more dominant than this reduction.

3.3.1 Photon evaporation Vs Final state model

Another interesting point of consideration is the impact of using the photon evaporation (PE) model instead of the final state (FS) method of Gd de-excitation on the $\bar{\nu}_e$ detection efficiency. This study is worthwhile as the PE model in GEANT4 is expected to conserve the Q value of reaction and expected to approximate the efficiencies better for moderate sized geometries like ISMRAN. We again generate 10^6 IBD events, but this time turning ON the 'photon evaporation' model in GEANT4. Since the positron interaction is unaffected by this change, we ignore the prompt event distributions and focus on the changes in the delayed event variable distributions.

Figure 3.15 shows the comparison of the sum energy and N_{bars} distributions for the two models under consideration. The first noticeable difference is the emergence of an intermediate peak in between those due to the H and Gd captures in the sum energy distribution (panel (a)). The peak can be attributed to the dominance of medium energy (3–4 MeV) γ -rays in PE model as compared to the

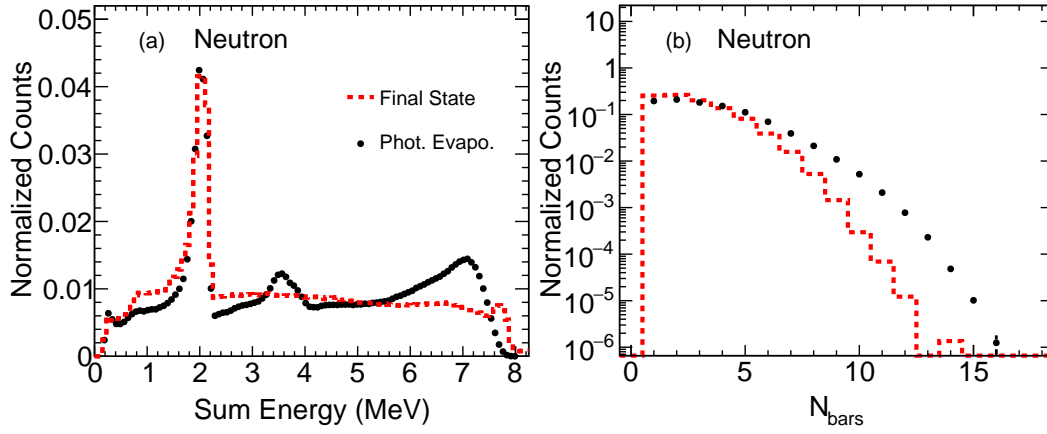


FIGURE 3.15: Sum energy (left) and N_{bars} (right) distributions for delayed neutron event in ISMRAN geometry for choice of final state and photon evaporation models of Gd de-excitation.

FS method. The important change is the increase in the number of reconstructed events closer to the expected Gd capture sum energy. The energies in PE model, are reconstructed below the ~ 8 MeV peak seen in the final state case, and the statistics in that region increases with lowered compton continuum. This reflects itself in more events falling inside the $3.0 < E^{\text{delayed}}(\text{MeV}) < 8.0$ cut and is expected to improve the efficiency. The H capture peak remains unchanged as it is a single γ -ray event.

To calculate the efficiency in this new data set, we impose the cuts as described in 3.3 and find out the final values in case of the stringent cuts. The efficiency is seen to improve to a value of 21%. The FS method basically generates on a random selection of γ -rays from the final spectrum of Gd isotopes. This approximation doesn't faithfully simulate captures on event by event basis and breaks the Q value. The PE model on other hand, presents a better option in this regard but its individual γ -ray spectrum is still not an accurate description of

the actual cascade event. Currently the simulation inputs in ISMRAN analysis use the events where PE model is used to simulate neutron capture. There have been recent studies of the radiative capture process of ^{155}Gd and ^{157}Gd isotopes [84], [85] which attempt at improving the description of their cascade γ -ray spectra. Inclusion of this improved modeling may lead to more realistic efficiency estimates.

3.4 Event embedding procedure

The efficiency values obtained from cuts applied in ISMRAN simulations are using only pure IBD events. The background is not known a priori and hence some of the selection cuts have to depend on educated guess for rejecting background. Additionally, these backgrounds vary non-linearly with reactor power and over the operation cycle. Meanwhile, miniISMRAN had been commissioned at the reactor site and has been acquiring the data in both reactor ON and OFF. In order to filter IBD like event in this dataset a simple application of above cuts simulated in ISMRAN geometry is not possible owing to its small volume and energy containment issue. Due to possibility of having many unknown background contributions and their unpredictable variations an ‘Embedded event technique’ for efficiency calculations is performed for miniISMRAN data.

This technique basically takes a reasonable number of pure IBD events (prompt and delayed event pairs) from monte-carlo (MC) simulations in miniISMRAN geometry i.e. the PS bar IDs, their energy deposits and internal timestamps, and randomly insert them inside the real data set while maintaining the mean time delay between the prompt and delayed event. Here we assume

that due to the negligibly small number of expected signal events as compared to the background, the real events in the data, at the raw level i.e. using only sum energy and N_{bars} cuts, can be considered to be entirely due to background.

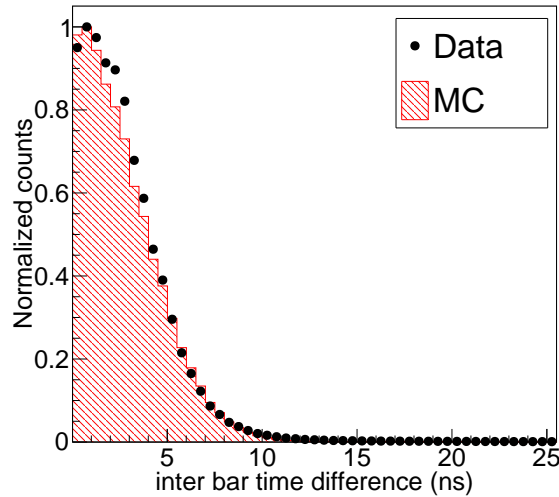


FIGURE 3.16: Timestamp differences of PS bars for whole dataset compared between simulation and miniISMARAN data.

The simulated events need to conform with the prompt delay dataset generated from the reactor data, for embedding to work in a realistic manner. To accomplish this, firstly, the bar energy values in the MC dataset are smeared using the obtained energy resolution function for the ISMRAN PS bars. Secondly, the MC events need to be assigned a realistic timestamp value as done by the digitizer in real data. This is crucial as the embedded events need to be presented to the data analysis flow as any other event from real data. These realistic timestamp values are derived from the raw event data (before prompt or delay classification) and then smeared within 1 microsecond range around this value to avoid replication. Also the at the individual bar level, the data has timestamps all sorted in ascending

order of time (as expected) so that the inter-bar time differences are all positive. These timestamps in the raw data have a Gaussian distribution. The σ of this Gaussian is used to smear the timestamps at the bar level in MC data. The data vs MC comparison after transforming the simulated event timestamps is shown in the figure 3.16. The matching signifies that the MC events now mimic the timing characteristics faithfully and can be introduced in the data sample for analysis.

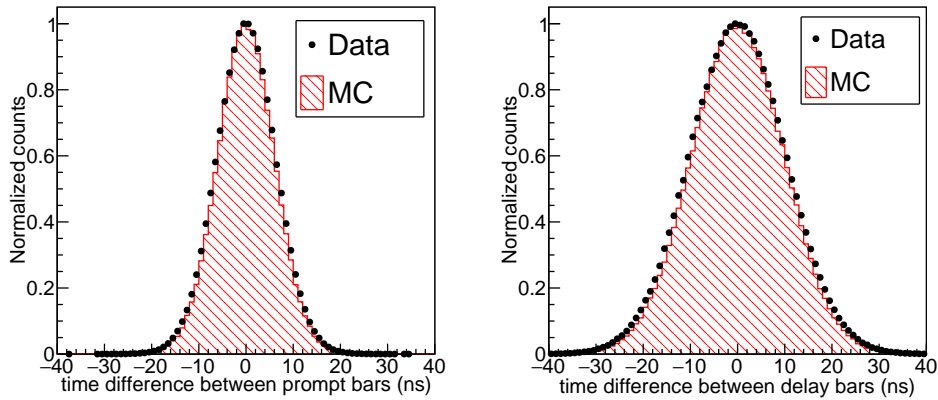


FIGURE 3.17: Time difference for different PS bars of an event compared between simulation and miniISM-RAN data for prompt(left) and delayed(right) events.

It must be pointed out that the MC prompt delay event ΔT_{PD} are unaltered in the above process. Another variable tagging the event as ‘MC’ is also added to the embedded events for user reference.

A lot of the comparisons presented here are in terms of the prompt and delayed events separately, as the simulated events are in the form of such pairs. The data events are grouped as either prompt or delayed using only the two base variables and the distributions are then compared with MC. The individual event timestamp differences among different bars in these prompt or delayed events obtained from simulation are compared with the data, as shown in the figure 3.17. The matching

confirms that timestamps selected when forming prompt and delayed events in MC get distributed identically as the data. Next step is to verify the Z position differences among the bars. ΔT_{LR} mean value in data is in turn translated to Z position through a polynomial function. But in MC, it is directly available as the energy weighted mean position of the bar hits. The comparison of the differences in the Z values of bars in an event is seen in Fig 3.18 which shows good match between the overlaid prompt and delayed event from data and MC.

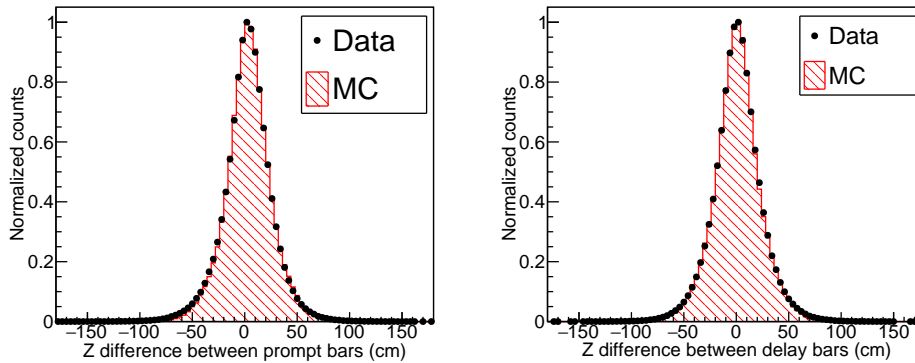


FIGURE 3.18: Difference of Z values of bars in an event compared between simulation and miniISMURAN data for prompt (left) and delayed (right) events.

The discrepancies due to background can be compensated to a great extent when a ratio of the energies is taken for a crude assumption that background behaves uniformly. Thus a ratio bar energies in an event can be a useful discriminating factor. The Fig 3.19) shows the ratio $- E_1/E_{\max}$ of 2nd highest to the highest energies among the hits forming an event and compared for MC and real data. For lower ratios in both the prompt and delayed events the data and MC ratios match. At higher ratios the background dominates. For delayed events there is an almost perfect match and is helpful as the ratio cut fro delayed events

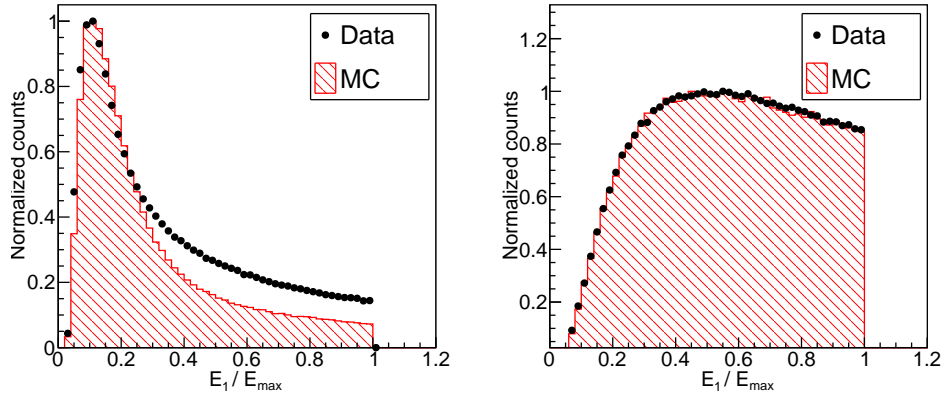


FIGURE 3.19: E_1/E_{\max} ratio of prompt(left) and delayed (right) events compared between simulation and miniISMRAN data.

is part of the criteria for event selection.

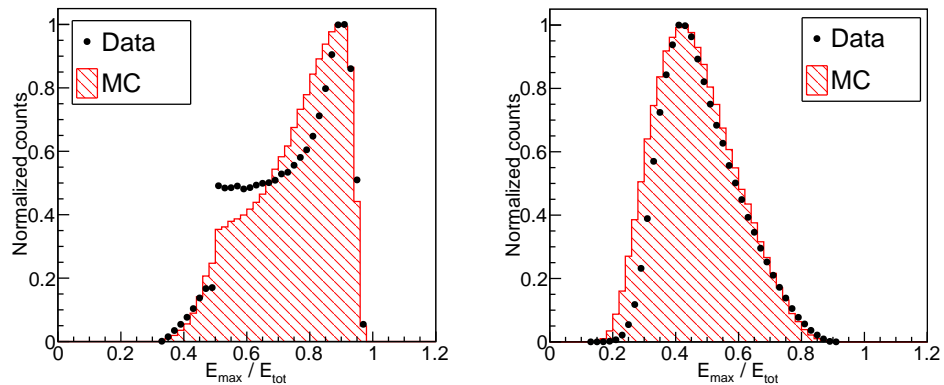


FIGURE 3.20: E_{\max}/E_{tot} ratio of prompt(left) and delayed (right) events compared between simulation and miniISMRAN data.

The maximum to total energy ratio – E_{\max}/E_{tot} , is another such ratio which reflects how well the MC mimics the data. This variable highlights the energy sharing characteristic of the event, with prompt event expected to deposit more in the first hit while the delayed events has a distributed pattern in energy sharing

among the bars. In both the cases, as seen in the figure 3.20, the data and MC match and agree on the expected energy sharing dynamic in the event. Finally

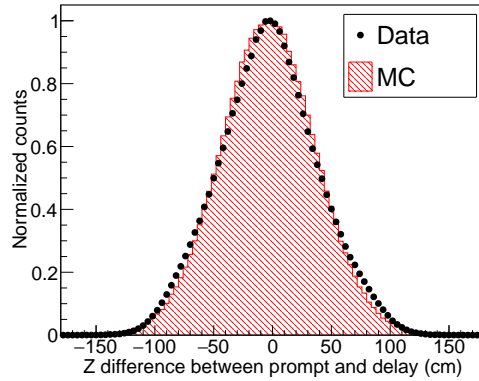


FIGURE 3.21: Difference in Z position of prompt delay pairs in simulation and miniISM-RAN data.

the topology of the prompt-delay pair in terms of the Z position is compared in data and MC as shown in the figure 3.21. The X-Y separation criteria is implicit in the N_{bars} cut but the Z difference is also needed to be checked for an IBD event. The events can span in the full Z-length of 100 cm but most of the events are concentrated within a distance of 50 cm, which is also seen from the monte carlo.

The next step is to apply all the selection criteria of ISMRAN cut based analysis on this event embedded data and observe how the event selection efficiency is impacted progressively and to obtain its final value for miniISM-RAN matrix. In order to avoid any over-estimation or under-estimation of efficiency only 25 events are embedded in a successive windows of 1 minute in reactor data. A prompt-delay pair can be formed with the MC events embedded in data in four ways 1) MC-MC where both the prompt and delayed events of MC get selected

TABLE 3.4: Selection cuts and corresponding event efficiencies from embedded data set.

Cuts	Efficiency(%)
Raw (Only sum energy and N_{bars})	74.25
Muon rejection	55.80
$\Delta Z_{\text{PD}} < 1 \sigma$	54.29
Prompt in contiguous bar	35.92
$(\Delta T_{\text{LR}})_{\text{prompt}} < 8.0\text{ns}$	35.52
Only one bar energy $> 5.5 \text{ MeV}$	27.88
$(E_1/E_{\text{max}})_{\text{prompt}} < 0.5$	27.62
$(\Delta T_{\text{bars}})_{\text{prompt}} < 1.5\sigma$	25.19
$(\Delta Z_{\text{bars}})_{\text{prompt}} < 1.5\sigma$	21.14
$E_{\text{max}}@T = 0$ or the first	21.12
$(\Delta T_{\text{LR}})_{\text{delay}} < 8.0\text{ns}$	19.69
Central bar required	18.12
$(E_1/E_{\text{max}})_{\text{delay}} < 0.5$	13.16
$(N_{\text{bars}})_{\text{delay}} 4$ to 7	12.82
Delay in contiguous bars	5.44
$(\Delta T_{\text{bars}})_{\text{delay}} < 1.5\sigma$	4.54
$(\Delta Z_{\text{bars}})_{\text{delay}} < 1.5\sigma$	3.94

by the cuts as the IBD pair 2) MC-Data where the prompt is from MC while delayed is from data 3) Data-MC where the prompt is from data and delayed is from MC and 4) Data-Data which is the usual case without embedding. Only the events where a MC–MC pair is filtered are counted for efficiency. The table 3.4 gives the event rates as the sequence of cuts are applied in the analysis with the embedded MC events as part of the data.

The events where double-prompt, double-delay pairs are formed and events which fall inside a muon veto window of $250 \mu\text{s}$ are first screened out. Also, only events where the neutron is captured by Gd are considered. Consequent addition of localization cuts in time and Z position reduce the efficiency to half. Further cuts on intra bar timings and energy thresholds are then introduced and we see a drastic reduction in efficiency. The final value comes out to be a meagre 3.94%

which is expected for miniISMARAN. Such an evaluation of the miniISMARAN data hints at the fact that the ISMRAN matrix with its scaled up volume has a better prospect for IBD event detection . However, the background quantification and analysis procedure can be established at the level of miniISMARAN which is useful.

3.5 Cosmic muon and neutron backgrounds

Cosmic background radiations like muons and neutrons are omnipresent and many of these particles are very penetrating due to their high energies. These muons and neutrons are a product of, high energy charge particle (mostly protons) collisions with the nuclei of gas molecules in upper atmosphere to produce shower of secondary particles. For an above ground setup like ISMRAN, the flux of these particles can pose a serious challenge, due to the modest overburden (~ 2 m.w.e) of concrete wall in the reactor hall. Based on the MIP energy loss in the single ISMRAN PS bar, 6 Hz of activity is observed without any shielding, due to the cosmic muons obtained by choosing high energy (mostly vertical) events beyond 15 MeV. Scaling this muon activity to the ISMRAN volume, about $\sim 10^6$ muon events are expected in a day. The veto shielding is expected to tag their presence, but their straight and long tracks coupled with high losses due to their passage from the thick bars in a segmented geometry will allow for a better identification. More than the muons, its their interactions with high density materials like Pb in shielding which can be harmful for ISMRAN. These high energy muons can undergo spallation in the Pb shielding and produce correlated shower of neutrons, which can mimic the prompt delay event due to two captures happening with a

time gap. A standard technique to reject such events is to introduce dead time in acquisition when muon events are encountered, usually around the veto signal. For ISMRAN, the acquisition is not planned to be interrupted and the veto signal will rather act as an additional flag in data for filtering muons and their associated low energy activity, later in analysis. After recording the raw stack data and forming the prompt and delay events using the first level sum energy and N_{bars} information, all events formed within a window of $250 \mu\text{s}$ on both sides of tagged high energy bar event is used to remove any of the aforementioned activity. It must be pointed out that this selection is inefficient in rejecting those muon events where there is partial or lower energy losses. The fraction of such events passing the prompt and delay selection in ISMRAN is only at a few percent level, and is estimated in the discussion that follows. In the mini-ISMARAN, a scintillator veto assembly is missing and the muon identification is only based on energy which rejects bar events beyond 8 MeV deposit, the expected rate of such events is less than 10 Hz in each bar, as observed from mini-ISMARAN operation in non-reactor (lab) environment. This leads to a maximum cumulative rate of 160 Hz in the 4×4 setup which is lower than the RON background rate.

In case of cosmogenic neutrons reaching sea level, we saw earlier that for beyond few MeV energies and up to GeVs they can't be stopped and are likely to again cause a correlated shower through deep inelastic interactions in shielding or metallic structures in ISMRAN setup. Rejecting outside neutrons is the most challenging task as they have no electromagnetic interactions and can easily mimic the delayed or even the prompt event once they thermalize and get captured, since the ultimate signature of IBD is considered due to the γ -rays only. The relatively low and falling nature of sea level cosmic neutron flux [82] is less

of a background than muons, but still necessary to be studied in terms of their signature in ISMRAN.

A cosmic ray shower generator ‘CRY’ is available for simulating such cosmic particles at different altitudes and different detector sizes [86]. When simulating using this package, all the particles including muons, neutrons, γ -rays and electrons are returned in the detector box which was selected as per ISMRAN size. But, in analysis only the muons and neutrons are selected for their event signatures. A sample of $\sim 10^6$ events are generated in this box size. In this shower about $\sim 2.8 \times 10^5$ muons are returned out of which about $\sim 6.5 \times 10^4$ ($\sim 23\%$ of incident flux) penetrate the shielding. The typical energies deposited in a single ISMRAN PS bar is as shown in the figure 3.22.

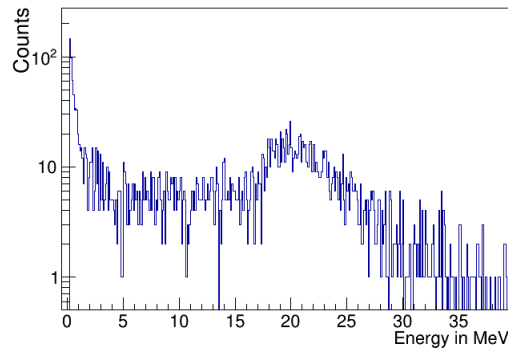


FIGURE 3.22: Typical energy spectrum recorded for CRY generated cosmic muon event in ISMRAN PS bar.

These muons and their secondary activity is then recorded in the whole volume on an event by event basis. The same sum energy and N_{bars} variables are derived for each event and plotted in the figure 3.23. The energy signature shows a wide range covering the whole 40 MeV scale, with the expected landau distribution having MPV at 20 MeV (MIP loss: $2\text{MeV g}^{-1} \text{cm}^{-3}$). The sum

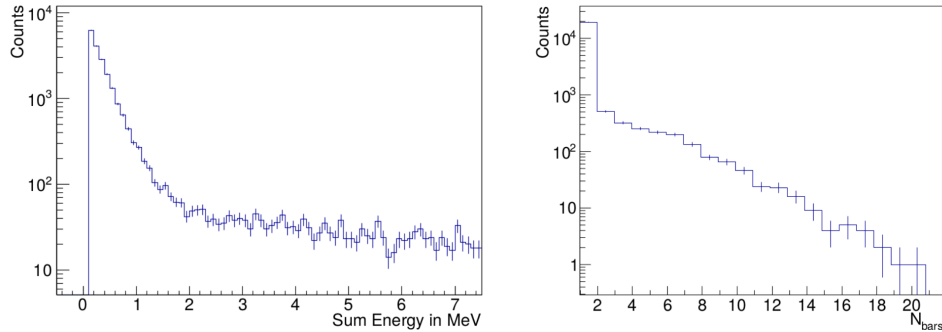


FIGURE 3.23: The sum energy (left) and N_{bars} (right) for the cosmogenic muon event in ISMRAN.

energy signature shows a high fraction of events in the low energy region where the selection cuts are supposed to reject the event. But there is a bed of cosmic muon events spanning 2 to 7.5 MeV range in sum energy at about 1% level of the total incident and penetrating flux. The N_{bars} signature shows a falling trend with most penetrating muons spanning lesser bars which is a good sign as the $N_{\text{bars}} > 1$ condition can remove most of them.

A similar approach for the cosmic neutron events in ISMRAN is taken with neutron events evaluated for signal like behaviour inside the detector volume. Out of the total shower particle count only 2% neutron events are incident on the ISMRAN detector. The number of neutrons incident on ISMRAN are about $\sim 2 \times 10^4$ of which $\sim 1.2 \times 10^4$ neutrons penetrated the shield which is about 1% of the total shower particles generated. The typical energies recorded due to these neutrons in a single PS bar is as shown in figure 3.24. The larger counts at energies less than 10 MeV is a problem as it overlaps with the IBD energy region of interest.

Figure 3.25 shows the recorded sum energy and N_{bars} distributions for the

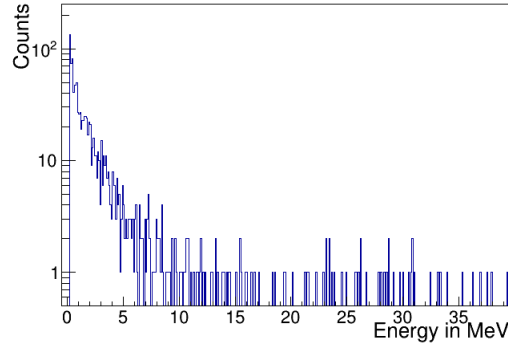


FIGURE 3.24: Typical energy spectrum recorded for CRY generated cosmic neutron event in ISMRAN PS bar.

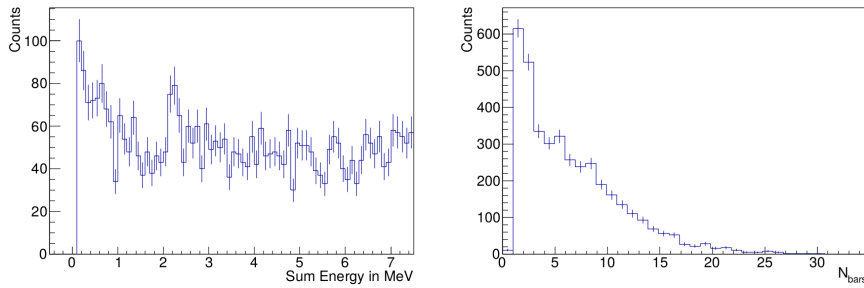


FIGURE 3.25: The sum energy (left) and N_{bars} (right) for the cosmogenic neutron events in ISMRAN..

neutron events. Observing these distributions shows almost a similar behaviour as the muon signals. The sum energy signature is uniformly distributed over the whole IBD region. Major fraction of neutron events lie in the $N_{\text{bars}} < 3$ region and can be easily removed in the cut for delayed events. To mitigate the contamination of cosmic muon and neutron activity, introducing additional selection criteria on single bar energies and event profile in cut based analysis and/or introducing event classification using multivariate analysis methods can be adopted, and will be discussed in coming chapters.

3.6 Summary

The ISMRAN detection setup including the Pb and BP shielding is simulated in GEANT4. Shielding effectiveness is first tested for a range of γ -ray and neutron energies. The neutron penetration is quite high as compared to γ -rays at high energies. Pure IBD events are simulated inside ISMRAN geometry using the precision packages available in GEANT4. A realistic $\bar{\nu}_e$ spectrum is used as input to derive the daughter positron and neutron products of IBD.

The simulated events are found to be useful in understanding the sum energy and N_{bars} or ‘number of bar hit’ distributions for prompt positron and delayed neutron events which in turn define the $\bar{\nu}_e$ event inside ISMRAN. The mean time delay value between such pairs is extracted and found to be $\sim 68\mu\text{s}$. Using this knowledge, appropriate cuts are designed excluding known background energy regions and a value of $\sim 16\%$ using the final state model and 21% in the photon evaporation model for Gd cascade is obtained.

The small volume of the miniISMRAN doesn’t allow the above simple analysis due to effects of incompletely contained γ -rays being more pronounced. Thus an embedding of simulated IBD events into the recorded miniISMRAN data is done and cut based analysis is performed to evaluate miniISMRAN efficiency. A modest value of $\sim 4\%$ IBD detection efficiency for the prototype is obtained from this embedded event analysis. Finally the characteristic signatures for cosmogenic muon and neutron activity are studied for the ISMRAN geometry using CRY cosmic ray generation package.

Chapter 4

Machine learning framework for ISMРАН

4.1 Choice of analysis technique

The cuts chosen to select prompt and delayed signal components of the IBD event results in a modest detection efficiency of 21% even in the best case scenario. These set of cuts are motivated by the requirement to have prompt and delayed events exclusive of each other and to reject most of the low and high energy activity surrounding the energy region of interest. This allows for higher purity in $\bar{\nu}_e$ detection. The ‘cuts’ approach essentially treats the variables independently or in a univariate manner and hence suffer from large inefficiency

due to the overlap between the sum energy and N_{bars} (see figure 4.1) for both prompt and delayed events. More advanced methods from ‘Multivariate analysis’ (MVA) can offer better performance in the presence of variable correlations e.g. the artificial neural networks (ANN) using ‘Machine learning’ (ML) algorithms. Such techniques can be explored for ISMRAN event classification to improve $\bar{\nu}_e$ detection efficiency and purity.

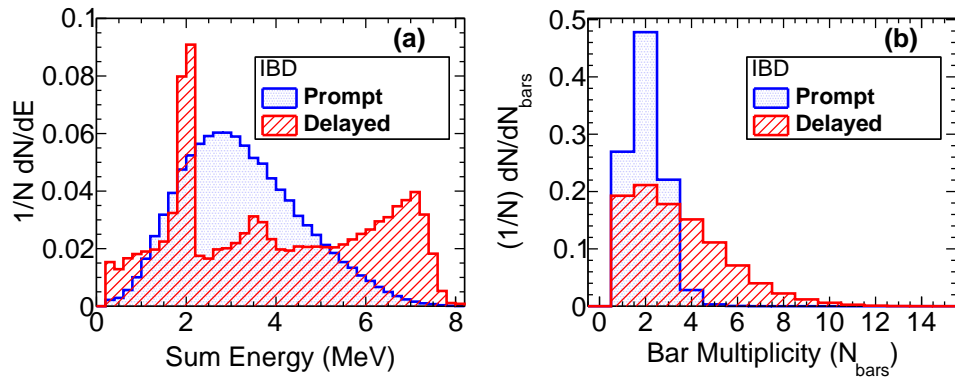


FIGURE 4.1: Simulated Sum Energy (panel (a)) and N_{bars} distributions (panel (b)) for prompt and delayed events in ISMRAN showing overlap at the threshold level cuts.

4.2 Multivariate analysis and Machine learning

The MVA techniques are particularly useful in the context of high energy physics (HEP) where multiple, possibly correlated, variables define a single event. These variables can be the energy depositions and timings in different detector segments, kinematical quantities of interaction products, angular spread and track information etc. Classification of events into signal and background components based

4.3. *ARTIFICIAL NEURAL NETWORKS AND MULTI-LAYER PERCEPTRON*

on some prior knowledge(theory) makes up most of such analysis problems. In some cases, ordination (ordering of variables) and clustering (grouping events without prior labels) may also be required. In terms of the their framework, these methods can range from purely multivariate statistics approaches to ML based methods, with the latter gaining increasing importance in recent times.

ML can make use of a combination of statistics, algorithms and optimization techniques to establish its learning process. In mathematical terms, its similar to fitting input data with complex functions [87]. Once the system has been characterized, the same model is used to predict new data points and infer properties of similar systems. The learning process in ML can be supervised, un-supervised or reinforcement type learning. Out of these the supervised learning is more commonly encountered in data analysis. This process trains the machine using data set with known class labels. Here the process essentially involves minimizing error (difference from known output) in machine response over multiple iterations.

4.3 Artificial Neural Networks and Multi-Layer Perceptron

ANN is an MVA candidate of the non-linear discriminant family and uses the supervised ML technique for its training. Most ANNs have a layered structure, as shown in the figure 4.2, with a layer for accepting the inputs (x_1, x_2, \dots, x_D) and a layer for producing the outputs (y_1, y_2, \dots, y_K) and one or more hidden layers (z_1, z_2, \dots, z_M). This is the so called 'feed-forward network' (FFN), wherein

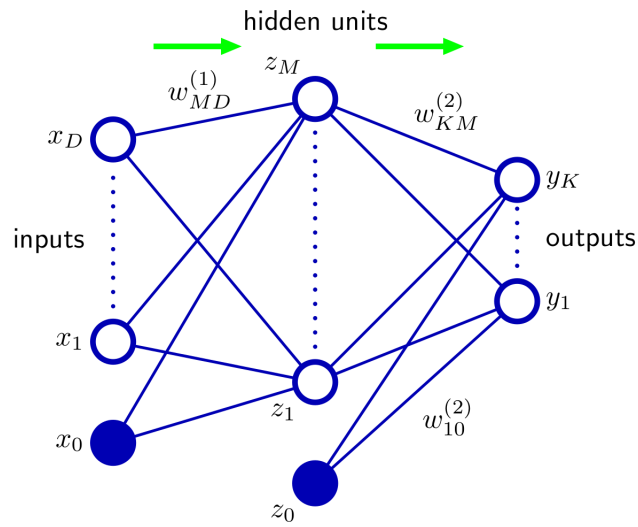


FIGURE 4.2: Simplest feed-forward neural network [88].

the information travels only in the forward direction from input layer to output layer. Such a simplistic ANN is popularly called the ‘Multi-Layer Perceptron’ or ‘MLP’ [88, 89, 90]. MLPs in a single hidden layer configuration are considered ‘universal function approximators’, a term signifying their ability to approximate any function with arbitrary precision given sufficient number of neurons [91, 92]. Main constituents of an MLP are as follows:

Neurons: These are the artificial counterparts of the neurons in human brain. These are computing nodes which decide the network’s mathematical response function. The input of a neuron are either the characteristic variables describing the sample dataset or outputs of other neurons. FFNs arrange the neurons in *layers* and route neuron outputs from one layer to next but never in the same or previous layer. The last layer of output neurons performs the classification/regression function. The output of a neuron, is a weighted sum of all the input connections to the neuron. A bias term denoted by the ‘0’ subscript is also added to this sum.

4.3. ARTIFICIAL NEURAL NETWORKS AND MULTI-LAYER PERCEPTRON

The weighted sum is usually operated upon by a non-linear *activation function* like a tanh or sigmoid to produce the output.

Connections: These are the links between neurons in the ANN similar to the synapses join the biological neurons. Connections are assigned weights “ w ” to denote its relative importance. A neuron can have more than one input and output connections.

The supervised learning method used in the ANN classifier can be summarized in the flow chart shown in figure 4.3. The inputs and corresponding output (class label) pairs are known for a data set called the ‘training data’. This data is fed to the the neural network. The process of learning in a MLP basically happens in the form of adjustment of weights of the connections. Accuracy of response is improved by iterative training till the the network response error is minimized. The evaluation of error is done parallel to the training process using a ‘cost function’ and evaluated periodically during learning. The nature of this

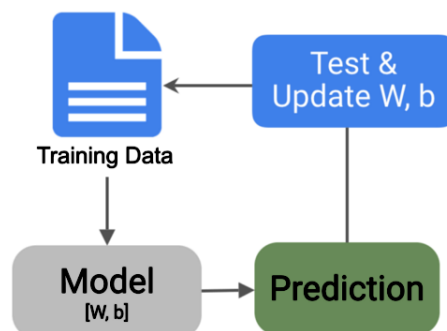


FIGURE 4.3: Flow of supervised learning mechanism using weights ‘W’ and biases ‘b’ in Machine learning. [93].

function can be adhoc or based on posterior probability. Mean-squared error is a

common cost-function which tries to minimize the average squared error between the expected and produced network response. The learning rate is decided by the size of the corrective steps taking place in each iteration. Higher learning rate reduces training time but also worsens the achievable accuracy, and, the opposite takes place for slow learning.

Backpropagation (BP): The learning process for FFNs is implemented using the ‘back-propagation’ algorithm. This algorithm repeatedly computes the gradient of the cost-function in terms of the change in the weights of the network, starting from the last layer and iterating backwards. The technique called ‘gradient descent’ or the more popular ‘stochastic gradient descent’ which is the approximation of the former optimizes the BP algorithm’s performance by finding the optimal route to minimizing the cost (error) function.

Networks like MLP have been used for speech and image recognition and process control systems. But more advanced networks have since been invented for the above tasks. The Deep Neural Networks (DNNs) having more hidden layers and more neurons address highly complex and non-linear problems. The Convolutional Neural Networks (CNNs) are designed to be good at implementing a feature-aggregation logic commonly needed in image recognition. Finally, the Recurrent Neural Networks (RNNs) are designed for natural language processing with a distinct feature of using self connections and connections within the layer, which is not the case with others.

4.3. ARTIFICIAL NEURAL NETWORKS AND MULTI-LAYER PERCEPTRON

4.3.1 TMVA analysis package and its MLP

The ROOT MVA package – Toolkit for Multivariate Analysis (TMVA) [94] is a collection of C++ and ROOT (object-oriented) implementations of MVA techniques. It has the ability to evaluate multiple MVA techniques for the same inputs parallelly and provide a performance comparison and are designed to cater to the needs of high-energy physics (HEP) applications. TMVA–Graphical User Interface (GUI) code facilitates optimum user interaction with the output of any of its MVA method provided in terms of visualization and plotting etc. Some of the common MVA methods often opted by users include: MLP, Fisher’s discriminant [95], Support vector machine (SVM) [96] and Decision trees specifically the –Boosted decision trees [97]. In general, if a simpler method is sufficient to handle the MVA task at hand then it should be chosen over more complex ones. For example, a properly trained ANN with optimally designed architecture is expected to give better performance over a complex ‘Boosted Decision Tree’ method. A balance between the discrimination power offered, classification time and computing constraints needs to be achieved. If a user chooses a simpler method like a linear discriminant analysis (LDA), a prior de-correlation of variables is preferable. The non-linear methods like ANN, SVM, BDT are more appropriate for classification/regression problems with more variables.

TMVA MLP: The TMVA MLP structure and functions are the same as the FFN type. TMVA provides 4 implementations of neural networks, out of which the newly developed MLP implementation is chosen is for testing with the ISM-RAN events, as it is faster and more flexible than the older Clermont-Ferrand and ROOT’s TMLPANN implementations and simpler than the DNN which is spe-

cially designed for complex network designs on multi-core GPU architectures. The primary parameters required to be set for MLP operation in TMVA package are:

- **NCycles:** Number of training cycles. Default value is 500.
- **Hidden Layers:** This specifies the hidden layer architecture. Default setting is: two layers with 'N' neurons in first hidden layer and 'N-1' neurons in second hidden layer designated as N, N-1. Here N is the number of input variables nodes including one bias node.
- **NeuronType:** The choice of activation function. Default is Sigmoid ($\frac{1}{1+e^{-x}}$). But other functions such as hyperbolic tangent function is also available.
- **Training method:** Choice of algorithm for learning. Default is Back Propagation, but BFGS, GA are also available.
- **TestRate:** Decides the frequency of over-training test during training. Test for over-training performed at each nth epoch.

There are many other parameters which can be set but not advised to be changed from default as they are already optimized for best performance.

4.4 Event definitions in ISMRAN

The digitizer output in ISMRAN, provides the integrated charge, channel number, event-timestamp and real time data for each event. These events are recorded only when both end PMTs of a PS bar record signal within a coincidence window

of 16 ns. Offline reconstruction of events is performed by grouping of the PS bars (N_{bars}) hit according to the stored timestamps and obtaining the sum energy of the deposits by addition of the individual energy deposited in each PS bar. Following this, a classification of event as either prompt-like or delayed-like needs to be done for further assigning it as a $\bar{\nu}_e$ candidate event. After these two events are identified then in the next step the mean time delay selection is imposed to call an event as a $\bar{\nu}_e$ candidate or background. Therefore, the accuracy of classifying the prompt positron and delayed neutron signal decides the efficiency of $\bar{\nu}_e$ detection. Out of these two the prompt signal is especially important as the spectrum of such events is needed to derive the $\bar{\nu}_e$ energy spectrum. Thus the focus of our MVA classification will be to evaluate how efficiently and accurately a chosen classifier can identify the prompt events in data.

4.5 Multivariate classifier for ISMRAN

The available multi-variate classification algorithms in TMVA are tested for their efficient classification of IBD prompt positron events in the existing GEANT4 simulation setup for ISMRAN [98]. The photon evaporation model is chosen to simulate Gd de-excitation cascade in this setup. A simulated sample of 5 million IBD events are generated randomly throughout the volume of the ISMRAN. The thresholds of $E_{\text{bar}}^{\text{Th}} = 0.2 \text{ MeV}$ and $N_{\text{bars}} > 1$ are used in the reconstruction of prompt and delayed events. The sum energy variable for the deposited energies and N_{bars} variable or number of PS bar hits obtained from simulations under these thresholds are calculated and recorded in separate trees. These can be referred to as the base or primary variables which define the event at the raw data

level. The reconstructed prompt positron or “reco prompt” events are labeled as ‘signal’ events and any other γ -ray and neutron induced signals are each separately stored as ‘background’ event trees. To have a comparison of classification performance possible with the linear statistical classifiers vs the non-linear ones the ‘maximum likelihood method’ and the ‘Multi-Layer Perceptron’ are chosen because of their relative simplicity coupled with robust performance. There are no specific parameters needed to be set for TMVA likelihood implementation as it is a statistical process. However in case of MLP there are many operational choices that are either kept default or tuned to cater to ISMRAN event classification needs. Firstly, the basis of MLP functioning for ISMRAN is unaltered i.e. the Backpropagation algorithm is kept intact with use of stochastic gradient descent method. The chosen MLP architecture in our study uses two hidden layers. The first hidden layer uses $N+5$ neurons while the second one uses N neurons, where N corresponds to the number of input variables. An approximation to the hyperbolic tangent function is used as the activation function in each hidden layer neuron. One of the input node apart from the input variables is the bias node, which is implicit in the MLP architecture. One of the variables labeled $D_k 2.5$ will be introduced later. The two hidden layer configuration is found to have optimal performance for reasonable number of iterations in error minimization leading to less computational time. The network can be pictorially represented as shown in the figure 4.4. To reduce the number of iterations of training for cutting down on the computation time an alternative approach called the Broyden-Fletcher-Goldfarb-Shannon (BFGS) method can be utilized while adapting the synapse weights. This method uses the second derivatives of the error function for adjusting the weights in each iteration. The results presented

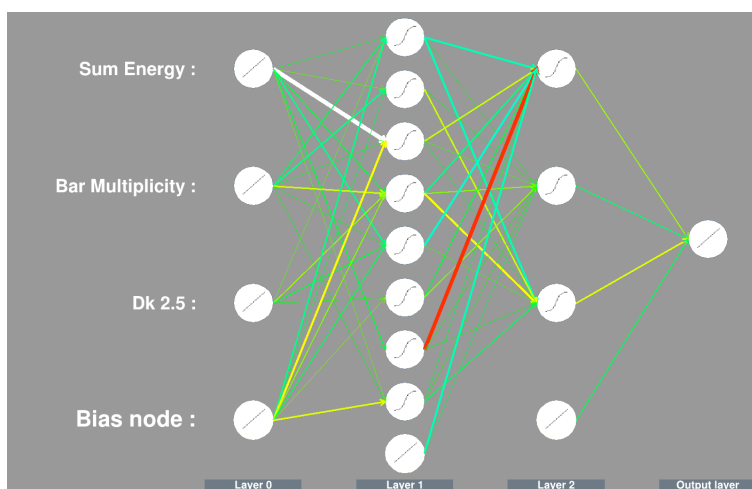


FIGURE 4.4: The two hidden layer MLP architecture for ISMRAN showing the neurons and their connections (synapses) color coded, with blue end representing weaker connection strength and red end depicting stronger connections.

here are for the classification using the ‘Bayesian’ extension of MLP with the above BFGS method incorporated in it, referred to as – ‘MLPBNN’ in the ROOT TMVA package. The MLPBNN approach allows for increasing the complexity (more hidden units and/or more layers) of the architecture while simultaneously employing a regulator to avoid over-training. This is achieved through addition of another term in the network error function that effectively penalizes large weights, consequently controlling the complexity of the model. For purposes of brevity in writing and also acknowledging the fact that MLPBNN is an extension of the more fundamental MLP algorithm, we will use only the term ‘MLP’ for the MLPBNN classifier here onward. Similar work adopting the convolution visual network a modified form of CNN, is used to classify neutrino interactions based on their topology [99].

To compare the relative performances of the maximum likelihood and MLP classifiers for separating prompt positron events from delayed neutron events, the

reconstructed neutron capture events from both Gd and H nuclei are chosen as backgrounds. The neutrons are observed to get captured $\sim 73\%$ of the times on Gd and $\sim 25\%$ of the times on H for the ISMRAN geometry. The Gd positioning is on the wrapping around the PS bar, while H is present in the bulk of the volume. The delayed neutron events can be interpreted as a prompt event due to the overlap discussed earlier in the event distributions. These events can be misidentified as the “reco prompt” events and hence called the “False prompt” events. To compare the discrimination power offered by these two classifier, or any classifier in general, the efficiency and purity of the classification offered are to be presented using an indicator which concisely and effectively conveys these performance parameters. The ‘Receiver Operator Characteristics’ – ROC curve of classifiers is one performance indicator targeting the above characteristics in a convenient graphical output format [100]. It uses a true positive (signal) vs false positive (background) ‘ratio’ based evaluation which makes it independent of the effects like class-skew i.e. imbalanced probabilities of true and false events and even unequal classification errors. In ROC terminology, the reco prompt represent the true positives while the false prompt are the false positives. The neutron capture events used in this classification are assumed to be due to the IBD neutrons only. In reality, ambient neutrons in the reactor hall also get captured in ISMRAN volume. The thermal/fast neutrons leaking from the guide tube and/or from the ports can thermalize in the shielding or in the volume and get captured on the Gd or H nuclei in the volume similar to the IBD neutrons. The statistics of such events occurring in ISMRAN is not yet quantified but their signature is expected to be similar when it comes to capture γ -rays. A total of 1000000 events are used for the classifier training and another 1000000 events are generated com-

pletely independent of the training dataset and used for testing and evaluation of the classifier performance. For the MLP classifier, some more details need to be specified which include the type of neurons, the number of hidden layers and training iterations and testing frequency. The ‘neuron type’ implies the activation function which in our case is the hyperbolic tan (approximation) function. The training is performed for 600 cycles and with a testing frequency of 1 testing cycle every 5 training cycles. Figure 4.5 shows the response curves for the maximum likelihood and MLP classifiers along with the reco prompt efficiency vs false prompt rejection curve – ROC for the two classifiers. The response graph for

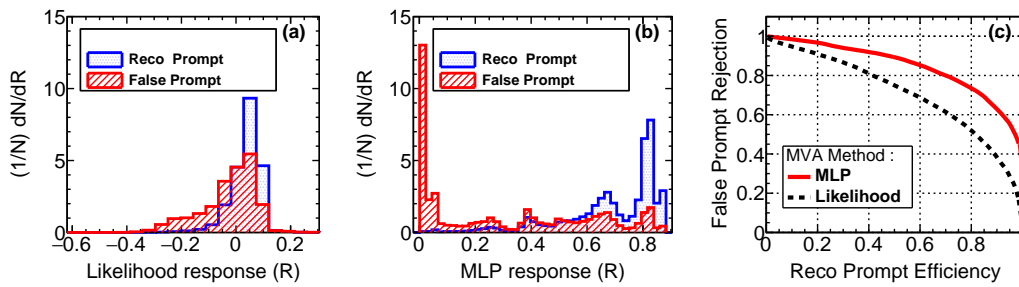


FIGURE 4.5: Panel (a) and (b) shows the comparison of performance for maximum likelihood and MLP classifiers on simulated IBD reco prompt and false prompt events in ISMRAN detector, respectively. Panel (c) shows the comparison of ROC curve for the MLP and maximum likelihood classifiers.

maximum likelihood classifier as seen in figure 4.5(a) again shows a substantial overlap between the reco prompt and false prompt not allowing for efficient classification. Panel (b) shows the MLP response which reflects an improved classification as there is less contamination of background. The ROC curve in panel (c) just re-confirms the above observation in an obvious sense by indicating higher efficiency of true positives or reco prompt identification compared to maximum likelihood with more than 25% more signal event selection for a

reasonable background rejection of 80%. This comparison evidently favours the MLP over Likelihood and provides more confidence in the choice of MLP classifier for ISMRAN event selection. The choice of a non-linear classifier also allows inclusion of more variable space due to lower threshold requirements which in turn contributes to the efficiency. This freedom was not available in case of cut based selection and it impacted the reconstructed $\bar{\nu}_e$ spectrum.

4.6 Results from reco prompt vs background classification with MLP

A number of different backgrounds can potentially hamper the prompt event reconstruction efficiency in ISMRAN event data. We have already seen that the neutron capture γ -rays can be misidentified as prompt signal. These captured neutrons can be from both IBD or any other reactor specific/cosmogenic sources. Apart from this the prominent backgrounds are the reactor hall γ -ray activity and the fast neutron scattering induced signals. These backgrounds are simulated in the ISMRAN geometry and MLP classifier is tested for discrimination power. The results of these classification exercises are discussed in this section. The cosmogenic backgrounds such as signals produced due to cosmic muons, neutrons or spallation neutrons from muon interactions in Pb shielding and also signals from long lived radioactive nuclei like ${}^9\text{Li}/{}^8\text{He}$ can mimic the correlated signature of prompt positron signal. These are not currently covered in this work, but, the muon and its induced activity is expected to be rejected by the use of veto shielding and by identifying the muon track in analysis. A $250\mu\text{s}$ dead time

is introduced in the data analysis whenever a muon track is detected and can remove the correlated activity of any spallation reaction products. Long-lived activity can be quantified in detail in future measurements.

Improvements in the MLP classifier

Capture of thermal neutrons on Gadolinium leads to formation of an excited compound nucleus which is followed by the subsequent emission of γ -ray cascades via de-excitation. The N_{bars} for such multiple γ -ray emissions is expected to be higher because of their number and energies involved. The sum energy of this event is expected to be near 8 MeV for both the Gd isotopes ^{155}Gd and ^{157}Gd when the complete event is contained inside the volume. From figure 4.5 (c) it is clear that a cut on the MLP response providing 90% signal selection can reject only 65% background or false prompt events, which is a substantial uncertainty. This relatively low background rejection performance can most possibly be due to the lack of discriminating power in the input variables before MLP model is introduced, and, it needs to be addressed. A hint can be taken from the particle collider experiments where the quark and gluon jet identification is to be performed in high energy proton-proton collisions [101]. Energy deposits and multiplicity of hits are often encountered in such collider data analysis. A common practice is to use energy/momentum weighted variables. On similar lines, we devise a new variable using both sum energy and individual bar energies with appropriate weights. The new variable is called ‘ D_k ’ and is formulated as $D_k = E_{\text{total}}^{-k} \times (\sum_i (w_i \times E_i^k))$, where E_{total} is the total sum energy, E_i is an individual energy deposit in a PS bar, k is a real exponent and $w_i = E_i/E_{\text{total}}$ is

the weight factor. A number of exponents starting from fractional values less than 1 to higher rational numbers were considered for the exponent ‘k’ and it was observed that the ROC curve starts to really improve for powers beyond 1. But as we start going beyond $k=2.5$, the ROC curves almost overlap, hence the value of ‘k’ is fixed as 2.5. The ‘ D_k ’ formula is observed to be sensitive to the energy deposition profile and hence discriminates reco prompt from the capture γ -ray background better than simply using base variables. Even before MLP classifier

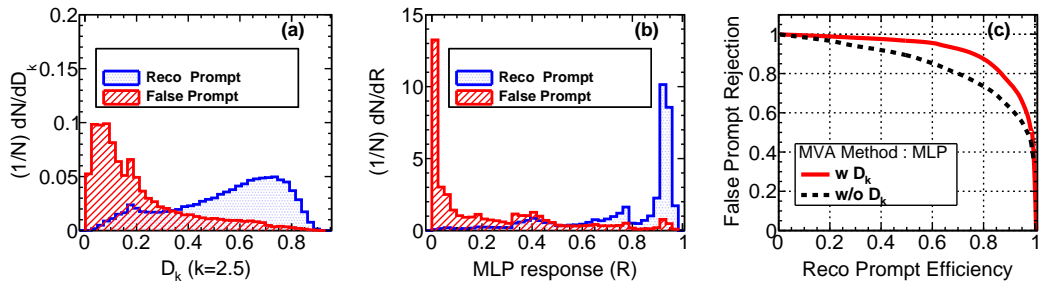


FIGURE 4.6: Panel (a) shows the reco prompt and false prompt event separation for D_k variable for IBD events in ISMRAN. Panel (b) shows the response after application of MLP classifier including the D_k variable along with N_{bars} and sum energy variable. Panel (c) shows the improvement in the ROC curve of MLP classifier with inclusion of D_k variable for reco prompt efficiency and false prompt rejection.

is trained with the inclusion of this new variable, the selective nature of D_k is seen in signal and background separation as seen in Fig. 4.6(a). At the variable level itself the signal and background separate away from each other. Consequently the MLP classifier response also improves (figure 4.6(b)) after inclusion of D_k . Fig. 4.6(c) confirms this improvement by comparison of ROC curves with and without inclusion of D_k . About 10% increase is observed in the signal efficiency at the same background rejection 80% considered earlier. With inclusion of

this variable the MLP framework is finalised for ISMRAN event classification. Further classification is tested for different types and components of background.

MLP classifier response for Gd and H capture background

The de-excitation mechanism of Gd and H nuclei following the neutron capture is altogether different and needs to be studied separately in context of MLP classifier. Since, Gd is a heavier nuclei ($Z=64$) and closer to the maxima of binding energy per nucleon curve, it releases ~ 8 MeV energy upon neutron capture in the final state while neutron capture on H leads to formation of deuterium with release of much lower energy of 2.2 MeV. Also, unlike deuterium the de-excitation of the Gd nucleus is not a single transition and involves many intermediate energy levels of the nucleus leading to the release of different cascades of γ -rays in each instance. Thus, the classifier variables have different characteristics. The aim of this exercise is to study the classifier performance for its effectiveness for these two cases. It also helps to understand whether the remaining inefficiencies have their source in H-capture events. If this is so, some modified threshold conditions could be considered to remove these events. By filtering the Gd-capture and H-capture events separately from the IBD simulated events the MLP response is trained and tested for reco prompt identification. The classification response of MLP for reco prompt selection with separated Gd and H neutron capture background events is shown in figure 4.7 (a) and (b), respectively. In both cases, the MLP is able to separate the reco prompt events from capture events with high efficiency. Figure 4.7 (c) shows the ROC curves for both cases overlapped for comparison. The rejection of false prompt events using MLP is slightly low in

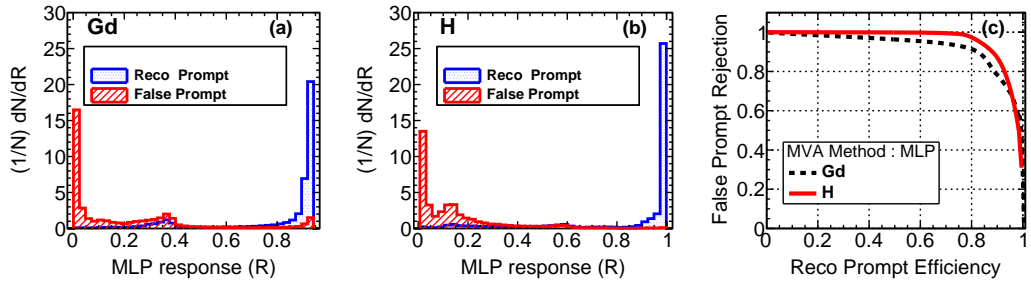


FIGURE 4.7: Panel (a) and (b) shows the MLP classifier response for reco prompt events from positron and false prompt events from neutron capture on Gd and H, respectively. Panel (c) shows the comparison of ROC curve for the reco prompt efficiency and false prompt rejection from neutron capture events on Gd and H.

H capture events compared to Gd capture events. This is evident in ROC as the responses depart slightly at higher reco prompt efficiency. But this departure is only at $\sim 5\%$ level.

MLP classifier response for reactor γ -ray background

A major source of background to the ISMRAN setup is the reactor hall γ -ray activity due to the proximity to the core and also to the neutron guide tube and beam dumps. The γ -ray emissions from the core itself cannot penetrate the ~ 4 m deep biological shielding made up of layered annular segments of stainless steel, concrete and light water shields. But the thermal neutrons from the beam ports and those due to leakage from guide tube can get captured in the surrounding material in the form of beam dumps and metallic structures and produce high energy γ -rays, which in turn can be a huge background to the setup. In order to test the MLP classifier's effectiveness against such a background we use a highly precise reference γ -ray spectrum of the NBSR reactor

site measured with large volume HPGe detectors as part of the PROSPECT experiment's site selection studies [102]. Due to the varied background and intense activity observed at the NBSR site, this exercise forms a good test bed for the MLP classifier in a realistic scenario. As these γ -rays are expected to be broadly uncorrelated amongst themselves, these events were incident one at a time on the fully shielded ISMRAN geometry in simulations and passed through the same recording procedure to form a tree of background events. The MLP classification is then trained for classifying the reco prompt events in the above background. The separation provided by the MLP response is shown in the Fig. 4.8(a). The ROC curve shows a small drop compared to the earlier performance for the capture γ -rays as seen in fig. 4.8(b). A reco prompt efficiency of $\sim 90\%$ is achieved with $\sim 70\%$ of reactor related γ -ray background event rejection.

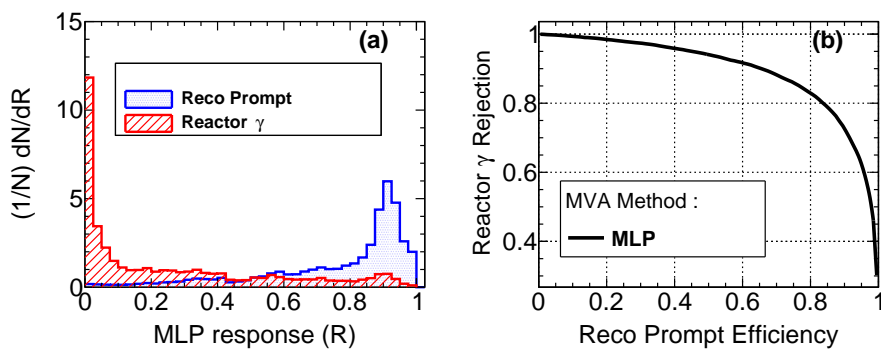


FIGURE 4.8: Panel (a) MLP classifier response for reco prompt events from positron and reactor γ -ray backgrounds. Panel (b) ROC curve for the reco prompt efficiency and reactor γ -ray background rejection.

MLP classifier response for reactor neutron background

Fast neutrons in the reactor environment pose a formidable challenge to the $\bar{\nu}_e$ detection as they are capable of mimicking the dual signature of IBD. A fast neutron entering in ISMRAN detector can elastically scatter inside the proton-rich volume of scintillator producing a positron like signature and lose energy till it thermalizes and gets captured on Gd or H to produce de-excitation γ -rays much like the IBD event. The delayed event cannot be distinguished as the capture event is the same. Also, the PS volume is not sensitive for particle ID of neutron (no PSD capability) as it can only sense EM interactions. Thus we are left with discriminating the positron dE/dx and annihilation signature from the proton recoil signature of fast neutrons. For this purpose, fast neutrons with

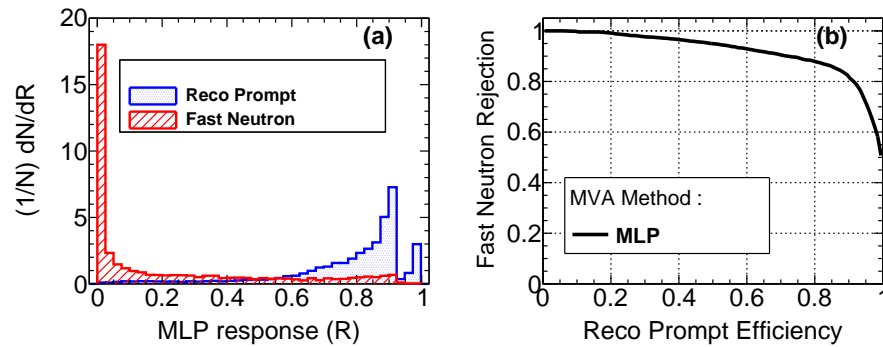


FIGURE 4.9: Panel (a) MLP classifier response for reco prompt events from positron and proton recoil events from fast neutrons. Panel (b) ROC curve for the reco prompt efficiency and fast neutron rejection.

a uniform distribution of energies ranging from 2–20 MeV are incident on the shielded ISMRAN and background tree is populated with their sum energy, N_{bars} and D_k variable values. Figure 4.9 (a) represents the separation offered by the MLP classifier between the reco prompt events and proton recoil events due to

fast neutrons. The ROC curve for the reco prompt efficiency and rejection of proton recoil events from fast neutron shows efficiency of $\sim 80\%$ is achievable with a rejection of proton recoil events close to 84% .

4.7 Evaluation of the MLP classifier performance for reco prompt selection

A mixed background sample of 100000 events made up of Gd and H capture events in the 3:1 proportion is independently prepared in ISMRAN simulation for performance evaluation of MLP classifier. The robust MLP classifier response at lower energies for rejecting reactor γ -ray and neutron backgrounds allows lowering of thresholds on base variables. This is useful for inclusion of delayed events where IBD neutron captures on H and consequently increases the efficiency of $\bar{\nu}_e$ detection but also potentially increases the contamination to the reco prompt events. But, as we saw in the classification results, the classifier has high efficiency for reco prompt identification from a H-capture sample too. Thus, this sample is used to find out the performance parameters i.e. the efficiency, purity and their product as a function of cuts on the MLP response. The efficiency and purity parameters are again reflecting the true positive or signal selection and false positive or background rejection. The third parameter which is the product, is useful to identify the operating region in terms of the cut values on MLP as it depicts where the efficiency and purity are balanced for optimal performance. The behaviour of these three parameters for our MLP framework is shown in figure 4.10 for different cuts on the MLP classifier. MLP response values from

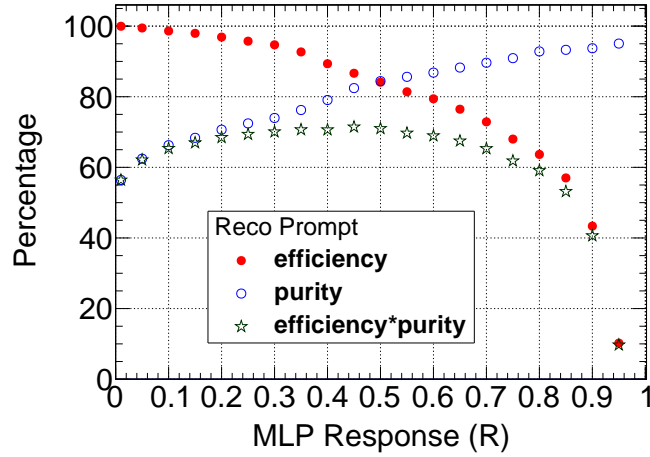


FIGURE 4.10: Reco prompt efficiency, purity and product of efficiency and purity for MLP as a function of different selection cut values on the MLP output.

0.2 to 0.6 show a maximum value of the product of signal efficiency and purity at about 70% and almost constant. Two popular figure of merit (FOM) values can be constructed for obtaining the MLP classifier effectiveness in terms of the signal and background events in the filtered sample. These are the $s/\sqrt{(s+b)}$ and s/\sqrt{b} , where s and b are the reco prompt signal and false prompt background events, respectively. The graph of $s/\sqrt{(s+b)}$ as a function of MLP cut value, brings out the region of maximum reco prompt signal efficiency. On the other hand, the plot of s/\sqrt{b} vs MLP cut values provides the range in which highest purity of the reco prompt signal is observed in the presence of false prompt background events. The table 4.1 lists the FOM values observed for obtaining the maximum efficiency and purity respectively. It is obvious that the maximum efficiency and purity values don't coincide as maximizing the efficiency involves lowering the MLP cut value which allows more background contamination, and vice versa for

4.7. EVALUATION OF THE MLP CLASSIFIER PERFORMANCE FOR RECO PROMPT SELECTION

TABLE 4.1: Efficiency, purity and false rejection performance for reco prompt events.

	MLP cut value	Efficiency (%)	Purity (%)	False Rejection (%)
$s/\sqrt{s+b}$	0.37	91.5	77.3	73.1
s/\sqrt{b}	0.88	56.4	93.5	96.1

purity. The efficiency, purity and false prompt rejection values are tabulated for these cut values.

The cut of 0.37 on MLP response provides the maximum reco prompt efficiency value which is 91.5% with ~27% background contamination. As compared to the maximum of 69% efficiency of prompt selection offered by the analysis cuts, this is a significant improvement (refer table 3.3). The maximum purity achievable is ~93% at the MLP selection cut of 0.88. Here the efficiency drops to ~56%. The cut value on the MLP response may be selected somewhere between these two values to achieve an optimal reco prompt signal efficiency with a reasonable reco prompt signal purity, but for the purpose of detection, efficiency is the deciding factor and hence choosing cut of 0.37 is more advisable. Further, the $\bar{\nu}_e$ spectrum is reconstructed from the prompt spectrum obtained after classifier selection and is expected to replicate the spectral shape. This implies that it is important to study the spectral shape of the classified events. An independent set of 10^5 IBD events is used for the spectral reconstruction using the MLP classification. The events which are selected for 0.37 cut on MLP response are selected for prompt sum energy spectrum reconstruction. Figure 4.11 (a) shows the true input prompt sum energy distribution of IBD events (in black), reco prompt event sum energy distribution from MLP response (red dashed) and same from a simple cut based analysis choosing ‘loose’ cuts on reco prompt

events, as in table 3.3(dashed dot blue). Due to higher selection on individual variables in case of cuts, the distribution also has a sharp threshold below which there are no events, while the MLP is more inclusive and retains the shape of true prompt spectrum. Figure 4.11 (b) shows the delayed capture event (false

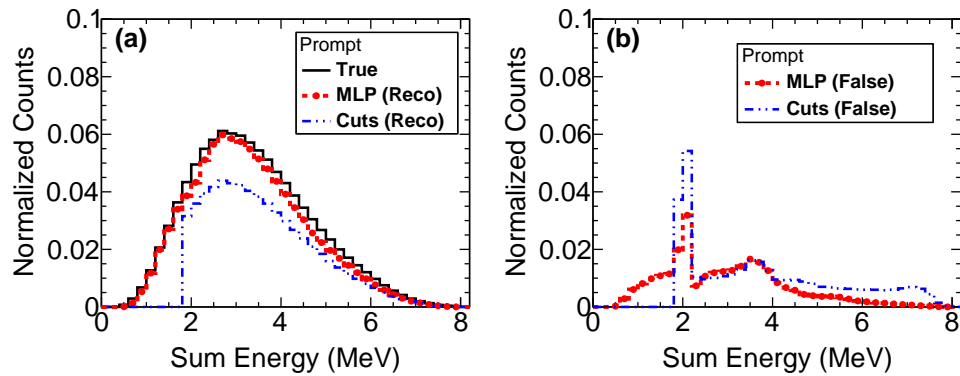


FIGURE 4.11: Panel(a) : Prompt sum energy distribution for true input, reco prompt events classified with MLP and from a cut based analysis. Panel(b) shows the false prompt events which are misidentified as reco prompt events using MLP classifier and cut based analysis.

prompt) energy distribution for MLP and cut based analysis which are wrongly classified as reco prompt signal events. The integrated counts in the MLP false prompt distribution is lesser than those from cuts analysis. Also, the the 2 MeV peak and higher energy continuum is suppressed which reduces the distortion in the MLP classifier signal response. Thus, the trained MLP response provides a more realistic representation of the $\bar{\nu}_e$ spectrum.

4.8 Summary

The offline reconstruction of IBD event in ISMRAN demands high efficiency separation of reconstructed prompt event from background events. The cut based analysis is observed to provide a maximum possible efficiency of $\sim 21\%$. To improve upon this a better IBD prompt event classification using machine learning algorithm – Multi-Layer Perceptron (MLP) is attempted in simulations. The MLP classifier technique is observed to demonstrate excellent reco prompt and false prompt event separation. The false prompt events included different sources of background such as the actual capture γ -ray event, reactor γ -ray and fast neutron scattering event. The performance comparison of MLP classifier vs cut and likelihood based classification shows significant improvement in efficiency and purity of reconstructed prompt event in case of MLP. With addition of a new variable D_k based on a weighted energy deposits in PS bars, the MLP performance further improves. MLP based classification offers reconstructed prompt efficiency of $\sim 91\%$ and rejects $\sim 73\%$ of the background or false prompt events in ISMRAN. Reconstructed prompt spectrum due to MLP shows less distortion and replicates the true $\bar{\nu}_e$ spectrum with high precision.

Chapter 5

miniISMARAN data-taking and analysis

5.1 Measurements with miniISMARAN

The miniISMARAN prototype detector consisting of 16 PS bars in a 4×4 matrix (32 PMT channels) uses two of the V1730 digitizers for its DAQ. This prototype setup is operated in the non-reactor (laboratory) environment and later moved to the reactor site location. The operation in the laboratory mostly involved characterization (see section 2.8) followed by cosmogenic background data-taking. Following this, the setup was moved to the reactor hall location at a standoff of ~13 m from reactor core and covered from all side with the 10 cm

Pb and 10 cm BP shielding. An elaborate data-taking campaign was started in reactor ON (RON) and OFF (ROFF) conditions, which also included background measurements for γ -rays and neutrons using LS and inorganic scintillators. 13 PS bars out of 16 showed consistent performance throughout the data-taking and the rest 3 bars suffered time-dependent gain drifts hence excluded from analysis. Data was taken throughout the year in 2018 up until last quarter of 2019 but with interruptions. However the data taken in March during full maintenance shutdown (ROFF) and in June, November and December (RON + ROFF) of 2018 had uninterrupted full month data with reactor ON at average thermal power of about 60–80 MW. The final analysis to filter $\bar{\nu}_e$ candidate events is performed on these datasets.

5.2 Non-reactor and reactor background measurements with miniISMARAN

There are multiple sources of backgrounds which can pose a challenge to the $\bar{\nu}_e$ detection setup like ISMRAN. These can be divided into γ -rays, neutron and cosmic muon backgrounds. The prompt-delay coincidence requirement for IBD detection reduces the uncorrelated backgrounds to some extent, but, these same activities can also give rise to correlated events inside the detection volume, when they combine as follows:

1. $\gamma - \gamma$: Two external γ -rays combining to produce a prompt-delay signature.
2. $\gamma - \text{neutron}$: A sufficiently energetic γ -ray giving prompt signal and a background neutron getting captured inside the volume in time vicinity to

pose as a delayed event.

3. neutron – γ : Here a fast neutron causes a proton-recoil to mimic a prompt-like signature and later undergoes radiative capture to give the delayed event. A sufficiently energetic γ -ray may also provide a delayed signature here.
4. neutron – neutron : A elastic scatter of a fast neutron and a later capture event due to same or different neutron forming the prompt-delay pair.

Cosmic muons can also induce prompt-delay mimicking activities either through production of γ -rays and neutrons or forming long-lived beta decaying nucleides. Some of the sources of such backgrounds at the site of ISMRAN are described below.

γ -ray background sources

The sources of γ -ray backgrounds can be the natural γ -ray activity present in the surroundings i.e. in the wall composition, soil, organic matter, detection materials or that encountered in reactor environment. Prominent amongst these are the ^{40}K :1460 keV γ -ray and the ^{208}Tl :2614 keV γ -ray. The ^{40}K is present in all organic matter along with natural potassium (120 ppm) and in most commercial PMT photocathodes. It has a long $T_{1/2}$ of $\sim 1.2 \times 10^9$ years and hence source of substantial activity. The ^{208}Tl on the other hand is amongst the last daughter products of thorium decay chain and hence part of earthly matter. Apart from these other radioactive isotopes of uranium and thorium decay chains such as – ^{224}Ra , ^{226}Ra , ^{214}Bi , ^{214}Pb , ^{228}Ac and another thallium isotope ^{212}Tl contribute

to this background but in smaller amounts [103]. Reactor environment γ -rays are mostly due to the escaping neutrons (from beam ports and guide tubes) getting captured on surrounding materials mostly support or shielding structures containing Fe, Co, B, C isotopes.

Neutron background sources

The neutron background to our setup is mostly from reactor and to a relatively small extent from cosmic showers. The reactor neutrons are mostly from thermal ($O(10)$ of meV) and fast (1–20 MeV) spectrum, coming from the beam ports and neutron guide tubes in vicinity, meant for scattering experiments. The cosmic neutron activity spans the very broad energy range starting meV extending up to 1000s of GeV and are due to the cosmic primaries (charge particles) hitting atmospheric gas nuclei. The neutron fluences expected for cosmic neutrons at sea level are at $\sim 0.01 \text{ cm}^{-2} \text{ s}^{-1}$ level [82]. About 10% neutrons, in energy range from MeV and above have been observed to penetrate the ISMRAN shielding.

Muons and their induced backgrounds

The muon activity is again from the cosmic particles (mostly protons) striking the earth's atmosphere at high altitudes and producing showers of pions and kaons most of which produce muons in their decay. Being in the minimum ionizing energies they can easily penetrate ISMRAN shielding and on occasions interact with the high Z materials like Lead and Steel to induce spallation reactions which basically break such nuclei and produce a correlated shower of neutrons and pions. The muons which stop inside the volume can produce short and long

lived radioactive nuclide like ^{12}B , ^{12}N , ^9Li and ^8He [104]. The first two nuclei produce beta particles and the latter ones are also delayed neutron emitters. These nuclides usually have few ms of lifetime and usually produce a dual signature like IBD event. One of the purpose for operating the prototype miniISMARAN has been to measure the background rates in non-reactor and reactor environment to get the level of such backgrounds expected for ISMRAN.

5.2.1 Non-reactor background measurement

The miniISMARAN setup was operated for about 2–3 months in the laboratory environment to help identify and quantify the surrounding natural activity. As observed from Fig 5.1 the calibrated distributions of the natural activity show the compton edges perfectly coinciding with those expected due to ^{40}K and ^{208}Tl . A bump at ~ 20 MeV is due to the minimum ionization energy deposited by muons in the 10 cm thick PS bar. The average non reactor background rates in a single unshielded PS bar from different natural sources are ~ 27 Hz and ~ 10 Hz for ^{40}K (1.460 MeV), ^{208}Tl (2.614 MeV) around the compton edge energies and ~ 6 Hz for cosmic muons in the 12–24 MeV region covering the most-probable-value or MPV (20 MeV) of their landau distribution, respectively. The integrated non reactor background rate in 3–8 MeV region is ~ 132 Hz. For a 16 bar matrix these values translate to a cumulative background event rate of maximum 2 kHz for the complete matrix without shielding. With 10 cm Pb and 10 cm BP this rate drops down to about 200 Hz cumulative rate as observed in miniISMARAN.

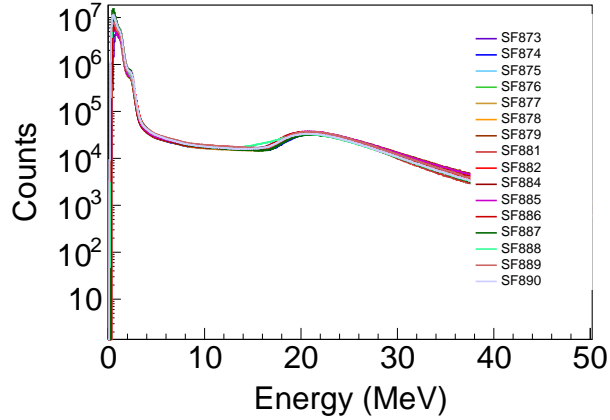


FIGURE 5.1: Non-reactor background spectrum recorded in 16 PS bars of the unshielded miniISMARAN setup in laboratory.

5.2.2 Reactor background measurement

Background in PS bar

Measurements have also been performed to quantify reactor ON and OFF background once the miniISMARAN setup was moved to the reactor hall site. First set of measurements have been performed to understand the reduction of overall rates starting from no-shield to full 10 cm Pb and 10 cm BP shield for the miniISMARAN (see Fig 5.2). An integrated background rate of ~ 24 kHz in the energy range from 0.2 MeV to 40 MeV is measured in the miniISMARAN array, without any shielding. With full shielding this rate drops down to ~ 500 Hz at full power. The high γ -ray activity recorded in the miniISMARAN PS matrix can be attributed to thermal neutron captures on the surrounding metallic structures. This background can be further reduced to about 10 Hz (3 orders of magnitude drop) by also introducing a correlation criteria of $N_{\text{bars}}=2$ within a $\mathcal{O}(10)$ ns time coincidence window. The individual PS bar rates for reactor ON condition,

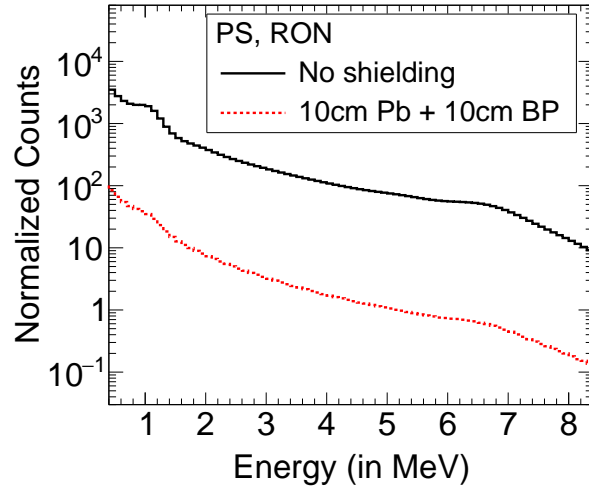


FIGURE 5.2: Energy spectrum recorded in ISMRAN PS bar under reactor ON condition for no-shielding and full shielding configurations.

TABLE 5.1: Background rates measured in mini-ISMARAN for various shielding configurations in reactor ON condition.

Detector configurations	Count Rates (Hz)
No Shielding (Single PS bar)	~ 24,000
10 cm thick lead shield	~ 2,000
10 cm thick lead + 10 cm thick B.P.	~ 500
10 cm thick lead + 10 cm thick B.P. ($N_{\text{bars}} = 2$, time window < 40 ns)	~ 10

as measured under various shielding levels and coincidence condition can be summarized as in table 5.1.

Once the shielding was in place, the quantification of reactor ON and OFF backgrounds as seen in miniISMARAN PS bars could be measured. Spectrum recorded in a single bar, shows 10 times more background rate in reactor ON as compared to reactor OFF (see Fig. 5.3). Up to about 7 MeV the background seen

in the reactor ON is due to the high energy γ -rays from neutron capture in surrounding material. Beyond 10 MeV, the reactor ON and OFF background scales indicating that the natural backgrounds primarily the cosmic muons dominate in this region.

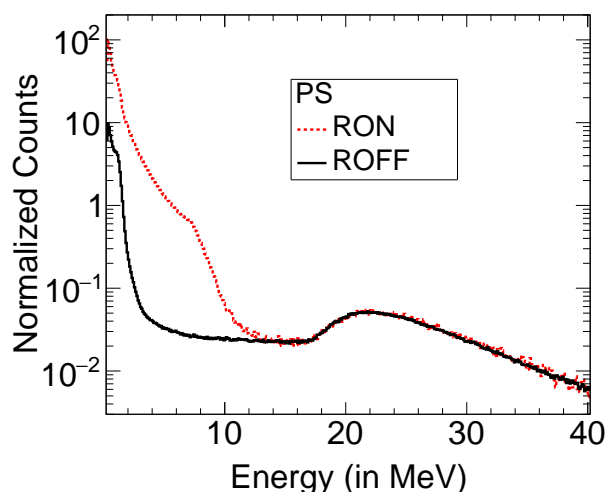


FIGURE 5.3: Energy distributions recorded in ISMRAN PS bar under full shielding reactor ON and OFF conditions.

γ -ray background from CeBr_3

As the PS cannot distinguish the γ -ray and neutron activity, an inorganic CeBr_3 scintillator with 2" crystal was used to measure specifically the γ -ray activity in the low energy region. The energy spectrum as obtained by CeBr_3 shows the individual radiations with much better resolution due to very efficiency and high resolution ($\sim 4\%$ at 1 MeV) in the lower energies up to about 3 MeV. Such precise spectrum is useful for simulating such backgrounds in ISMRAN geometry. The CeBr_3 scintillator was placed just next to the miniISMRRAN PS array inside the 10 cm Pb and 10 cm BP shielding. Reactor ON and OFF data were recorded in

this arrangement and compared, as seen in Fig 5.4. High γ -ray activity can be attributed to the thermal neutron capture γ -ray incident on the setup. Possible reasons maybe a quasi elastic neutron scattering experiment next to the ISMRAN setup uses a thermal neutron beam port with $\sim 10^5 \text{ n} \cdot \text{cm}^{-2} \cdot \text{s}^{-1}$ flux and guide tube running just 1.5 m away from miniISMARAN setup.

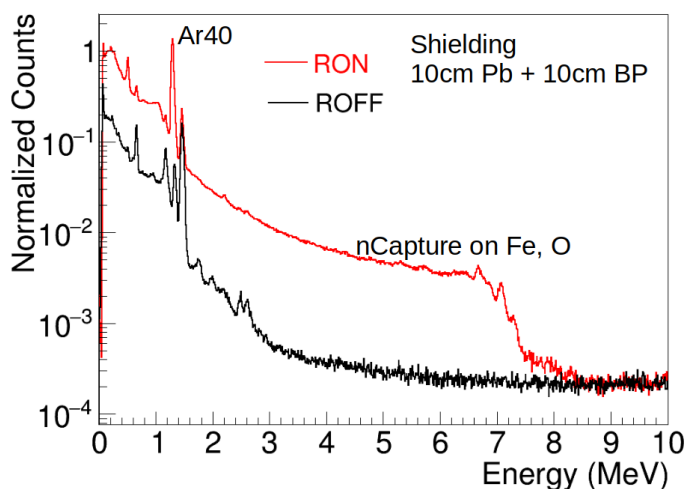


FIGURE 5.4: Energy distributions recorded in a CeBr_3 γ -ray detector under reactor ON and OFF conditions.

The prominent feature in the reactor background are highlighted in the spectrum. Interesting additions to the natural activity in reactor ON include: the Annihilation γ -rays, ^{40}Ar peak due to ambient neutron capture on argon in air as well as high energy γ -rays (6-8 MeV) from neutron captures on Fe and O elements present in the surrounding metallic structures and water loops. The high energy features appear suppressed as the efficiency of photoelectric process inside CeBr_3 falls down around these energies and much Compton scatterings occur which is evident in the large plateau like feature leading up to the small peaks. Possible H-capture signature is also seen at 2.2 MeV. Thus the overall

capture activity is much higher in the energies beyond 3 MeV. The reactor OFF condition measured had some nominal thermal power still maintained, hence ^{40}Ar is still visible. However, some of the other activities such as ^{137}Cs , ^{60}Co and natural γ -rays from ^{40}K , ^{208}Tl and ^{214}Bi are now clearly visible.

Fast neutron background in LS

Identifying neutron activity in PS is not possible as the pulse shapes for both γ -ray and neutron signals have nearly same profile. Using a liquid scintillator comes in handy in such situation as neutron interactions produce slightly stretched out pulse in its volume owing to delayed fluorescence phenomenon. A pulse shape discrimination (PSD) algorithm in digiTES software then distinguishes the neutron using the PSD variable ($\text{PSD} = 1 - \frac{Q_s}{Q_L}$) (see section 2.6.1). Plotting a 2-dimensional PSD vs Energy (MeV_{ee}) brings out two distinct set points as seen in Fig 5.5. Due to the peculiar formulation of the PSD formula, the lower lobe

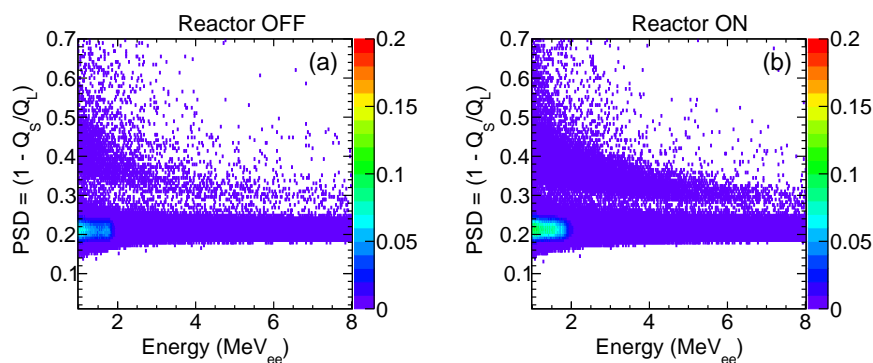


FIGURE 5.5: PSD vs Energy plot for events recorded with 5" liquid scintillator inside full ISMRAN shielding.

of points signifies γ -ray events, while upper blob represents the neutron events. This representation as plotted for reactor ON and OFF qualitatively shows the

reduction in both the radiations. Also the relative rates of the neutron w.r.t the γ -rays is observed. If we take a slice of this distribution for energy range $1.5 < E(\text{MeV}) < 6.0$, which selects a major chunk of the fast neutron spectrum, a quantitative picture is obtained. With these cuts a $\sim 10^{-6}\text{Hz cm}^{-2}$ rate of fast neutron background is observed inside the shielding. As observed from Fig 5.6

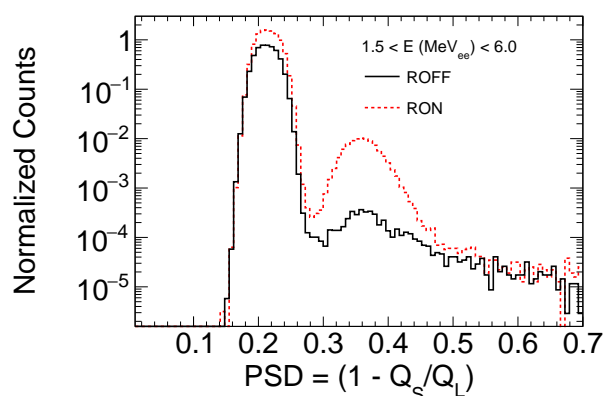


FIGURE 5.6: PSD plot for events recorded with 5" liquid scintillator inside full ISMRAN shielding for specific energy cut.

the relative rate of neutrons is 2 orders of magnitude lower than the γ -rays. Also the reduction seen in neutron rates, going from On to OFF condition is more than 1 order of magnitude. This quantification can then be scaled to the ISMRAN geometry and included in simulation to understand the neutron induced signature events in the final detection volume.

Monitoring stability of PS bars

Operating the miniISMARAN under full shielding requires arrangement for in-situ calibration, to ensure gain drifts are monitored. Hence, a gap was introduced early on, by shifting the central PS bars so that a radioactive source like ^{22}Na can

be introduced near the center. However, in between calibration rounds, there is a need to rely to some known background to monitor operation stability of PS bars. This is to ensure that the measured data has been consistent throughout the data-taking period. Due to the 10 cm Pb and 10 cm BP shielding the natural activity peaks gets suppressed significantly.

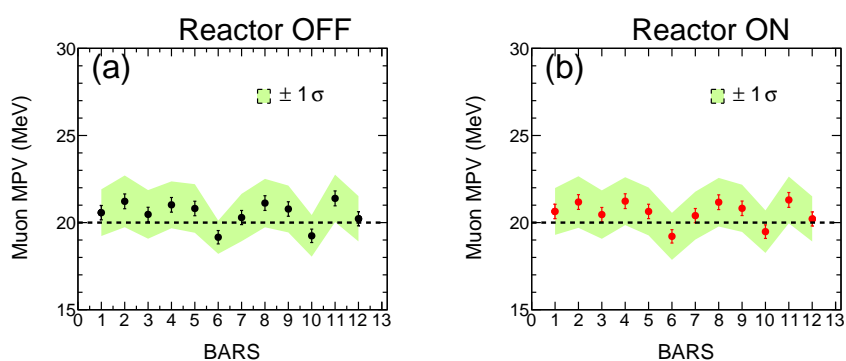


FIGURE 5.7: Deviations from the expected MPV for muon events in all the miniISMARAN PS bars at the reactor site.

However, the high energy cosmic muons can penetrate the shield and their fixed MPV of 20 MeV in the ISMRAN calibration scale can be indicator of voltage stability. Any deviation from this energy point can indicate shift in PMT bias. As shown in figure 5.7 the monitored MPV of 13 PS bars with consistent response is plotted for the month of June 2018. This same monitoring was done for other data-taking periods too and it was found that these bars had a uniform response throughout.

5.3 Event building in reactor data

The data from miniISMARAN matrix is acquired with the minimum threshold (0.2 MeV) on energy in each PS bar. The minimum requirement to register a hit in a bar is to have a coincidence of both the end PMTs triggering above threshold within a 16 ns window. This minimum bias acquisition of hits generates large volume of data, but is still useful as the high single event rates in the reactor ON condition will cause a more complex triggering scheme to introduce higher dead time and hence more event loss. Once all the bar events are written, a sorting of the data using timestamps is done to bring the events into a chronological sequence. The bulk of analysis then happens offline, with event variables being calculated using proper grouping of hits. For a single event it can be safely assumed that the timestamps of hits are distributed close to each other. If a time difference plot is generated for each pair of successive bar hits, then the correlated events are all seen to fall within 20 ns window, while the flat distribution beyond 20 ns is due to the uncorrelated events, as seen in Fig 5.8. These set of events

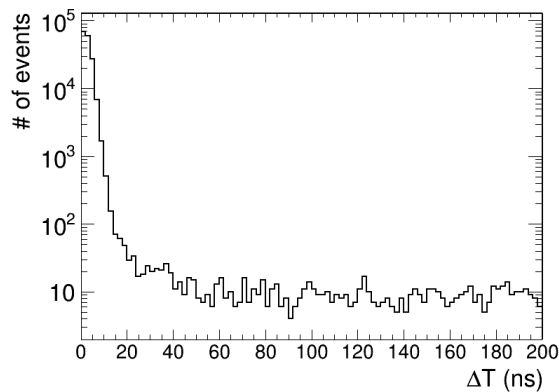


FIGURE 5.8: Inter bar ΔT distribution for events in the miniISMARAN matrix.

then are imposed with prompt and delay event cuts for further analysis.

5.3.1 Prompt and delayed events in ISMRAN

While making the classification of prompt and delayed events in miniISMARAN, the cuts are decided based on the simulations of pure IBD events. For a calibrated bar event to qualify its energy should obey the selection : $0.2 < E_{\text{bar}}(\text{MeV}) < 7.5$. The lower cut ensures spectral uniformity among all the bars and the upper threshold ensures selecting only the energy region of interest covering the $\bar{\nu}_e$ spectrum and the neutron capture energy. All the higher energy backgrounds are rejected by this cut. Next, the bar hits within 20 ns is summed up for deriving the sum energy variable. The number of bars : N_{bars} involved in an event is also recorded. Classification of these miniISMARAN events then follows using more stringent cuts to label them as prompt or delayed events. The simulation derived E^{prompt} and E^{delayed} cuts (or shorthand E_{pr} and E_{dl}) and N_{bars} are then imposed for this classification.

1. Prompt event : $2.6 < E^{\text{prompt}}\text{MeV} < 8.0$ and $1 < N_{\text{bars}} < 4$

2. Delayed event : $3.0 < E^{\text{delayed}}\text{MeV} < 8.0$ and $3 < N_{\text{bars}} < 9$

The prompt and delayed events chosen at this level are called ‘raw’ prompt and delayed events, as they have been not been screened for any background contamination. The cosmic muon contamination is one of the first level backgrounds which needs to be filtered out. We have already removed the high energy hits but their associated activity has not been considered yet. Figure 5.9(a) shows mean time delay distributions for raw events in reactor OFF and (b) reactor ON. The muon contamination can be in either the raw prompt or the raw delayed event only or both. While there will also be events where there is no muon contamination.

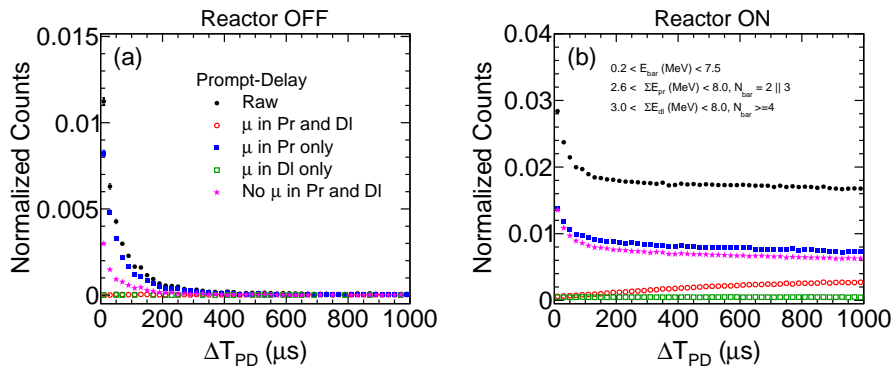


FIGURE 5.9: ΔT_{PD} between prompt and delay events with cosmic muon contamination in reactor OFF and ON conditions.

Removing the muon contamination can be realized by introducing a dead time before and after the timestamp where the muon event was located. The raw events found in a $250 \mu s$ window before and after this timestamp are removed. The large time scale allows for correlated activity induced by muons to die down.

At this juncture, it is worthwhile to look at the selected raw events by relating them to reactor power i.e. how these event rates change under ON and OFF and power changes in a reactor cycle.

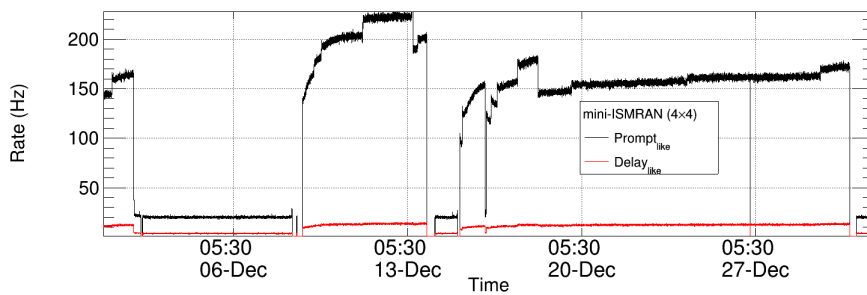


FIGURE 5.10: Raw prompt and delay event rates during reactor ON and OFF periods in the month of December 2018 from miniISMIRAN data.

Figure 5.10 show these raw prompt and delay-like event rates as a function

of time in the month of December. These rates are referred to as the ‘global rates’ which is basically the cumulative rates for all bars with threshold cuts. RON state is distinguished from ROFF using the cut of at least 600 Hz of global rate to be observed for a time period of 6 hrs. Figure 5.11 in the month of March when there was a complete shutdown for maintenance and rates are seen below 1 Hz level. A general observation to make is that the delay-like events are usually at least 4 times smaller than prompt like events as the prompt event is more susceptible to background contamination due to lower N_{bars} requirement and also miniISMRAN capture events are in general not contained and hence there is lot of inefficiency in the delayed selection.

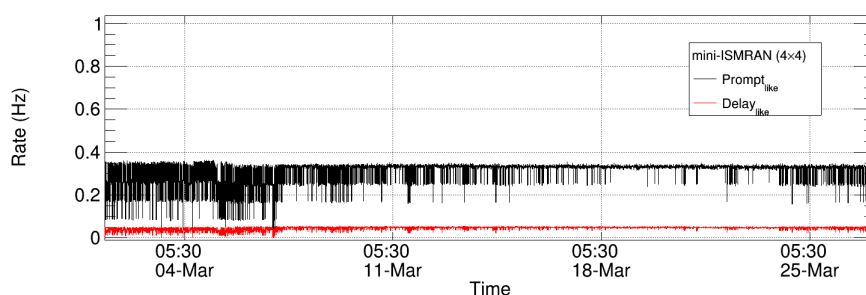


FIGURE 5.11: Raw prompt and delay event rates during the complete shutdown in the month of March 2018 from miniISMRAN data.

The remaining raw events after muon rejection are in the form of various combinations such as prompt following a prompt event, prompt preceded by a delay event, two simultaneous delay events or prompt followed by two close-by prompts called double prompts as seen in figure 5.12. These combinatoric backgrounds owe themselves to the huge uncorrelated background, which can form such pairs among themselves and with real events. All such false pairs are filtered out.

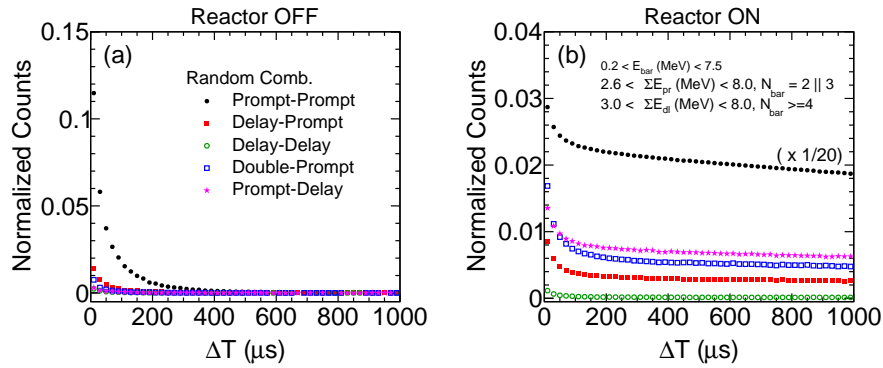


FIGURE 5.12: ΔT_{PD} between raw events in different combinations after cosmic muon contamination removal in reactor OFF and ON conditions.

Additional cuts on prompt and delayed events

Additional requirements need to be imposed on the raw events to filter out background. For this the basic cuts on sum energy and N_{bars} need to be augmented with additional criteria. These new cuts had been introduced in the simulations section 3.4, especially for miniISMARAN, since the basic cuts assumed larger ISMRAN geometry and was not possible to simply use them in miniISMARAN data. The small geometry effect and the uncorrelated backgrounds are the primary driving factors for such additional cuts.

Selection on timestamps and Z-positions

To remove the uncorrelated background, timing and topology of event can be utilized. As the uncorrelated event can have hits anywhere in the PS matrix the requirement of contiguous bar hits can selectively chose correlated events which is expected for IBD. Additionally, due to the rapid energy loss and annihilation of positron, the expected time window within which the prompt event happens

is very small, usually not more than 5 ns from the time the first hit is observed. Same is true for a delayed event where the cascade very quickly deposits energy within few ns.

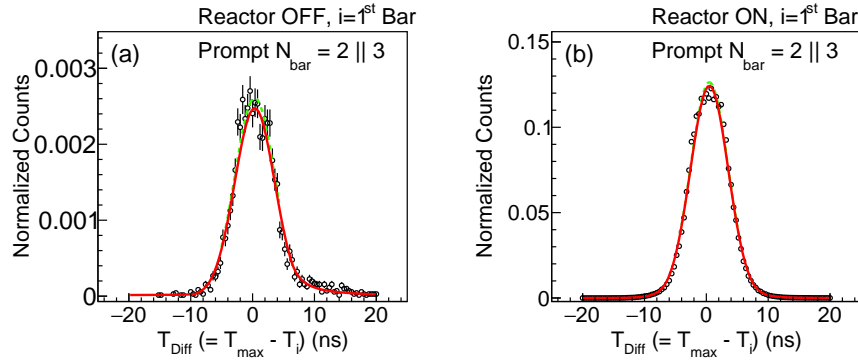


FIGURE 5.13: Difference of timestamps 2nd highest to highest energy deposit for prompt events with $N_{\text{bars}}=2$ or 3.

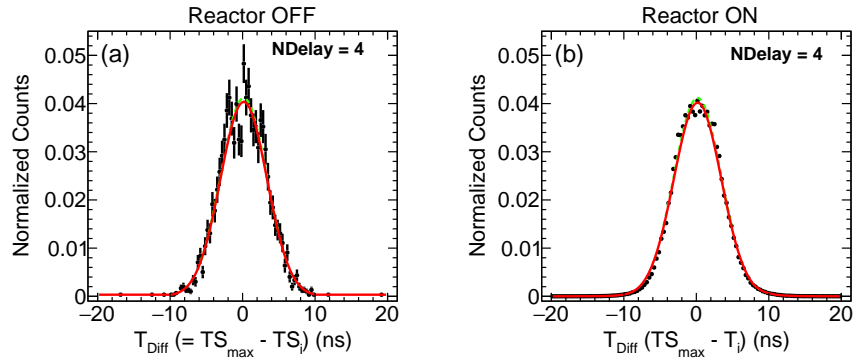


FIGURE 5.14: Difference between the timestamps of highest and the next highest energy PS bar for a 4 bar delay event.

A cut to utilize this instantaneous behaviour can be implemented on the distribution of timestamp differences for bar deposits in an event. Figure 5.13 panel (a) and (b) show these distributions for reactor OFF and ON conditions for

prompt events and Fig 5.14 panel (a) and (b) represent this cut in the delayed event, respectively. The delayed events are only depicted for 4 bar events as higher bar events had lower statistics in miniISMARAN. A cut of 1.5σ on these distribution selects the first two highest energy bars close to each other within 5 ns interval. This ensures selection of coincident (correlated) hits and rejection of any uncorrelated background happening later. For a 3 bar prompt event, this cut can also be used for checking closeness of 2nd highest energy to 3rd highest energy bar (see Fig 5.15).

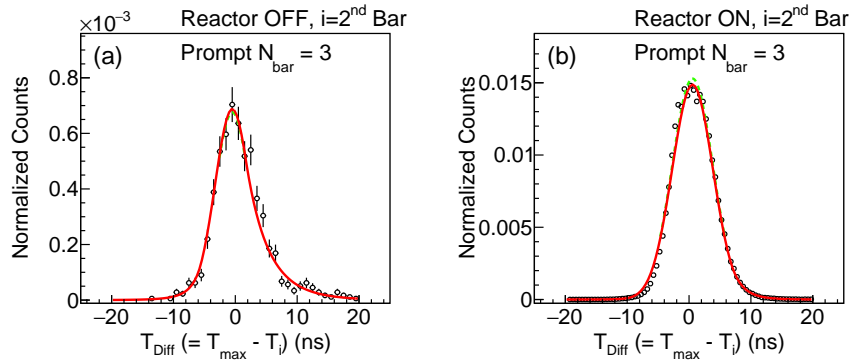


FIGURE 5.15: Difference of timestamps of 3rd highest and highest energy deposit for prompt events with $N_{\text{bars}}=3$.

The E_{max} or highest bar energy for an event, considered here after timestamp sorting is required to lie at $T = 0$ i.e. at the start of a candidate prompt event. This requirement stems from the fact that both positron dE/dx and epicenter of γ -ray cascade for delayed event is expected to be the highest loss preceding any Compton scattering losses later. For prompt event it is obvious, since the higher cut allows only sufficiently energetic positrons to be selected. For the delayed events the event also needs to include a central bar due to its smaller geometry.

An important distinction, specific to the prompt event, is that most of the

uncorrelated backgrounds is lower in energy, with ^{208}Tl being the highest energy contributor. Consequently, a threshold like cut of 2.4 MeV on the highest energy bar in a prompt event is introduced. Finally, to remove higher energy deposits due to passing muons or high energy γ -rays from ambient neutron capture contaminating a prompt event, a high energy deposit of 5.5 MeV is allowed only in one PS bar.

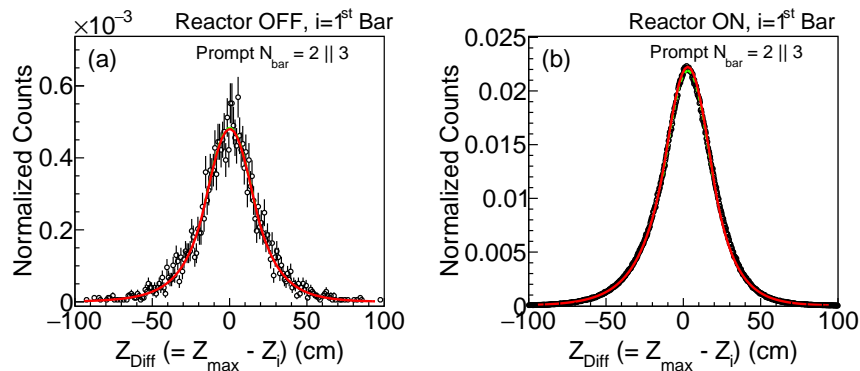


FIGURE 5.16: Difference between the Z positions of highest and the next highest energy PS bar for a prompt event.

The requirement of contiguous bars for an event only confines it in the X–Y directions, but doesn't incorporate the closeness along the Z-axis. For this purpose the parametrization derived for timestamp to Z conversion can be utilized. The functional relation between the ΔT inside the bar to the Z position allows evaluating the position of the hits forming an event. These Z-positions calculated for each bar is compared similar to the timestamp differences of bar deposits. Figure 5.16 shows such a distribution obtained for difference in Z position from maximum to the next highest energy bar for 2 and 3 bar prompt events in the reactor ON and OFF condition. The figure 5.17 plots these differences for the 3 bar prompt events under both RON and ROFF, but for 3rd highest to

2nd highest deposit bars. The nature is similar to the timestamp difference distributions. Again a cut of selecting events within 1.5σ of the mean allows for most uncorrelated events to be filtered out.

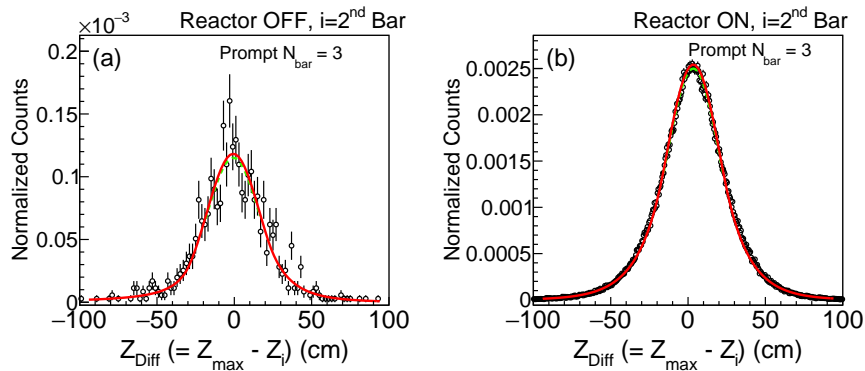


FIGURE 5.17: Difference between the Z positions of highest and the next highest energy PS bar for a prompt event.

For the delayed events only the first two hits are chosen and 1.5σ selection is employed, see figure 5.18 for the distributions obtained.

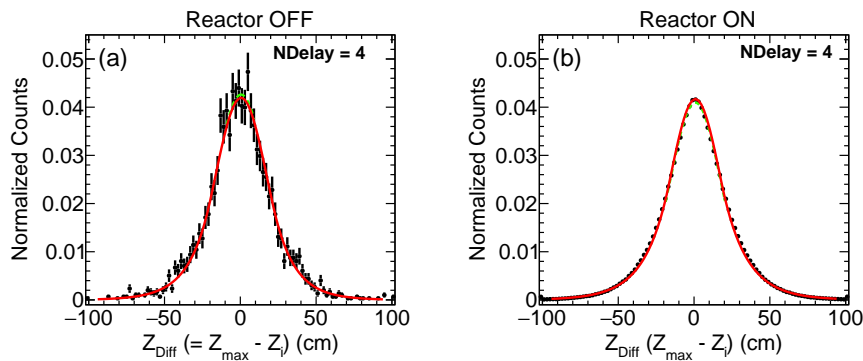


FIGURE 5.18: Difference between the Z positions of highest and the next highest energy PS bar for a 4 bar delay event.

The use of energy sorted timestamp and Z position cuts can be accompanied by cuts that utilise the energy ratios between the top bars with highest energies.

Ratio cuts differentiate the signal from background as most background which is uncorrelated has a flat ratio while for the correlated events the different shapes in the ratio may be helpful. The ratio distribution for prompt event is plotted for the first two bars (E_1/E_{\max}) and the 1st and 3rd bars ((E_2/E_{\max})) as seen in figure 5.19 and 5.20.

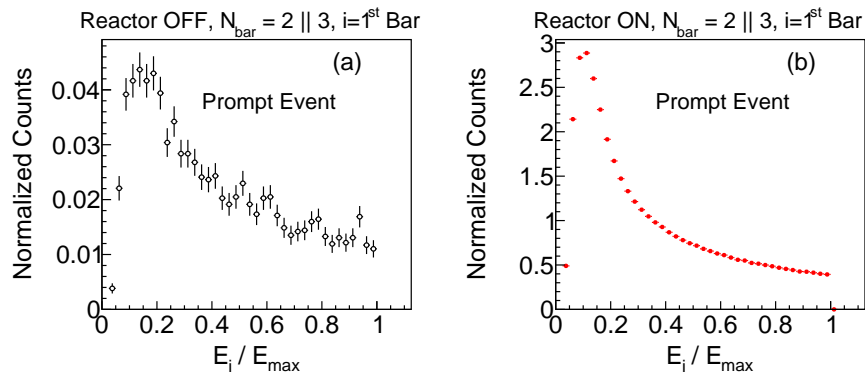


FIGURE 5.19: E_1/E_{\max} ratio for prompt events with $N_{\text{bars}}=2$ or 3.

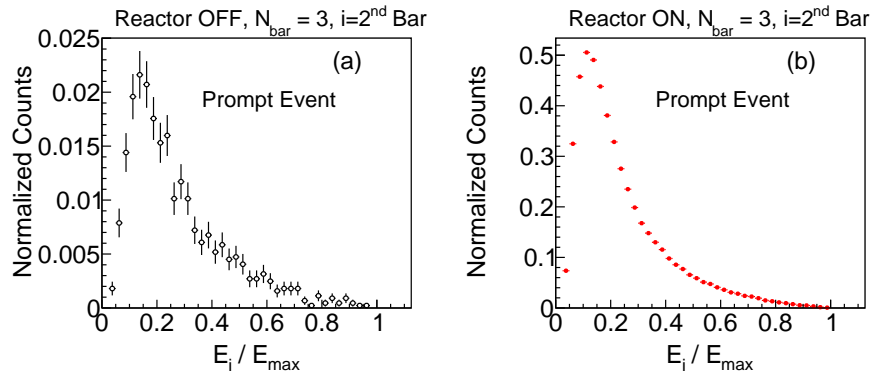


FIGURE 5.20: E_2/E_{\max} ratio for prompt events with $N_{\text{bars}}=3$.

These plots are obtained for the reactor OFF and ON conditions respectively. The poissonian rise and fall of the distribution signifies accumulation of interesting events within the first half or ratio < 0.5 cut. Hence, such a cut is also

incorporated in the selection scheme to avoid including tail events due to background. The same analysis for the first two energy bar ratio in delayed events has already been discussed in section 3.4.

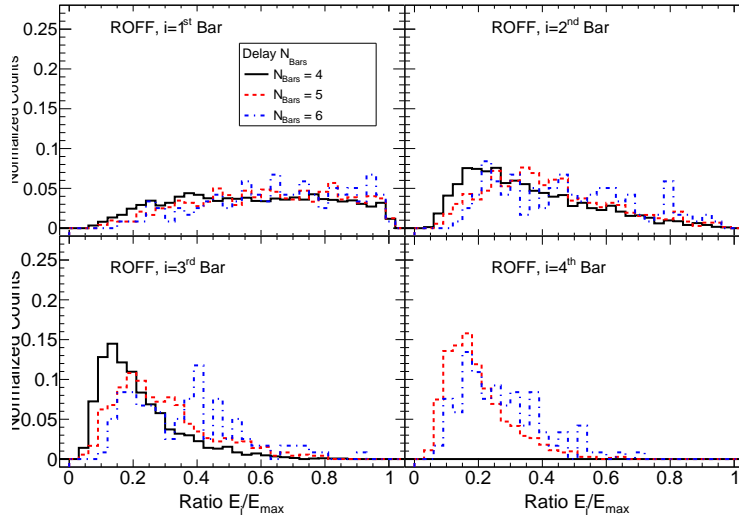


FIGURE 5.21: Ratio of all the lower energies E_1, E_2, \dots to highest energy deposit (E_{\max}) shown progressively in clockwise fashion, under reactor OFF conditions for ISMRAN delay events $N_{\text{bars}}=4, 5$ and 6.

From the comparison of the simulations with data, it has been observed that, the highest to next highest shows a slight saturation behaviour beyond 0.4 value which signifies background contributions and can be a useful distinguishing feature for putting a selection. Figure 5.21 and 5.22 show these distributions as obtained from miniISMRAN data both in reactor OFF and reactor ON. Both the figures shows a comparison of energy ratios of different bar deposits w.r.t the maximum energy deposit of a single delayed like event.

The energy ratio cut is not extended beyond the first ratio in delayed events in the analysis. With these cuts included, the timing, Z-position localization as well as energy based IBD like correlated selection are complete. Further cut i.e. the

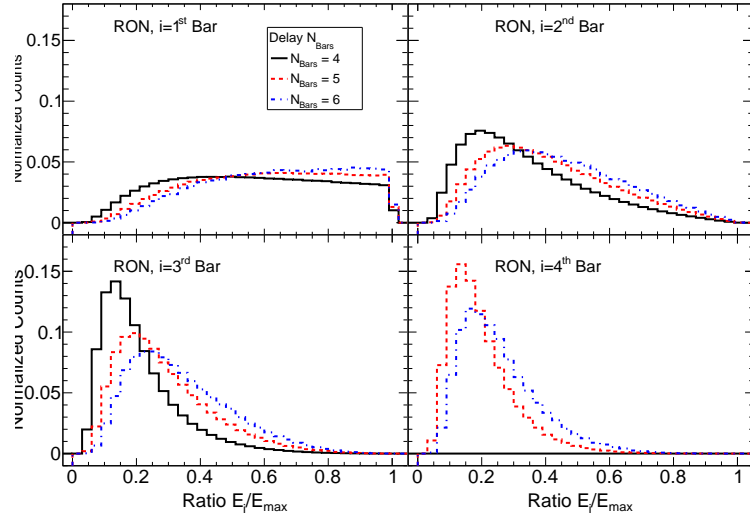


FIGURE 5.22: Ratio of all the lower energies to highest energy deposit shown progressively in clockwise fashion, under reactor ON conditions for ISMRAN delay events $N_{\text{bars}}=4,5$ and 6.

mean time delay criteria are to be applied at the selected pairs of prompt and delay events to make the final selection of $\bar{\nu}_e$ candidate events. Before moving on to signal and background separation the final filtered delayed event sum energy and N_{bars} distributions shows good agreement between simulation and data obtained for mini-ISMARAN geometry as seen in figure 5.23

5.4 Mixed event analysis

In general, the flow of selections on the first level PS bar data from miniISMARAN matrix is designed to first form a prompt event and next to look for delayed event. The time window for the pair selection is guided by the ΔT_{PD} or mean time delay between prompt and delay of $68\mu\text{s}$ obtained from pure IBD simulation (see section 3.2.1). The lower threshold of $8\mu\text{s}$ as used in cut is retained as

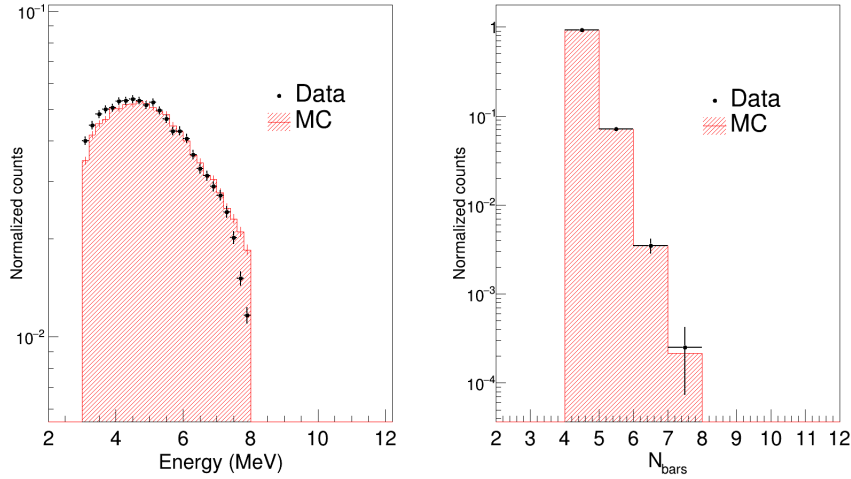


FIGURE 5.23: Comparison plot between data (symbols) and simulation (shaded region) for mini-ISMARAN delay events.

it takes care of fast decaying background like cosmic muon decay in volume. But for the upper end of the window, in general, 7 times the mean time delay value (or 7 half lives can be chosen), which is an approximation. To have a solid ground for choosing a particular IBD coincidence window a technique called the ‘mixed event analysis’ can be used. The calculation of true $\bar{\nu}_e$ count rates in miniISMARAN data requires subtraction of the background component from the combined signal and background region in the ΔT_{PD} distribution. This requires knowledge of the background region in the event distribution and also sufficient statistics to allow for lower uncertainties on the calculated rates. But due to the limited statistics from the miniISMARAN detector, the higher time delay or expected background candidate events filtered after the cuts is quite low and hence uncertainties blow up. The ‘mixed event’ technique can help by deriving the background event level by building more background statistics while keeping

the background spectral shape the same.

As the name suggests, ‘Mixed events’ involves mixing the original set of prompt and delayed events obtained from a cut based selection to create a new set of events independent of the original through a time shifting procedure. This shifting doesn’t affect the other event characteristics such as energy and multiplicity, which are untouched. To understand this shifting procedure, consider a time window big enough so that no known correlated signal and background event pairs can exceed the window. Then shift a prompt (delayed) event by this time period so as to bring it amongst an entirely new set of delayed (prompt) events. In our case this window is chosen as 1 millisecond long and the shifting is done to the prompt events. An entirely new set of correlated IBD like pairs can be formed for all prompt events which are shifted. This new set is called a ‘mixed events’ set. This procedure is repeated for time windows increasingly farther ahead, which generates newer and newer datasets. We may as well repeat the exercise using delayed events instead of prompts.

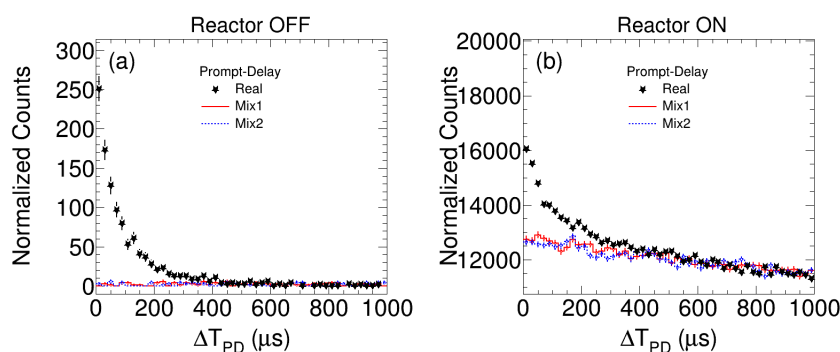


FIGURE 5.24: Prompt delay pairs ΔT_{PD} distribution from mini-ISMRRAN data in ROFF and RON overlaid with mixed event datasets

If there are still some global correlations present they cannot be attributed to

any phenomenon of interest for our detection and simply fitted with a expected background function usually a large lifetime exponential decay. The figure 5.24 shows the real or candidate IBD event ΔT_{PD} overlaid with two mixed event sets ‘Mix1’ and ‘Mix2’ to extract the uncorrelated background level in reactor OFF and ON. It is evident that in reactor OFF the mixed sets are truly flat or uniform in distribution and scale with real data beyond $500\mu s$ and we chose events beyond this mark for extracting the pure background pairs. However, in the reactor ON dataset global correlations still persist and are observed as a long lifetime exponentially decaying background. In spite of the existence of this non-uniform background, the mixed and real data set in reactor ON once again scales beyond $500\mu s$. This reassures us that the mixing technique is effective in identifying the background component.

Finally using the window of $8 < \Delta T_{PD} \mu s < 500$ time window the signal + background component is extracted and beyond which for an equal size window the pure background events are extracted. The background is then statistically subtracted from the signal + background event space. A shifting of the background window in small steps towards higher and lower side was also performed to observe its variation. The re-evaluated backgrounds from this shifting were found to be within the uncertainties.

Systematic errors in rate calculations

For the final calculations of the IBD candidate rates, the systematic error budget needs to be evaluated. In the characterization section 2.8 we saw 5% systematics due to the calibration scale. The array of cuts in analysis implicitly include

TABLE 5.2: Systematic errors at different selection levels implemented for cut based analysis

Selection cut	Error (%)
ΔT within bars	7.3
ΔZ prompt-delay	3.9
Energy ratio cuts	7.1
ΔT among bars	1.7
ΔZ among bars	5.3
Background subtraction	10.0

this uncertainty while bringing in their contributions to the final systematics. A conservative estimate of systematic errors is obtained by varying the cuts by 5% and calculating the change in the final numbers. The table 5.2 lists all the cuts and their contribution to systematic uncertainty. Using these values a final systematic error of 16 % on the IBD rate number is obtained for the cut based analysis. In addition to the above systematics, the contributions to the IBD rates in mini-ISMRRAN, coming from fast neutron backgrounds discussed earlier, are also estimated in simulation using a flat distribution of 2–12 MeV neutrons. The set of signals generated by these simulated fast neutron events are then passed through the same IBD selection cuts and it is observed that these events are selected with an efficiency of $<0.1\%$. This rate is an upper limit for fast neutrons to fake a true IBD event in mini-ISMRRAN. Other backgrounds like the long-lived cosmic ray activation products such as ${}^9\text{Li}$ and ${}^8\text{He}$ produced by cosmic muons can also produce a prompt-delay mimicking correlated background [104]. For a prototype of PANDA detector with 36 plastic scintillator –PANDA36 (3.6×10^5 g), the production rates of such isotopes has been evaluated [63]. Since, miniISMRRAN consists of PS bars of same dimensions as of PANDA, scaling of these numbers

yields rates for such isotopes in miniISMARAN as :

$${}^9\text{Li} : 3.0 \times 10^{-3} \text{ s}^{-1} \sim 116\text{day}^{-1}$$

$${}^8\text{He} : 3.0 \times 10^{-4} \text{ s}^{-1} \sim 12\text{day}^{-1}$$

PANDA36 has reported an efficiency of only 0.5% for these events, consequently the expected rates for these in miniISMARAN volume are also negligible.

5.5 Filtered IBD candidate events after cuts

The multitude of cuts described in the previous sections for the prompt as well as delayed events with the augmentation of mean time delay cut applied in both reactor OFF and ON event yields the final IBD candidate rates.

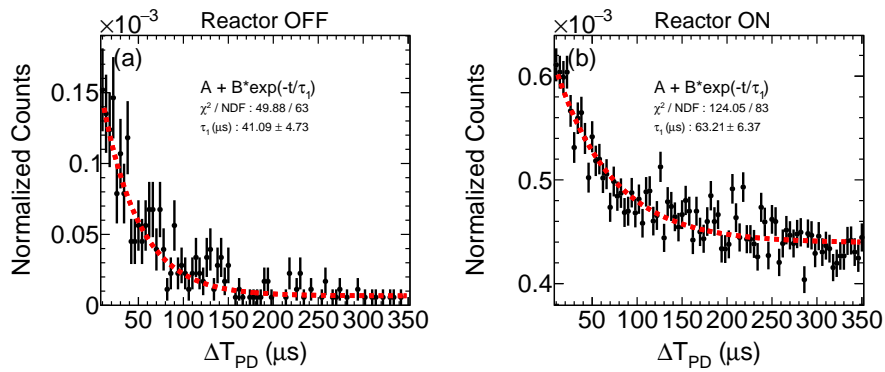


FIGURE 5.25: ΔT_{PD} for reactor ON and OFF conditions fitted with double exponential.

The statistics in both the data sets falls sharply and is about 3 orders less than the initial number of raw events. Due to the extremely small number of events obtained from final selections on miniISMARAN data and the relatively high uncorrelated background, it is preferable to have a reckoning of the the ΔT_{PD} spectral shape at an intermediate level. This is done to verify whether the

TABLE 5.3: Filtered $\bar{\nu}_e$ -like candidate events using cuts in mini-ISMRRAN reactor data.

	S + B	B	(S + B) - B	Prediction
March: ROFF(~22 days)	$8.0 \pm 2.8(\text{stat})$	$1.0 \pm 1.0(\text{stat})$	$7.0 \pm 3.0 \pm 1.1$	–
June: RON(~28 days)	$444.0 \pm 21.1(\text{stat})$	$389.0 \pm 19.7(\text{stat})$	$55.0 \pm 28.9(\text{stat}) \pm 8.6(\text{sys})$	57.0 ± 5.0
ROFF(~2 days)	$4.0 \pm 2.0(\text{stat})$	$3.0 \pm 1.7(\text{stat})$	$1.0 \pm 2.6(\text{stat}) \pm 1.2(\text{sys})$	
November: RON(~27 days)	$484.0 \pm 22.0(\text{stat})$	$429.0 \pm 20.7(\text{stat})$	$55.0 \pm 30.2(\text{stat}) \pm 9.0(\text{sys})$	57.0 ± 5.0
ROFF(~3 days)	$3.0 \pm 1.7(\text{stat})$	$1.0 \pm 1.0(\text{stat})$	$2.0 \pm 2.0(\text{stat}) \pm 1.1(\text{sys})$	
December: RON(~23 days)	$268.0 \pm 16.4(\text{stat})$	$225.0 \pm 15.0(\text{stat})$	$43.0 \pm 22.2(\text{stat}) \pm 6.9(\text{sys})$	46.0 ± 4.0
ROFF(~8 days)	$5.0 \pm 2.2(\text{stat})$	$1.0 \pm 1.0(\text{stat})$	$4.0 \pm 2.4(\text{stat}) \pm 0.9(\text{sys})$	

progressively tight selections are preserving the spectral shape and hence don't deviate from the true IBD events. The panel (a) and (b) of the figure 5.25 show these ΔT_{PD} distributions. A fit to the exponential distributions yields a value of $\sim 63\mu\text{s}$ in reactor ON, not far-off from the $68\mu\text{s}$ value obtained in simulations. Also the reactor OFF data doesn't show a smaller decay time ($41\mu\text{s}$) than reactor ON, indicating some background only source.

Finally, the $\bar{\nu}_e$ -like events, for the 4 different months, using all the cuts are as tabulated in table 5.3. The integral counts in the signal(S) plus background(B) region i.e. S + B is first obtained and then the background component is subtracted to yield the final number of events. The statistical errors quoted are due to quadrature sum of the errors in the counts for the S+B and B region. The systematics are calculated using the 16% error obtained earlier and the same is used in reactor OFF as an upper limit on error although reactor OFF data is expected to suffer from less background. The march month data had complete shutdown with negligible activity due to maintenance operations at reactor and therefore show much less counts relative to other service shutdowns. The IBD like events obtained after the cuts are compared with the theoretical prediction listed in the last column of the table. These are calculated using the formula 2.1 presented

in the section 2.3 using reactor power, detector volume, distance and average interaction cross-section. The predicted values, therefore, are not simulation results since such an estimate will require background modelling which is yet to be performed. The uncertainties mentioned for the prediction are small as they only account for systematics due to errors in reactor power reading and those from cross-section values and not for fuel fraction and core geometry induced uncertainties.

5.6 Summary

The miniISMARAN setup provides a useful opportunity to evaluate the performance as well as physics reach of the ISMRAN setup. The setup has been used to quantify the background, both natural as well as in reactor conditions. The reactor background cumulative rates observed inside the full ISMRAN shielding are reduced by 3 orders of magnitude as compared to the unshielded setup. The measurements both with the PS bar, efficient γ -ray detector— CeBr_3 show a high γ -ray activity up to about 2.4 MeV. The fast neutron rate from a 5” liquid scintillator gives an estimated 10^{-6} Hz cm^{-2} of such events at the reactor site for the given thresholds. The PS bar background energy spectrum shows a shoulder above 2 MeV to 7 MeV where the $\bar{\nu}_e$ events of interest lie.

About a month long uninterrupted run of miniISMARAN at ~ 13 m distance was conducted for 4 different months. miniISMARAN collected data for a complete shutdown in the month of March 2018 and in reactor ON and OFF in June, November and December 2018 at an average power ranging from 60–80 MW. This data has been extensively analysed using various selection cuts inspired by

simulations performed for the ISMRAN setup. The cuts cover all the aspects such as event sum energy, bar multiplicity, topology of the event, closeness in time, energy distribution among the bars etc. Successive application of these cuts filters out much of the background. Also, with implementation of mixed event analysis, the level of background could be quantified. This allowed for calculating the potential IBD candidates from miniISMARAN data. The numbers obtained suffer heavily from statistical errors much higher than the expected systematics.

Chapter 6

Conclusions

Neutrinos make important tools for probing nuclear activity remotely, especially, for monitoring nuclear reactor cores. They can also act as messenger particles for probing otherwise inaccessible physical phenomena like supernovae, AGNs and GRBs. Additionally, some unsolved problems still exist in the neutrino physics sector such as existence of sterile counterparts of known neutrinos, the mass hierarchy of the neutrino mass eigenstates, whether neutrinos are Dirac or majorana fermions etc. To host such detection setups, nuclear reactors provide an ideal environment due to their high $\bar{\nu}_e$ s flux and controlled operation.

The ISMRAN experiment at Dhruva reactor facility of BARC, India, is a one of the efforts in this area. It is proposed for monitoring the natural uranium core of Dhruva using non-hazardous plastic scintillator volume of moderate scale.

The experiment has made substantial progress, with completion of a number of different activities for its development.

6.1 Studies of $\bar{\nu}_e$ using ISMRAN

Characterization of PS

The plastic scintillators used to form the ISMRAN matrix have been characterized for their energy and timing response. Detailed studies using known radioactive sources and natural background have been carried out for spectral matching of the PMTs and also globally amongst the different PS bars. The calibration derived for each PS shows a linear energy response over a broad scale ranging up to 20 MeV (cosmic muon). The presence of double ended PMT readout is useful to leverage the timing information from both and infer the timing and Z position. Parametrization for the timing to Z position conversion have been calculated. A data-taking exercise using known correlated γ -ray source ^{60}Co shows faithful reconstruction of its events and also points to use of sum energy and bar multiplicity or N_{bars} as event variables to select IBD events in the ISMRAN segmented volume.

6.2 Simulations in ISMRAN geometry

The plastic scintillator volume comprising of individual PS bars is replicated in monte-carlo simulations and IBD events are generated and transported using the GEANT4 simulation package. The reference spectrum and various parametrization and cross-section calculations are taken from known LEU phenomenology

analyses as part of references [80, 79, 48, 81]. These are used as the inputs to generate the IBD event and then standard kinematics derives the daughter product energies. The resulting event signatures are separately evaluated for prompt positron and delayed neutron for their sum energy and N_{bars} signature. The event detection efficiencies are evaluated from the simulated events using these variables.

Due to the requirement of in situ calibration, the matrix may have to be reduced to 9×10 and the remaining width can be divided into the gaps between bar columns. Although, the reduced volume will roughly reduce the $\bar{\nu}_e$ detection rates by 10% the events interacting are found to be detected with only 1% drop in efficiency even in the modified geometry with gaps.

6.3 Using MLP for improved detection efficiency

Machine learning has been gaining increased popularity among HEP community for filtering signal events from background dominated samples, especially in collider experiments. Although the neutrino detection process is not as dynamic and lacks direct trigger information as in colliders, the task of looking for specific tracking or energy signatures which are mimicked by other backgrounds is the same. ISMRAN aims to adopt the power of machine learning to filter signal events as the DAQ system uses only minimum thresholds for online triggering and records much of the raw data for possibly complex and involved analysis needed for $\bar{\nu}_e$ detection.

Using a standard feed-forward ANN in the form of a multi-layer perceptron (MLP) having two hidden layers and the capability for Bayesian error correction

(MLPBNN), a highly efficient prompt event classification is shown to be possible for the full ISMRAN volume. As part of this process, a new and effective variable – D_k is devised, which is a weighted combination of both the base variables sum energy and N_{bars} . This framework yields about 91% efficient classification data with close to 73% pure output sample. This is a positive sign for the ISMRAN setup as it suffer from huge efficiency losses when only cut based analysis is considered.

6.4 Analysis results from the prototype - miniISMRAN

The prototype detector – miniISMRAN, which is a 16 PS bar matrix, is a precursor to the ISMRAN detector. This prototype serves as a test bed for the full detector operation as it allows for formalizing and streamlining of the various procedures to be adopted for setting up of ISMRAN. Operation of this prototype in the reactor environment for long duration with minimal personnel supervision has established the suitability of a near-field detector like ISMRAN for long-term unmanned operation inside the reactor hall. An elaborate background measurement campaign has been carried out both in laboratory and reactor environments with miniISMRAN matrix. A detailed analysis framework has been developed to extract the IBD candidate events and their rates in the miniISMRAN data are also calculated.

Chapter 7

Outlook

7.1 Full scale ISMRAN detector

At the time of writing this thesis, a stack of 90 scintillators has been characterized in the laboratory. A 9×10 matrix with required DAQ comprised of an array of CAEN V1730 digitizers and HV modules are in operation for taking cosmogenic background data 7.1. About 25 tons of Pb in the form of chevron and flat shaped bricks has been procured. Borated polyethylene sheets to cover all sides of the ISMRAN $1m^3$ volume will be arriving soon. The shielding structure has been fabricated and its testing with Pb bricks and existing BP sheets is underway at the Center for Design and Manufacture (CDM).

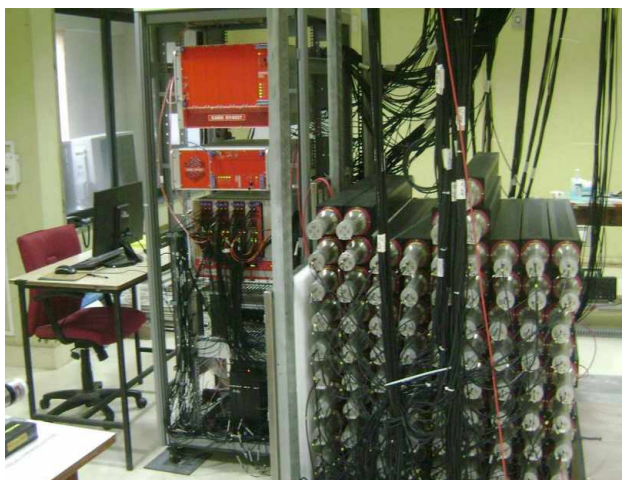


FIGURE 7.1: The scaled up 9×9 PS matrix recording cosmic background in laboratory.

7.2 Extracting neutrino spectrum

Simulations to obtain the expected neutrino flux needs to be performed for the Dhruva core. Determining the burn-up process (fuel evolution) for a natural Uranium core would be a novel study. The result of this study will provide the exact spectral input for improving the accuracy of ISMRAN simulations and to test its suitability for estimating the plutonium build-up. On the measurement side, the efforts will be directed towards extracting the $\bar{\nu}_e$ spectrum for the Dhruva core from analysis of the dataset generated by the full ISMRAN setup operation in reactor.

7.3 Detection technology

As already pointed out, the homogeneous doping, bulk volume design and the possibility of fast neutron ID in liquid scintillator detectors makes them an ideal choice in terms of detection of IBD. On the other hand, plastic scintillators offer

the option of building a non-hazardous and convenient assembly of detectors suitable for antineutrino based monitoring of nuclear reactors at close distances. Since, ISMRAN is already using the plastics, it is worth exploring the bulk liquid scintillator design in larger volumes for moderate baseline (30–50 m) neutrino detection, from outside the reactor complex. First steps in this direction are already being initiated in collaboration with the Chemistry division at BARC.

Even the plastic scintillators that ISMRAN currently uses are of commercial make and don't offer much in terms of precision detection abilities. Also, scaling the existing volume of ISMRAN or building more identical modules calls for in-house capability development of plastic scintillators. This aspect is also being explored at BARC.

The development of ASIC chips and other electronics which can enhance the capabilities of ISMRAN but are not yet developed or available for procurement are also being explored.

7.4 New physics

Many reactor neutrino experiments have reported the observation of a spectral distortion in 4-7 MeV region of the reconstructed antineutrino spectra called the '5 MeV bump', as the distortion peaks at 5 MeV. This has triggered a new search for the source of this distortion. In the long term, once the proof-of-principle neutrino detection is demonstrated, ISMRAN can aim to address such issues either through a bigger detector or more precise detection techniques. The sensitivity of ISMRAN to the sterile neutrino detection is already shown possible in the simulations, and with some additional analysis, probing the 5 MeV bump

is also within reach. This exercise is particularly interesting again owing to the natural Uranium core of Dhruva offering a new data point in the global analysis.

7.5 Potential reactor sites

PFBR at IGCAR Kalpakkam

In the context of probing novel reactor cores for monitoring, sterile searches and looking for spectral distortions the 'Prototype fast breeder reactor (PFBR) at IGCAR institute in Kalpakkam, Tamil nadu provides an interesting avenue. The prototype reactor core uses a purely plutonium core and hence offers an opportunity to understand the above physics in a novel reactor core fuel assembly. The higher power rating – $1.5 \text{ GW}_{\text{th}}$ will allow higher event rates ~ 225 events per day for a moderate stand-off of ~ 30 m if inside hall operation is to be avoided.

Power reactors at Kudankulam

A more natural and convenient progression for ISMRAN experiment will be to move to a power reactor site offering higher event rates as compared to Dhruva. The Kudankulam Nuclear Power Plant (KNPP) offers such a venue with its planned 6 LWR units. Unit 1 and 2 had already been commissioned with each having a power output of $\sim 3\text{GW}_{\text{th}}$ providing for a possible event rate of about 900 events per day at equal standoff of 30 m from each core.

The operation at both the PFBR and KNPP sites is envisaged outside the reactor complex and hence reactor background will not be a problem, while, at the same time offering reasonable event rates. This is a promising scheme worth

exploring for ISMRAN in the long term.

Bibliography

- [1] Wolfgang Pauli (1930). Typed copy. URL: <http://cds.cern.ch/record/83282> (cit. on p. 43).
- [2] James Chadwick. *Proc. R. Soc. Lond. A* (1932). URL: <https://royalsocietypublishing.org/doi/10.1098/rspa.1932.0112> (cit. on p. 43).
- [3] E. Fermi. *Il Nuovo Cimento* 11 (1 1934) (cit. on p. 44).
- [4] *What Is The Standard Model of Particle Physics?* (2018). URL: <https://www.sciencealert.com/the-standard-model> (cit. on p. 44).
- [5] Peter W. Higgs. *Phys. Rev. Lett.* 13 (16 Oct. 1964), pp. 508–509. URL: <https://link.aps.org/doi/10.1103/PhysRevLett.13.508> (cit. on p. 45).
- [6] F. Englert and R. Brout. *Phys. Rev. Lett.* 13 (9 Aug. 1964), pp. 321–323. URL: <https://link.aps.org/doi/10.1103/PhysRevLett.13.321> (cit. on p. 45).

- [7] G. S. Guralnik, C. R. Hagen, and T. W. B. Kibble. *Phys. Rev. Lett.* 13 (20 Nov. 1964), pp. 585–587. URL: <https://link.aps.org/doi/10.1103/PhysRevLett.13.585> (cit. on p. 45).
- [8] G. Aad et. al. *Physics Letters B* 716.1 (0370-2693 2012), pp. 1–29. URL: <http://www.sciencedirect.com/science/article/pii/S037026931200857X> (cit. on p. 45).
- [9] S. Chatrchyan et. al. *Physics Letters B* 716.1 (0370-2693 2012), pp. 30–61. URL: <http://www.sciencedirect.com/science/article/pii/S0370269312008581> (cit. on p. 45).
- [10] J. C. Street and E. C. Stevenson. *Phys. Rev.* 52 (9 Nov. 1937), pp. 1003–1004. URL: <https://link.aps.org/doi/10.1103/PhysRev.52.1003> (cit. on p. 45).
- [11] Seth H. Neddermeyer and Carl D. Anderson. *Phys. Rev.* 51 (10 May 1937), pp. 884–886. URL: <https://link.aps.org/doi/10.1103/PhysRev.51.884> (cit. on pp. 45, 56).
- [12] Arthur et. al Loureiro. *Phys. Rev. Lett.* 123 (8 Aug. 2019), p. 081301. URL: <https://link.aps.org/doi/10.1103/PhysRevLett.123.081301> (cit. on p. 46).
- [13] Christian Spiering. *The European Physical Journal H* 37 (Aug. 2012), pp. 515–565. URL: <https://doi.org/10.1140/epjh/e2012-30014-2> (cit. on p. 47).
- [14] M.R. Krishnaswamy et al. *Phys. Lett. B* 57 (1975), pp. 105–108 (cit. on p. 49).

- [15] Thomas K Gaisser. *Physica Scripta* T121 (Jan. 2005), pp. 51–56. URL: <https://doi.org/10.1088/0954-3899/121/1/007> (cit. on p. 49).
- [16] Kumar. A et. al. *Pramana - J Phys* 79 (Apr. 2017). URL: <https://doi.org/10.1007/s12043-017-1373-4> (cit. on p. 49).
- [17] W. David Arnett et al. *Annual Review of Astronomy and Astrophysics* 27.1 (1989), pp. 629–700. URL: <https://doi.org/10.1146/annurev.aa.27.090189.003213> (cit. on p. 50).
- [18] M.G. Aartsen et. al. *Journal of Instrumentation* 12.03 (Mar. 2017), P03012–P03012. URL: <https://doi.org/10.1088/1748-0221/12/03/P03012> (cit. on pp. 51, 77, 78).
- [19] George W. Rodeback and James S. Allen. *Phys. Rev.* 86 (4 May 1952), pp. 446–450. URL: <https://link.aps.org/doi/10.1103/PhysRev.86.446> (cit. on p. 53).
- [20] M. Goldhaber, L. Grodzins, and A. W. Sunyar. *Phys. Rev.* 109 (3 Feb. 1958), pp. 1015–1017. URL: <https://link.aps.org/doi/10.1103/PhysRev.109.1015> (cit. on p. 54).
- [21] C. L. Cowan et al. *Science* 124.3212 (1956), pp. 103–104. URL: <https://science.sciencemag.org/content/124/3212/103> (cit. on p. 54).
- [22] *Los Alamos Science* (1997). URL: <https://permalink.lanl.gov/object/tr?what=info:lanl-repo/lareport/LA-UR-97-2534-02> (cit. on p. 55).

- [23] G. Danby et al. *Phys. Rev. Lett.* 9 (July 1962), pp. 36–44. URL: <https://link.aps.org/doi/10.1103/PhysRevLett.9.36> (cit. on p. 56).
- [24] Martin L. Perl. *NATO Sci. Ser. B* 352 (1996). Ed. by Harvey B. Newman and Thomas Ypsilantis, pp. 277–302 (cit. on p. 57).
- [25] K. Kodama et al. *Phys. Lett. B* 504 (2001), pp. 218–224 (cit. on p. 57).
- [26] J. N. Bahcall and M. Cribier. *Inside the Sun*. Ed. by Gabrielle Berthomieu and Michel Cribier. Springer Netherlands, 1990, pp. 21–41 (cit. on p. 58).
- [27] Bruce T. Cleveland et. al. *The Astrophysical Journal* 496 (1 Oct. 1997), p. 505. URL: <https://iopscience.iop.org/article/10.1086/305343> (cit. on p. 58).
- [28] Y. et. al Fukuda. *Phys. Rev. Lett.* 77 (9 Aug. 1996), pp. 1683–1686. URL: <https://link.aps.org/doi/10.1103/PhysRevLett.77.1683> (cit. on p. 59).
- [29] J.N. Abdurashitov et. al. *Physics Letters B* 328.1 (1994), pp. 234–248. URL: <http://www.sciencedirect.com/science/article/pii/0370269394904545> (cit. on p. 60).
- [30] M. Cribier et. al. *Nuclear Physics B - Proceedings Supplements* 70.1 (1999). Proceedings of the Fifth International Workshop on topics in Astroparticle and Underground Physics, pp. 284–291. URL: <http://www.sciencedirect.com/science/article/pii/S0920563298004381> (cit. on p. 60).
- [31] Nick Jelley, Arthur B. McDonald, and R.G. Hamish Robertson. *Annual Review of Nuclear and Particle Science* 59.1 (2009), pp. 431–465. URL:

- <https://doi.org/10.1146/annurev.nucl.55.090704.151550>
(cit. on p. 60).
- [32] Q. R. et. al Ahmad. *Phys. Rev. Lett.* 89 (1 June 2002), p. 011301. URL: <https://link.aps.org/doi/10.1103/PhysRevLett.89.011301>
(cit. on p. 61).
- [33] T.J. Haines et al. *Phys. Rev. Lett.* 57 (1986), pp. 1986–1989 (cit. on p. 61).
- [34] K.S. Hirata et al. (Mar. 1988). Ed. by J. Tran Thanh Van, pp. 235–246
(cit. on p. 61).
- [35] T. Kajitaa, E. Kearns, and Super-Kamiokande Collaboration M. Shiozawa. *Nuclear Physics B* 908 (2016), pp. 14–29. URL: <https://doi.org/10.1016/j.nuclphysb.2016.04.017> (cit. on p. 62).
- [36] Y. et. al. Ashie. *Phys. Rev. Lett.* 93 (10 Sept. 2004), p. 101801. URL: <https://link.aps.org/doi/10.1103/PhysRevLett.93.101801>
(cit. on p. 63).
- [37] B. Pontecorvo. *JETP* 6 (2 Feb. 1958), p. 429. URL: <http://www.jetp.ac.ru/cgi-bin/e/index/e/6/2/p429?a=list> (cit. on p. 63).
- [38] Ziro Maki, Masami Nakagawa, and Shoichi Sakata. *Progress of Theoretical Physics* 28.5 (Nov. 1962), pp. 870–880. eprint: <https://academic.oup.com/ptp/article-pdf/28/5/870/5258750/28-5-870.pdf>. URL: <https://doi.org/10.1143/PTP.28.870> (cit. on p. 63).
- [39] L. Wolfenstein. *Phys. Rev. D* 17 (9 May 1978), pp. 2369–2374. URL: <https://link.aps.org/doi/10.1103/PhysRevD.17.2369> (cit. on p. 66).

- [40] S.P. Mikheyev and A. Yu. Smirnov. *Sov. J. Nucl. Phys.* 42 (1985), pp. 913–917 (cit. on p. 66).
- [41] Robert-Jan Hagebout (2014). URL: <https://pdfs.semanticscholar.org/71c5/6cfa54418b8e5d37c209a8df55d3360caf8c.pdf> (cit. on p. 67).
- [42] E. Majorana. *Nuovo Cimento* 14 (171 1937) (cit. on p. 68).
- [43] *Physics Reports* 427.5 (2006), pp. 257–454. URL: <http://www.sciencedirect.com/science/article/pii/S0370157305005119> (cit. on p. 68).
- [44] *Physics Reports* 427.5 (2006), pp. 257–454. URL: <http://www.sciencedirect.com/science/article/pii/S0370157305005119> (cit. on p. 68).
- [45] A. et. al Aguilar. *Phys. Rev. D* 64 (11 Nov. 2001), p. 112007. URL: <https://link.aps.org/doi/10.1103/PhysRevD.64.112007> (cit. on p. 69).
- [46] B. Bodmann et. al. *Nuclear Physics B - Proceedings Supplements* 31 (1993), pp. 301–306. URL: <http://www.sciencedirect.com/science/article/pii/0920563293901505> (cit. on p. 69).
- [47] Aguilar-Arevalo et. al. *Phys. Rev. Lett.* 121 (22 Nov. 2018), p. 221801. URL: <https://link.aps.org/doi/10.1103/PhysRevLett.121.221801> (cit. on p. 70).
- [48] G. Mention et. al. *Phys. Rev. D* 83 (2011), p. 073006. URL: <https://link.aps.org/doi/10.1103/PhysRevD.83.073006> (cit. on pp. 70, 139, 235).

- [49] Y.J. Ko et al. *Phys. Rev. Lett.* 118 (12 Mar. 2017), p. 121802. URL: <https://link.aps.org/doi/10.1103/PhysRevLett.118.121802> (cit. on p. 71).
- [50] A. P. Serebrov et al. *JETP Letters* 109 (4 Feb. 2019), pp. 213–221. URL: <https://doi.org/10.1134/S0021364019040040> (cit. on p. 72).
- [51] J. et. al. Ashenfelter. *Phys. Rev. Lett.* 121 (25 Dec. 2018), p. 251802. URL: <https://link.aps.org/doi/10.1103/PhysRevLett.121.251802> (cit. on p. 72).
- [52] I. Alekseev et al. *Journal of Instrumentation* 11.11 (2016), P11011. URL: <http://stacks.iop.org/1748-0221/11/i=11/a=P11011> (cit. on p. 72).
- [53] Y. Abreu et. al. *Journal of Instrumentation* 13.05 (May 2018), P05005–P05005. URL: <https://doi.org/10.1088/1748-0221/13/05/P05005> (cit. on pp. 72, 73).
- [54] Patrick Huber. *Phys. Rev. Lett.* 118 (4 Jan. 2017), p. 042502. URL: <https://link.aps.org/doi/10.1103/PhysRevLett.118.042502> (cit. on p. 75).
- [55] L. A. Mikaelyan. *Proceedings of the International Conference "Neutrino 77", Nauka, Moscow 2 (1978)*, pp. 383–385 (cit. on pp. 79, 80).
- [56] Yu. V. Klimov et al. *Atomic Energy* 76.2 (Feb. 1994), pp. 123–127. URL: <https://doi.org/10.1007/BF02414355> (cit. on pp. 79, 95).

- [57] A. Bernstein et al. *Journal of Applied Physics* 91 (Mar. 2002), p. 4672. URL: <https://aip.scitation.org/doi/10.1063/1.1452775#> (cit. on p. 79).
- [58] N.S. Bowden et al. *Nuclear Instruments and Methods in Physics Research Section A: Accelerators, Spectrometers, Detectors and Associated Equipment* 572.2 (2007), pp. 985–998. URL: <http://www.sciencedirect.com/science/article/pii/S0168900206024326> (cit. on p. 81).
- [59] Andi S. Cucoanes. *J. Phys. Conf. Ser.* 375 (2012). Ed. by Lothar Oberauer, Georg Raffelt, and Robert Wagner, p. 042063 (cit. on p. 82).
- [60] A. Porta et al. *Nuclear Instruments and Methods in Physics Research Section A: Accelerators, Spectrometers, Detectors and Associated Equipment* (June 2009), pp. 1–8 (cit. on p. 81).
- [61] M. Askins et al. (Feb. 2015). arXiv: 1502.01132 [physics.ins-det] (cit. on p. 82).
- [62] Y. Kuroda et al. *Nuclear Instruments and Methods in Physics Research Section A: Accelerators, Spectrometers, Detectors and Associated Equipment* 690 (2012), pp. 41–47. URL: <http://www.sciencedirect.com/science/article/pii/S0168900212007061> (cit. on p. 83).
- [63] S. Oguri et al. *Nuclear Instruments and Methods in Physics Research Section A: Accelerators, Spectrometers, Detectors and Associated Equipment* 757 (2014), pp. 33–39. URL: <http://www.sciencedirect.com/science/article/pii/S0168900214004781> (cit. on pp. 84, 228).
- [64] IAEA (2008). URL: <https://www.lefigaro.fr/assets/pdf/AIEA-neutrino.pdf> (cit. on p. 89).

- [65] D. Mulmule et. al. *Nuclear Instruments and Methods in Physics Research Section A: Accelerators, Spectrometers, Detectors and Associated Equipment* 911 (2018), pp. 104–114. URL: <http://www.sciencedirect.com/science/article/pii/S0168900218313408> (cit. on pp. 90, 135).
- [66] S.K. Agarwal et al. *Nuclear Engineering and Design* 236 (2006), pp. 747–757. URL: <https://www.sciencedirect.com/science/article/pii/S0029549306000732?via%5C%3Dihub> (cit. on pp. 90, 92).
- [67] (2020). URL: <http://barc.gov.in/reactor/index.html> (cit. on p. 93).
- [68] (). URL: <https://eljentechnology.com/products/plastic-scintillators/ej-200-ej-204-ej-208-ej-212> (cit. on pp. 97, 98, 137).
- [69] (). URL: <http://et-enterprises.com/products/photomultipliers/product/p9305kb-series> (cit. on pp. 98, 99).
- [70] (). URL: <https://www.caen.it/products/v1730/> (cit. on pp. 103, 105).
- [71] (). URL: <https://www.caen.it/?downloadfile=5724> (cit. on p. 104).
- [72] (2020). URL: <https://www.caen.it/> (cit. on p. 110).
- [73] S. Agostinelli et. al. *Nuclear Instruments and Methods in Physics Research Section A: Accelerators, Spectrometers, Detectors and Associated*

- Equipment* 506.3 (2003), pp. 250–303. URL: <http://www.sciencedirect.com/science/article/pii/S0168900203013688> (cit. on p. 135).
- [74] V.I. Tretyak. *Astroparticle Physics* 33.1 (2010), pp. 40–53. URL: <http://www.sciencedirect.com/science/article/pii/S0927650509001650> (cit. on p. 137).
- [75] Dennis H. et. al. Wright. *AIP Conf. Proc.* 896.1 (2007). Ed. by M. Albrow and R. Raja, pp. 11–20 (cit. on p. 137).
- [76] P. Vogel, L.J. Wen, and C. Zhang. *Nature Communications* 6.3 (2015), p. 6935. URL: <https://doi.org/10.1038/ncomms7935> (cit. on p. 138).
- [77] F. P. et. al. *An. Chinese Physics C* 41 (July 2016) (cit. on p. 140).
- [78] Yeongduk Kim. *Nuclear Engineering and Technology* 48.2 (2016), pp. 285–292. URL: <http://www.sciencedirect.com/science/article/pii/S1738573316000498> (cit. on p. 140).
- [79] L. Zhan et. al. *Phys. Rev. D* 78 (11 2008), p. 111103. URL: <https://link.aps.org/doi/10.1103/PhysRevD.78.111103> (cit. on pp. 139, 235).
- [80] Th. A. et. al. Mueller. *Phys. Rev. C* 83 (5 2011), p. 054615. URL: <https://link.aps.org/doi/10.1103/PhysRevC.83.054615> (cit. on pp. 139, 235).
- [81] P. Vogel. *Phys. Rev. D* 29 (9 1984), pp. 1918–1922. URL: <https://link.aps.org/doi/10.1103/PhysRevD.29.1918> (cit. on pp. 139, 235).

- [82] P Goldhagen et al. *Nuclear instruments and methods in physics research. Section A, Accelerators, spectrometers, detectors and associated equipment* 476 (Feb. 2002), pp. 42–51 (cit. on pp. 143, 170, 204).
- [83] N.S. Bowden, M. Sweany, and S. Dazeley. *Nuclear Instruments and Methods in Physics Research Section A: Accelerators, Spectrometers, Detectors and Associated Equipment* 693 (2012), pp. 209–214. URL: <http://www.sciencedirect.com/science/article/pii/S0168900212007528> (cit. on p. 154).
- [84] T et. al. Tanaka. *Progress of Theoretical and Experimental Physics* 2020.4 (Apr. 2020). URL: <https://doi.org/10.1093/ptep/ptaa015> (cit. on p. 162).
- [85] K et. al Hagiwara. *Progress of Theoretical and Experimental Physics* 2019.2 (Feb. 2019). URL: <https://doi.org/10.1093/ptep/ptz002> (cit. on p. 162).
- [86] Chris Hagmann, David Lange, and Doug Wright. *2007 IEEE Nuclear Science Symposium Conference Record 2* (2007), pp. 1143–1146 (cit. on p. 171).
- [87] Michael Kagan. *CERN Academic Training Lecture Regular Programme, April 2017 (Machine Learning)* (). URL: <https://indico.cern.ch/event/619370/> (cit. on p. 177).
- [88] Bishop C. *Springer book* (2006). URL: <https://www.springer.com/gp/book/9780387310732> (cit. on p. 178).
- [89] F. Rosenblatt. *Spartan books* (1961) (cit. on p. 178).

- [90] R. Reed and R. Marks. *Bradford Books ed.* (1999) (cit. on p. 178).
- [91] M. Stinchcombe K. Hornik and H. White. *Neural Networks* 2 (5 1989), pp. 359–366. URL: [https://doi.org/10.1016/0893-6080\(89\)90020-8](https://doi.org/10.1016/0893-6080(89)90020-8) (cit. on p. 178).
- [92] G. Cybenko. *Math. Control Signals Systems* 2 (1989), p. 303. URL: <https://doi.org/10.1007/BF02551274> (cit. on p. 178).
- [93] Yufeng G. *towards data science – A medium publication* (Sept. 2017). URL: <https://towardsdatascience.com/the-7-steps-of-machine-learning-2877d7e5548e> (cit. on p. 179).
- [94] (2020). URL: <https://root.cern.ch/tmva> (cit. on p. 181).
- [95] R. A. Fisher. *Annals of Eugenics* 7 (1936), pp. 179–188. URL: <https://doi.org/10.1111/j.1469-1809.1936.tb02137.x> (cit. on p. 181).
- [96] Corinna Cortes and Vladimir Vapnik. *Machine Learning* 20 (3 1995), pp. 273–297. URL: <https://doi.org/10.1007/BF00994018> (cit. on p. 181).
- [97] Wu. Xindong et. al. *Knowledge and Information Systems* 14 (1 2008), pp. 1–37. URL: <https://doi.org/10.1007/s10115-007-0114-2> (cit. on p. 181).
- [98] D. Mulmule et al. *Journal of Instrumentation* 15 (4 2020), P04021–P04021. URL: <https://doi.org/10.1088/1748-0221/15/04/P04021> (cit. on p. 183).

- [99] A. Aurisano et. al. *Journal of Instrumentation* 11 (2016). URL: <https://doi.org/10.1088/1748-0221/11/09/P09001> (cit. on p. 185).
- [100] Tom Fawcett. *Pattern Recognition Letters* 27.8 (2006). ROC Analysis in Pattern Recognition, pp. 861–874. URL: <http://www.sciencedirect.com/science/article/pii/S016786550500303X> (cit. on p. 186).
- [101] Jason Gallicchio and Matthew D. Schwartz. *Journal of High Energy Physics* 2013.90 (2013). URL: [https://doi.org/10.1007/JHEP04\(2013\)090](https://doi.org/10.1007/JHEP04(2013)090) (cit. on p. 189).
- [102] J. Ashenfelter et. al. *Nuclear Instruments and Methods in Physics Research Section A: Accelerators, Spectrometers, Detectors and Associated Equipment* 806 (2016), pp. 401–419. URL: <http://www.sciencedirect.com/science/article/pii/S0168900215012309> (cit. on p. 193).
- [103] G. Knoll. *John Wiley and Sons, Inc* (2000) (cit. on p. 204).
- [104] S. et. al. Abe. *Phys. Rev. C* 81 (2 Feb. 2010), p. 025807. URL: <https://link.aps.org/doi/10.1103/PhysRevC.81.025807> (cit. on pp. 205, 228).

Thesis Highlight

Name of the Student: Dhruv Mulmule

Name of the CI/OCC: BARC

Enrolment No.: PHYS01201504023

Thesis Title: Studies of reactor anti-neutrinos with ISMRAN

Discipline: Physical Sciences

Sub-Area of Discipline: Neutrino Physics

Date of viva voce: 14/01/2021

Indian Scintillator Matrix for Reactor AntiNeutrinos (ISMRAN) detection experiment aims to measure anti-neutrino flux at short distance from nuclear reactors for sterile oscillation searches and possible non-intrusive monitoring of reactor power. ISMRAN detector is proposed to be ~ 1 tonne by weight segmented plastic scintillator (PS) geometry using moderate layered shielding of Boronated Polyethylene (BP) and Lead, housed inside a movable trolley structure with waveform digitizers forming its DAQ. Detector standoff from core is ~ 13 m and is over ground which leads to high backgrounds. Such a setup calls for a precise understanding of detector response and backgrounds, an improved detection efficiency and also a robust analysis framework. This thesis addresses the above aspects of the experiment.

A prototype, mini-ISMRAN, which is a 16% by volume (4×4 array) of the full scale detector is set up to carry out characterization and benchmarking studies. The response of each PS bar is first studied and found to be linear in the energy region of interest with a resolution function $\sim 20\% / \sqrt{E}$. PS bar responses are gain-matched for collective operation. Synchronization and daisy-chaining of digitizers is done to set up a multi-digitizer DAQ. The synchronized DAQ is measured to provide a time resolution down to ~ 220 ps between two PS bars for cosmic muon signals. A correlation of timestamp difference of PMTs to the Z position of event in a single PS bar is established allowing for a 3D position reconstruction for possible use in topological cuts. Correlated gamma-ray source (^{60}Co) data taken with mini-ISMRAN benchmarks the use of sum energy and bar multiplicity (N_{bars}) as base variables for signal and background discrimination.

A GEANT4 simulation of the antineutrino induced inverse beta decay (IBD) reaction inside the full ISMRAN geometry yields a maximum of $\sim 21\%$ detection efficiency using sum energy and N_{bars} variables and photon evaporation model for Gd cascade. A mean time delay of $68 \mu\text{s}$ is observed between the IBD positron and neutron signal. An embedded event analysis, which involved injecting simulated events into mini-ISMRAN reactor data, provides a realistic efficiency estimate of $\sim 4\%$ for the smaller mini-ISMRAN setup. Parallely, applying machine learning algorithm - Multi Layer Perceptron (MLP) on simulated data from ISMRAN with inclusion of another powerful variable is seen to discriminate prompt IBD positron signal from backgrounds with $\sim 91\%$ efficiency and minimal impact on final antineutrino spectral shape.

Measurements with unshielded mini-ISMRAN in lab provided a natural background rate of ~ 132 Hz in 3-8 MeV energies in a PS bar. In reactor, and inside 10 cm Pb and BP shield this background rate drops to about 20-30 Hz. An uninterrupted mini-ISMRAN reactor data of four months (one month of full reactor OFF and three months of reactor ON with few days of OFF) was chosen for filtering possible IBD candidates. Analysis of this data is done using an elaborate scheme of cuts based on simulations. Advanced cuts on timing, Z positions and energy ratios for bars triggered in an event are introduced. This is followed by a 'mixed event' analysis to extract the background level. The subtraction of these background events from the signal and background region yielded candidate antineutrino-like event numbers reasonably close to the theoretical prediction for the mini-ISMRAN setup at ~ 13 m from reactor core, but with large statistical and systematic uncertainties.